NASA/CR—2015–218840

Fuselage-Induced Velocity Model for LRTA, RTA, and HART Fuselages

Berend G. van der Wall
German Aerospace Center
Braunschweig, Germany

Sung N. Jung
Konkuk University
Seoul, South Korea

Ganesh Rajagopalan
Sukra-Helitek
Ames, Iowa

Eduardo Solis
Ames Research Center
Moffett Field, California

Angello Castro
Universities Space Research Association
Ames Research Center
Moffett Field, California

June 2015

NASA STI Program ... in Profile

Since its founding, NASA has been dedicated to the advancement of aeronautics and space science. The NASA scientific and technical information (STI) program plays a key part in helping NASA maintain this important role.

The NASA STI program operates under the auspices of the Agency Chief Information Officer. It collects, organizes, provides for archiving, and disseminates NASA's STI. The NASA STI program provides access to the NTRS Registered and its public interface, the NASA Technical Reports Server, thus providing one of the largest collections of aeronautical and space science STI in the world. Results are published in both non-NASA channels and by NASA in the NASA STI Report Series, which includes the following report types:

- TECHNICAL PUBLICATION. Reports of completed research or a major significant phase of research that present the results of NASA Programs and include extensive data or theoretical analysis. Includes compilations of significant scientific and technical data and information deemed to be of continuing reference value. NASA counterpart of peer-reviewed formal professional papers but has less stringent limitations on manuscript length and extent of graphic presentations.

- TECHNICAL MEMORANDUM. Scientific and technical findings that are preliminary or of specialized interest, e.g., quick release reports, working papers, and bibliographies that contain minimal annotation. Does not contain extensive analysis.

- CONTRACTOR REPORT. Scientific and technical findings by NASA-sponsored contractors and grantees.

- CONFERENCE PUBLICATION. Collected papers from scientific and technical conferences, symposia, seminars, or other meetings sponsored or co-sponsored by NASA.

- SPECIAL PUBLICATION. Scientific, technical, or historical information from NASA programs, projects, and missions, often concerned with subjects having substantial public interest.

- TECHNICAL TRANSLATION. English-language translations of foreign scientific and technical material pertinent to NASA's mission.

Specialized services also include organizing and publishing research results, distributing specialized research announcements and feeds, providing information desk and personal search support, and enabling data exchange services.

For more information about the NASA STI program, see the following:

- Access the NASA STI program home page at http://www.sti.nasa.gov

- E-mail your question to help@sti.nasa.gov

- Phone the NASA STI Information Desk at 757-864-9658

- Write to:
  NASA STI Information Desk
  Mail Stop 148
  NASA Langley Research Center
  Hampton, VA 23681-2199

NASA/CR—2015–218840

Fuselage-Induced Velocity Model for LRTA, RTA, and HART Fuselages

Berend G. van der Wall
German Aerospace Center
Braunschweig, Germany

Sung N. Jung
Konkuk University
Seoul, South Korea

Ganesh Rajagopalan
Sukra-Helitek
Ames, Iowa

Eduardo Solis
Ames Research Center
Moffett Field, California

Angello Castro
Universities Space Research Association
Ames Research Center
Moffett Field, California

National Aeronautics and
Space Administration

Ames Research Center
Moffett Field, CA 94035-1000

June 2015

Acknowledgments

This report was written and compiled by Berend G. van der Wall with technical contributions from Sung N. Jung, Konkuk University; Marc Wentrup, German Aerospace Center; Ganesh Rajagopalan, Sukra-Helitek; and Eduardo Solis and Angello Castro, NASA Ames Research Center.

Available from:

NASA Center for AeroSpace Information
7115 Standard Drive
Hanover, MD 21076-1320
443-757-5802

National Technical Information Service
5301 Shawnee Road
Alexandria, VA 22312
703-605-6000

This report is also available in electronic form at

http:/ntrs.nasa.gov

Table of Contents

List of Figures ... iv
List of Tables ... vi
Nomenclature ... vii
Summary ... 1
1. Introduction ... 3
2. Data Generation Using CFD ... 8
   2.1 LRTA Computed by DLR Using the TAU Code ... 9
   2.2 RTA Computed by NASA Using the RotCFD Code ... 11
   2.3 HART Computed by KU Using the KFLOW Code ... 13
3. Physics Observed in Fuselage-Induced Velocities ... 15
   3.1 Potential Flow Around a Sphere ... 15
   3.2 Investigation of CFD Data With Respect to Potential Flow Characteristics ... 16
   3.3 A Generic Example ... 23
4. Semi-Empirical Model of Fuselage-Induced Velocities ... 24
   4.1 LRTA and RTA Fuselages ... 24
   4.2 HART Fuselage ... 28
      4.2.1 Angle-of-Attack Variation ... 31
      4.2.2 Side-Slip Angle Variation ... 33
      4.2.3 Blending of Angle of Attack and Side-Slip Angle for Arbitrary Combinations ... 35
5. Comparison of the Model With CFD Data ... 36
   5.1 Range of Small Angles of Attack, No Side-Slip ... 36
   5.2 Range of Large Angles of Attack (HART Only), No Side-Slip ... 40
   5.3 Range of Large Side-Slip Angles (HART Only), No Angle of Attack ... 43
6. Model Behavior Outside the Validated Data Range ... 45
7. Effect of Fuselage-Rotor Interference on Rotor Trim ... 49
   7.1 Results From Simple Blade Element Theory ... 49
      7.1.1 Effect on Thrust ... 50
      7.1.2 Effect on Lateral Control ... 52
      7.1.3 Effect on Longitudinal Control ... 53
   7.2 Results From Nonlinear Rotor Simulation ... 54
      7.2.1 Bo105 Model Rotor With Bo105 Fuselage in Descent ... 54
      7.2.2 LRTA, RTA, and HART: Fuselage Effect When Re-Trimming the Rotor ... 56
      7.2.3 LRTA, RTA, and HART: Fuselage Effect When Keeping Collective Fixed ... 59
8. Conclusions ... 64
9. References ... 66

List of Figures

Figure 1: Overview of typical rotorcraft aerodynamic interactions (from reference [1]).............. 3
Figure 2: Free-stream flow deflection due to fuselage presence. 5
Figure 3: Mutual interference between fuselage and rotor. 6
Figure 4: Fuselage bodies investigated. 7
Figure 5: CFD computational grid for the LRTA. 9
Figure 6: Convergence history of the start solution, LRTA, $\alpha = 0°$. 10
Figure 7: Convergence history of the restart solutions for various α, LRTA. 10
Figure 8: CFD computational grid for the RTA. 12
Figure 9: Convergence history of velocity residuals, RTA, $\alpha = 0°$. 12
Figure 10: CFD computational grid for the HART II. 13
Figure 11: Convergence history, HART, $\alpha = 0°$. 14
Figure 12: Potential flow around a sphere. 15
Figure 13: Potential flow around a generic fuselage body. 16
Figure 14: Fuselage-induced velocity distribution, $\alpha = -20°,\ z = 0.1R$. 16
Figure 15: Fuselage-induced velocity distribution, $\alpha = -10°,\ z = 0.1R$. 17
Figure 16: Fuselage-induced velocity distribution, $\alpha = 0°,\ z = 0.1R$. 18
Figure 17: Fuselage-induced velocity distribution, $\alpha = 10°, z = 0.1R$. 18
Figure 18: Influence of zR on fuselage-induced velocity distribution, RTA, $\alpha = 0°$. 19
Figure 19: Peak velocities of the fuselages, $\alpha = 0°$. 19
Figure 20: Proof of dependence of the peak velocities on $z, \alpha = 0°$. 20
Figure 21: Dependence of fuselage-induced velocity profiles on angle of attack. 21
Figure 22: Large areas of separated flow for large angle of attack or side-slip........................... 21
Figure 23: Lateral velocity profiles and their dependence on $z;\ \alpha = 0°$. 22
Figure 24: Superposition principle of the model. 23
Figure 25: Upwash and downwash magnitude dependence on zR, step 1, RTA. 24
Figure 26: Upwash and downwash position dependence on zR, step 1, RTA. 25
Figure 27: Upwash and downwash x shape factor dependence on zR, step 1, RTA. 25
Figure 28: Upwash and downwash y shape factor dependence on zR, step 1, RTA. 25
Figure 29: Upwash and downwash magnitude and position dependence on α, step 2, RTA....... 26
Figure 30: Upwash and downwash x, y, and z shape factor dependence on α, step 2, RTA. 27
Figure 31: Relative error of the model for the LRTA and RTA fuselages, step 1........................ 28
Figure 32: Relative error of the model for the LRTA and RTA fuselages, step 3........................ 28
Figure 33: Dependence of fuselage-induced velocity profiles on angle of attack, $\beta = 0°$. 29
Figure 34: Dependence of fuselage-induced velocity profiles on side-slip angle, HART. 29
Figure 35: Dependence of tail boom-induced velocity profiles on side-slip angle, HART. 30
Figure 36: Dependence of fuselage-induced velocity magnitudes on $\alpha, \beta = 0°$. 31
Figure 37: Dependence of peak velocity position and shape factor (z) on $\alpha, \beta = 0°$. 31
Figure 38: Dependence of shape factors (y, x) on $\alpha, \beta = 0°$. 31
Figure 39: Mean relative error for the angle of attack variation, $\beta = 0°$. 32
Figure 40: Dependence of velocity magnitudes and shape in z-direction on $\beta, \alpha = 0°$.............. 33

Figure 41: Dependence of position of velocity magnitudes on $\beta, \alpha = 0°$. 33
Figure 42: Dependence of shape factors (y, x) on $\beta, \alpha = 0°$. 34
Figure 43: Mean relative error for the side-slip-angle variation, $\alpha = 0°$. 34
Figure 44: Comparison of CFD data with model reconstruction, $\alpha = -20°, z = 0.1R$. 36
Figure 45: Comparison of CFD data with model reconstruction, $\alpha = -10°, z = 0.1R$. 37
Figure 46: Comparison of CFD data with model reconstruction, $\alpha = 0°, z = 0.1R$. 38
Figure 47: Comparison of CFD data with model reconstruction, $\alpha = +10°, z = 0.1R$. 39
Figure 48: Comparison of CFD data with model reconstruction, $\alpha \leq -30°, z = 0.1R$. 41
Figure 49: Comparison of CFD data with model reconstruction, $\alpha \geq 30°, z = 0.1R$. 42
Figure 50: Comparison of CFD data with model reconstruction, $\beta = 10°$. 43
Figure 51: Comparison of CFD data with model reconstruction, $\beta \geq 10°$. 44
Figure 52: Usage of the model outside the validated range, $\alpha = \beta = 0°$. 45
Figure 53: Usage of the model outside the validated range, $\alpha \neq 0°, \beta = 0°$. 46
Figure 54: Usage of the HART model outside the validated range, $\alpha \neq 0°, \beta = 0°$. 47
Figure 55: Usage of the HART model in quartering flight. 48
Figure 56: Relative thrust change due to fuselage presence. 51
Figure 57: Change in lateral cyclic control due to fuselage presence. 52
Figure 58: Change in longitudinal cyclic control due to fuselage presence. 53
Figure 59: Comparison of blade motion for different fuselage modeling, from reference [51]. 55
Figure 60: Normal force coefficient at 87 percent radius, from reference [51]. 55
Figure 61: Acoustic pressure time histories, from reference [51]. 56
Figure 62: Effect of fuselage on collective, thrust re-trimmed to isolated rotor. 57
Figure 63: Effect of fuselage on lateral cyclic, thrust re-trimmed to isolated rotor. 58
Figure 64: Effect of fuselage on longitudinal cyclic, thrust re-trimmed to isolated rotor. 59
Figure 65: Effect of fuselage on rotor power, thrust re-trimmed to isolated rotor. 60
Figure 66: Effect of fuselage on rotor thrust, collective fixed from isolated rotor trim. 60
Figure 67: Effect of fuselage on lateral control, collective fixed from isolated rotor trim. 61
Figure 68: Effect of fuselage on longitudinal control, collective fixed from isolated rotor trim. 62
Figure 69: Effect of fuselage on power, collective fixed from isolated rotor trim. 62

List of Tables

Table 1: Overall dimensions of fuselage and rotors. 7
Table 2: Free-stream velocities used for CFD computations... 8
Table 3: Parameters used for generation of figure 24.. 23

Nomenclature

$A_{u,d,t}$	Nondimensional magnitude of upwash, downwash, tail boom wash
A, B	Nondimensional radial beginning and ending of the aerodynamic part of the blade
C_l, C_d	Lift and drag coefficient
C_T, C_W	Rotor thrust and helicopter weight coefficient
c_{nj}	Polynomial coefficients of inflow ratio amplitude representation
l	Fuselage length, m
M_∞	Free-stream Mach number
R	Rotor radius, m
r	Nondimensional radial coordinate
$S_{x,y,A}$	Nondimensional shape factors
V_∞	Free-stream velocity, m/s
V_T, V_P	Blade element tangential and perpendicular velocities, m/s
v_{ixf}, v_{iyf}	Fuselage-induced velocity components in the rotor rotational plane, m/s
v_{izf}	Fuselage-induced velocity normal to the rotor rotational plane, m/s
x, y, z	Hub coordinate system (x position aft, y position starboard, z position up), m
$\bar{x}, \bar{y}, \bar{z}$	Nondimensional coordinates
x_0, y_0	Peak position of fuselage-induced velocity function, m
z_0	Fuselage centerline position below hub center, m
α	Fuselage centerline angle of attack, deg
α_a	Blade element angle of attack, deg
β	Fuselage centerline side-slip angle, deg
λ_{izf}	Fuselage-induced inflow ratio normal to the rotor disk
μ	Advance ratio
ρ	Air density, kg/m³
Ω	Rotor rotational speed, rad/s
ψ	Rotor azimuth, deg

BVI	Blade-vortex interaction
CAMRAD II	Comprehensive Analytical Model of Rotorcraft Aerodynamics and Dynamics (Johnson Aeronautics software)
CFD	Computational Fluid Dynamics
CFL	Courant–Friedrichs–Lewy
DLR	Deutsches Zentrum für Luft- und Raumfahrt (German Aerospace Center)
DNW	Deutsch-Niederländische Windkanäle (German-Dutch Wind Tunnels)
HART	HHC Aeroacoustic Rotor Test
HHC	Higher Harmonic Control
LRTA	Large Rotorcraft Test Apparatus
NASA	National Aeronautics and Space Administration
NFAC	National Full-Scale Aerodynamics Complex
RANS	Reynolds-Averaged Navier–Stokes Equations
RotCFD	Rotorcraft structured incompressible CFD solver of Sukra-Helitek
RTA	Rotor Test Apparatus

SI	Système International d'Unités (International Standardized Units)
TAU	Triangular Adaptive Upwind, the unstructured compressible unsteady CFD solver of DLR
UTTAS	Utility Tactical Transport Aircraft System

Summary

In order to make the aerodynamic fuselage-rotor interference effects available to comprehensive rotor codes, a simple analytical model of the fuselage-induced velocities is developed here for the following bodies used in wind tunnel experiments:

- the Large Rotor Test Apparatus (LRTA),
- the Rotor Test Apparatus (RTA), and
- the Higher Harmonic Control Aeroacoustic Rotor Test (HART).

While the first two are used in the National Full-Scale Aerodynamics Complex (NFAC) at NASA Ames Research Center, California, the third one is used by Deutsches Zentrum für Luft- und Raumfahrt (DLR) in the large low-speed facility of the German-Dutch wind tunnel in the Netherlands. The fuselage-induced velocity model is based on parameter identification of isolated fuselage-induced velocity data (computed by means of computational fluid dynamics (CFD)) and is intended to be generic enough to be used for real helicopter fuselages as well. The accuracies obtained in reproducing the CFD data show a remaining average error of less than or equal to 5 percent of the peak-to-peak induced velocity range, which is considered sufficient for comprehensive code analysis.

1. Introduction

Compared to early helicopter design, modern helicopters have larger fuselage bodies relative to rotor diameter, and they are located closer to the main rotor. Therefore, fuselage-rotor mutual interactions become more evident and more important for the main rotor and the overall helicopter performance. This interaction problem can be analyzed in detail using computational fluid dynamics (CFD) but at a tremendous computational effort. Rotorcraft interactional aerodynamics is one of the key research fields for design, performance, handling qualities, vibration, and aero-acoustic radiation.[1]-[3] Sheridan[1] describes experiences during the YUH-61A Utility Tactical Transport Aircraft System (UTTAS) development program where Boeing encountered interactional phenomena and subsequently performed broad studies in their wind tunnel to understand these interactions. He states that these interactions become more severe in today's helicopters because their design is more complex, they have a trend to higher disk loading, and the general requirements for compactness result in a closer proximity of components.

The interaction occurs between the individual components such as the rotor, hub, fuselage, empennage, tail stabilizers, and tail rotor (fig. 1). The effects are essentially nonlinear and dependent on flight condition and thrust level. Because of the general trends for higher disk loadings of the rotor and advanced operational requirements (e.g., smaller clearance and higher transportability) in modern helicopter designs, the interaction phenomena have become more problematic. During last decades, a large volume of research has been conducted to identify the sources of the problem. This led to a closer understanding of the interaction mechanisms and advances in prediction capability for complete helicopter configurations. The studies can be categorized as purely experimental or experimental-cum-theoretical work,[4]-[12] simple analytical or numerical work that uses simplified aerodynamic and structural models,[13]-[23] or

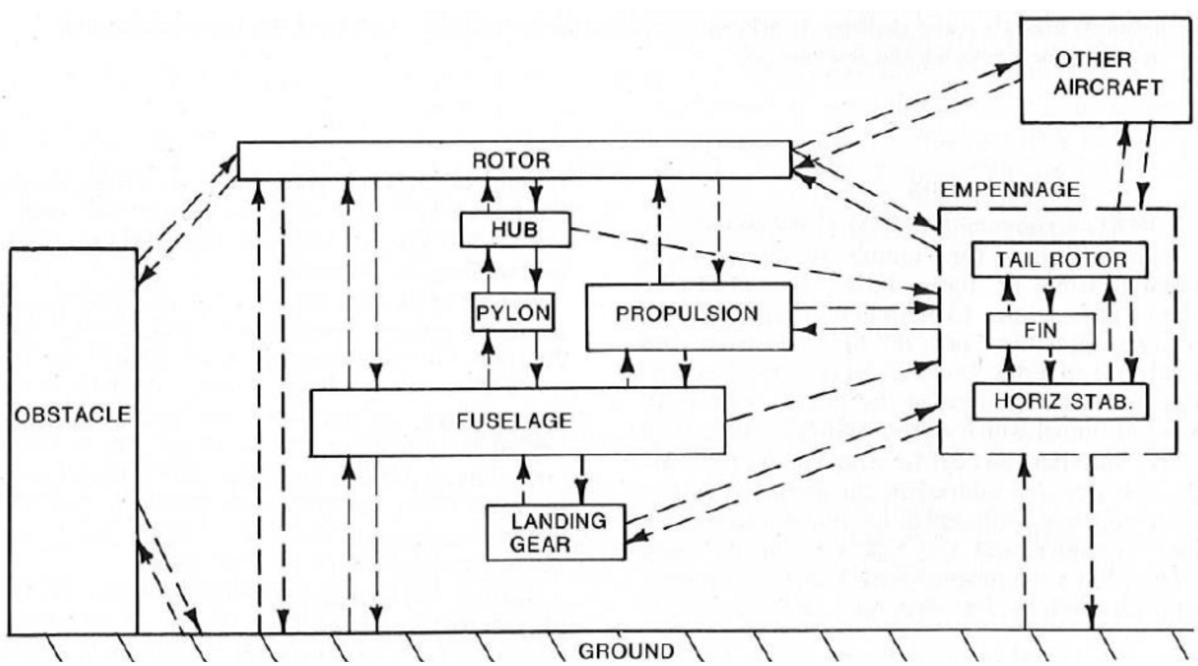

Figure 1: Overview of typical rotorcraft aerodynamic interactions (from reference [1]).

computationally more involved work that directly solves Euler or Navier–Stokes equations for the rotorcraft flow field.[24]-[33]

Leishman and his associates[4],[5],[7],[11] investigated the interference effects for a scaled rotor/body model in a wind tunnel by varying the flight speeds and shaft orientation angles while fixing the distance between rotor and fuselage. They used structurally rigid blades to simplify the investigation. Both steady and unsteady aerodynamic loads were measured using pressure transducers distributed over the fuselage surface. In addition to the combined rotor/body configuration, either the isolated rotor or the isolated fuselage case was tested to determine the interaction effects separately. The interaction effects were found to be significant in hover and low-speed forward flight. The rotor generated a download on the fuselage due to the downwash of the rotor, and in reverse the fuselage affected the rotor by substantially increasing the thrust. After re-trimming to the isolated rotor thrust, a reduction of the rotor power was observed: the fuselage acted similar to ground effect. Unsteady pressure fluctuations on the body were detected at blade passage frequencies. A lifting-line blade element theory of the rotor was coupled with a source-panel model of the body to provide the numerical predictions of the rotor/body interaction analysis. A prescribed wake model was used to calculate the local induced velocities of the rotor. Fair correlation between measured and computed surface pressures was obtained with the simple analysis.

The conventional analytical model for the interaction phenomena typically used a lifting-line aerodynamic model with rigid[11],[16],[20] or elastic[13]-[15] blade representation, a prescribed (vortex rings)[11],[14],[18] or free wake[16],[20] representation of the vortex wake, along with a source panel fuselage model. These first-generation models have evolved into more refined analytical models such as seen in Wachspress et al.[21] and Kenyon and Brown.[22] In addition, Yamauchi and Johnson[23] performed a comprehensive rotorcraft analysis combined with a modified slender-body theory to identify body-induced effects on rotor performance and loads behavior. Several axisymmetric body shapes and different rotor types were considered for the investigation. The comparison results demonstrated a solution with reliable accuracy against the closed-form solution with significantly higher computational efficiency than the potential-based panel approaches. Wachspress et al.[21] used a fast vortex/fast panel method to predict the rotor/body/wake problem under the limitation of the nonviscous flow assumption. This obvious limitation was overcome by Kenyon and Brown,[22] who introduced the vorticity transport model based on the solutions of the Navier–Stokes equations in vorticity-velocity form. A remarkable feature of this approach was a vortex wake computation that showed little numerical dissipation with less computational requirements compared to conventional CFD approaches. Despite the advantage in wake-preserving characteristics, some controversies surfaced especially with regard to a grid convergence problem.[24]

Thanks to the notable growth of computer hardware capabilities, CFD-based methods such as RANS (Reynolds-Averaged Navier–Stokes) solvers have become one of the most powerful tools to tackle the rotorcraft aerodynamic interaction problem. Nam et al.[25] used Euler simulations on unstructured meshes to estimate the interactional aerodynamic features of rotor/body coupled configurations. A sliding mesh algorithm was adopted to deal with the rotational motion of the rotor in relation to the nonrotating rectangular grids. The correlation results showed reasonable agreement with the wind tunnel measurement data including substantial deviations of the rotor-induced velocities and static pressures near tip vortex impingement locations. Neglecting the viscous effects was blamed for the discrepancy. The most up-to-date CFD approaches used an unsteady RANS solver combined with a structured[26],[29],[31],[34] or an unstructured[33] overset grid system. The viscous boundary layers were taken into account naturally with proper choice of the turbulence modeling. Recent studies on aerodynamic interaction include a complete helicopter configuration including the tail rotor.[34]

Even though the direct use of CFD is viable and sometimes desired in predicting the complicated interaction behavior accurately, it is still computationally expensive and prohibitive, especially for cases within the preliminary design stage of a rotorcraft. Whereas the conventional approach based on lifting-line theory with a prescribed or free vortex wake model lacks the critical accuracy required in the rigorous evaluation of various physical phenomena, these simplified methods are advantageous, particularly in terms of computational efficiency. It is estimated for an isolated rotor case that the computational costs would be reduced by six orders of magnitude compared to the CFD counterpart method.[35]

With a view on the aforementioned aspects of the rotor/fuselage interaction problems, an accurate and computationally more efficient solution can be reached by combining the prescribed wake modeling with the state-of-the-art CFD approach. In the context of the present research, a RANS CFD solver computes the flow fields induced by a fuselage near the rotor disk. These CFD results are used to identify the parameters of a simple mathematical model that represents these effects in the volume surrounding the rotor with sufficient accuracy. This model is then fed into the lifting-line method for both efficiency and accuracy. A schematic example of free-stream deflection angles due to a fuselage is given in Stepniewski's textbook, *Rotary-Wing Aerodynamics*[36] and shown in figure 2 (a) herein. A similar schematic with a small side-slip angle of only 3° is shown in figure 2 (b), reproduced from Rand.[15] It is obvious that even small side-slip angles will cause a relatively large amount of asymmetry and need to be accounted for.

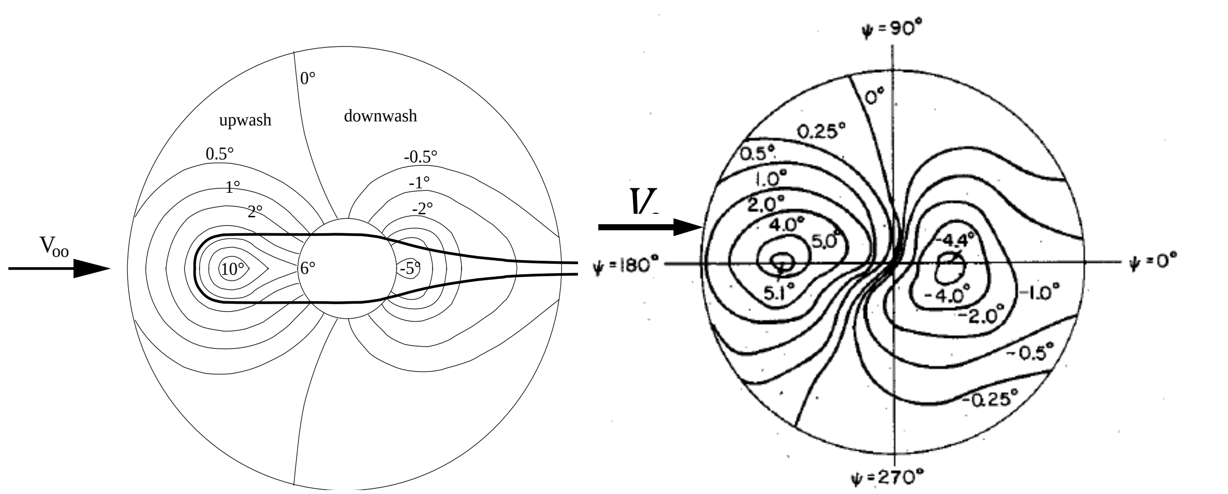

(a) No side-slip, adapted from reference [36] (b) With 3° side-slip, from reference [15]

Figure 2: Free-stream flow deflection due to fuselage presence.

The importance of such interaction for today's helicopters is highlighted by Dreier[37]:

"The problem of correctly modeling aerodynamic interference in a rotorcraft is as much art as it is science. … The downwash from a rotor impinges on the fuselage, striking it almost normally. With forward speed, the wake decreases in strength and moves toward the tail. The fuselage itself also decelerates or redirects the moving air, influencing all other bodies attached to it. As the fuselage plows through the air, the air above it is pushed out of the way. The air also is retarded directly in front of the fuselage, but accelerated in the x direction over the top of the fuselage. … A potential flow model of the fuselage is one method to estimate the effect."

Alike, Leoni's book[38] about the development of the UH-60 helicopter mentions this problem:

"The rotor performance of first prototype flight tests was way behind predictions, and vibrations were above … one cause was identified in the rotor being too close to the fuselage … leading to a shaft extender, raising the hub above for flight and lowering it for stowage and folding in a transport aircraft or vessel."

Overall, there is enough reasoning to address this subject of fuselage-rotor interaction, sketched in figure 3 (a). Keep in mind that there always is a mutual interaction of the rotor back onto the fuselage via its downwash, generating an additional aerodynamic download (and side-force as well as moments) relative to the isolated forces and moments of the fuselage that need to be accounted for (see fig. 3 (b)). Typically the rotor downwash attacks the fuselage from top to bottom, generating a download that adds to the helicopter weight and causes the total rotor lift to be larger than the vehicle weight in most operational conditions, especially in hover. However, the rotor-fuselage interaction is not addressed here.

Three fuselages are investigated in this study:

- the Large Rotor Test Apparatus (LRTA),
- the Rotor Test Apparatus (RTA), and
- the Higher Harmonic Control Aeroacoustic Rotor Test (HART).

While the first two are used in the National Full-Scale Aerodynamics Complex (NFAC) at NASA Ames Research Center, California, the third one is used by Deutsches Zentrum für Luft- und Raumfahrt (DLR) in the large low-speed facility of the German-Dutch wind tunnel in the Netherlands. All three of them are sketched in figure 4. Note that the scales are different.

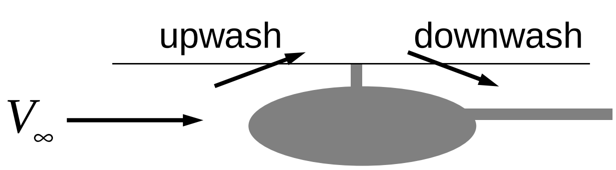

(a) Fuselage-rotor interference

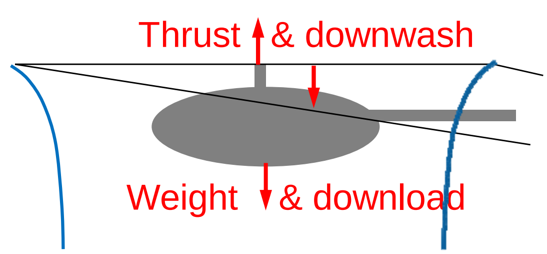

(b) Rotor-fuselage interference

Figure 3: Mutual interference between fuselage and rotor.

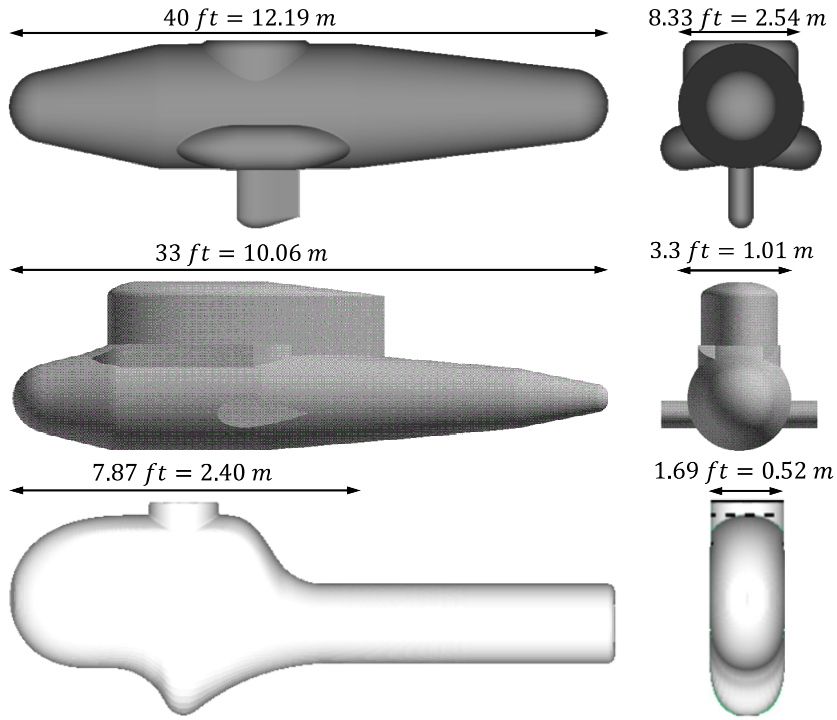

(a) LRTA for UH-60 size rotors ($R = 26.83\ ft = 8.179m$)

(b) RTA for Bo105 -size rotors ($R = 16.11\ ft = 4.91m$)

(c) HART for model-scale rotors ($R = 6.56\ ft = 2.0m$)

Figure 4: Fuselage bodies investigated.

Table 1: Overall dimensions of fuselage and rotors.

Fuselage	Fuselage length $l\ [ft; m]$	Rotor radius $R\ [ft; m]$	Fuselage centerline below hub $z_0\ [ft;\ m]$	Ratio l/R	Ratio z_0/R
LRTA	40.00; 12.19	26.83; 8.18	–7.18; –2.19	1.491	–0.2676
RTA	33.00; 10.06	16.11; 4.91	–6.44; –1.96	2.048	–0.4000
HART	7.87; 2.40	6.56; 2.00	–1.97; –0.60	1.200	–0.3000

The overall dimensions are given in table 1. It is apparent that the size of the fuselage main body relative to the rotor radius is largest for the RTA/Bo105 combination, moderate for the LRTA/UH-60 combination, and smallest for the HART. Additionally, the rotor-fuselage proximity is important as well, and here the LRTA/UH-60 is closest together, followed by HART, and the RTA/Bo105 combination appears with the largest separation. Finally, the fuselage shape also plays a role, and here the HART and RTA have large curvatures close to the rotor, while the LRTA is smooth from front to end. The conversion from imperial units to SI units made use of $1\ ft = 0.3048\ m$ for lengths and $1\ kts = 1.852\ km/h = 0.5069\ m/s$.

2. Data Generation Using CFD

Since flight speeds of conventional helicopters with a blade tip Mach number of about 0.64 are limited to approximately $V_\infty = 90\,m/s$ (or $M_\infty = 0.265$; this represents a tip speed ratio of $V_\infty/\Omega R = 0.41$ or an advancing blade tip Mach number of $M_{\psi=90°} = 0.905$), the flow around the fuselage can be considered incompressible. Even the experimental compound helicopters such as the Sikorsky X2 or the Airbus Helicopters X³ concept peak at $V_\infty = 260\,kts = 133.7\,m/s$, which represents $M_\infty = 0.393$, where compressibility effects just start to show up (the Prandtl–Glauert compressibility correction factor is 1.087). In addition, only the flow field in the volume described by rotor blade flapping is of interest, which is outside the boundary layer on the surface (i.e., in the potential flow regime). Therefore, only one velocity needs to be computed for the various fuselage angles of attack or side-slip settings. The resulting fuselage-induced velocities, referred to the free-stream velocity, v_{if}/V_∞, are justifiably assumed as independent of speed.

The air data for all the CFD computations are standard atmosphere at sea level and $15°C$ temperature. However, the oncoming flow velocity was set to different values as given in table 2 because the data were generated independently by different organizations. In addition, the outer grid dimensions, related to both the rotor radius, R, and the fuselage length, l, as given in table 1, are shown.

Note the large differences in the grids used in terms of number of grid points or cells, but also in terms of dimensions relative to the respective rotor or fuselage size. In this respect the HART fuselage computation has a much higher density of cells than all others, but the HART was computed up to extreme angle of attack and side-slip with massive flow separation to be resolved. This was not the case for both LRTA and RTA fuselages. The latter two are computed for a small range of α around 0° at no side-slip and are streamlined bodies, but the HART fuselage was computed up to $\pm 90°$ in both angle of attack and side-slip. The Mach number of all computations was well within the incompressible flow regime.

All computations were done solving the steady Reynolds Averaged Navier–Stokes (RANS) equations. The reason for using steady RANS instead of unsteady RANS is found in the application of the results: the goal is to create a mathematical model for the steady mean characteristics of the flow field. Unsteady RANS will result in highly unsteady flow fields when flow separation occurs, which usually is the case when bluff bodies are being computed, such as helicopter fuselages. Unsteady results need a long-term averaging procedure to obtain averaged flow field characteristics. In addition, the steady RANS is computationally much faster and thus more efficient for the purposes of this study.

Table 2: Free-stream velocities used for CFD computations.

Fuselage (code used)	LRTA (TAU)	RTA (RotCFD)	HART (KFLOW)
Free-stream velocity, V_∞; m/s	50	51.4	32.9
Free-stream Mach number, M_∞	0.147	0.151	0.097
Outer grid size, multiples of R	149.1	248.3	10
Outer grid size, multiples of l	100	121.1	8.33
Total discretization, times 10^6	2.2 (points)	0.066 (cells)	31.5 (cells)

2.1 LRTA Computed by DLR Using the TAU Code

Steady RANS computations were executed by Marc Wentrup of the DLR Institute of Aerodynamics and Flow Technology, Braunschweig, using the Triangular Adaptive Upwind (TAU) code. The surface definition was provided by Ethan Romander of NASA Ames Research Center. The CFD computations were performed using the DLR flow solver TAU.[39] This code solves the compressible RANS equations on an unstructured computational grid. The numerical method in space involved a central differencing scheme of second-order accuracy, with a Jameson-type artificial dissipation, on a cell-vertex-based finite volume formulation. For the considered computations, the time integration was done by an implicit Backward-Euler scheme using a Courant–Friedrichs–Lewy (CFL) number of 2. The flow was considered completely turbulent, and the turbulent terms of the RANS equations were modeled by the one-equation turbulence model from Spalart–Allmaras[40] in its original form. For the purpose of calculating the induced velocities above the LCTR fuselage, a relatively rough computational grid was created by using Gridgen by Pointwise®.[41] The resulting hybrid mesh consists of about 2.2 million points. The boundary layer was resolved by a prism/hexahedra layer normal to the surface with an initial spacing of $0.005\,mm$ and a $\tanh$ distribution function and a value of $y^{+} = 0.7$. The considered computational volume was encased by a cube with an edge length of $100 \cdot l$, with l as model length ($l = 40\,ft = 12.19\,m$) and far field boundary conditions (see fig. 5).

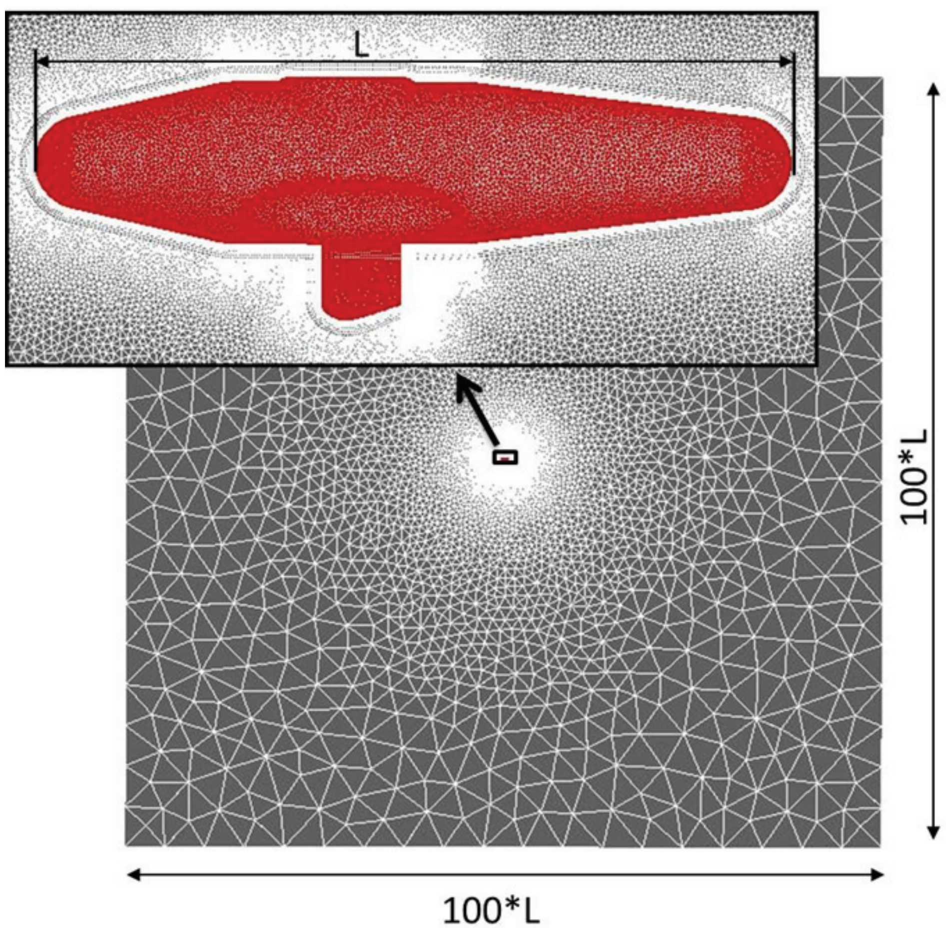

Figure 5: CFD computational grid for the LRTA.

In the first step, a restart solution with 50,000 iterations was created with a pitch angle of $\alpha = 0°$. Then 50,000 further iterations were performed for a pitch angle range of $\alpha = -20°$ to $\alpha = +15°$ with 5° step increments. Each calculation was done in parallel mode on 96 cores on the DLR C²A²S²E-2 cluster [42] using a three-level multi-grid to accelerate convergence. Each computation lasted about 3 hours. The convergence history of the initial and the restart solutions is illustrated in figure 6 and figure 7. The red line represents the density residual, the dark blue line is the lift coefficient, and the light blue line is the drag coefficient.

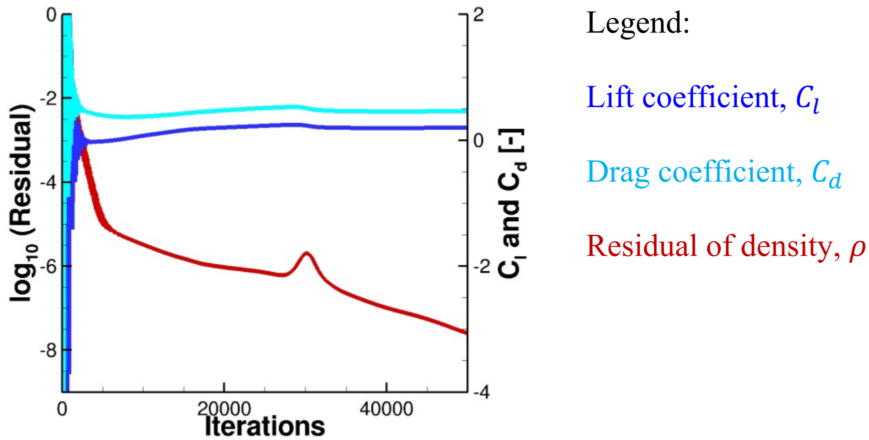

Figure 6: Convergence history of the start solution, LRTA, $\alpha = 0°$.

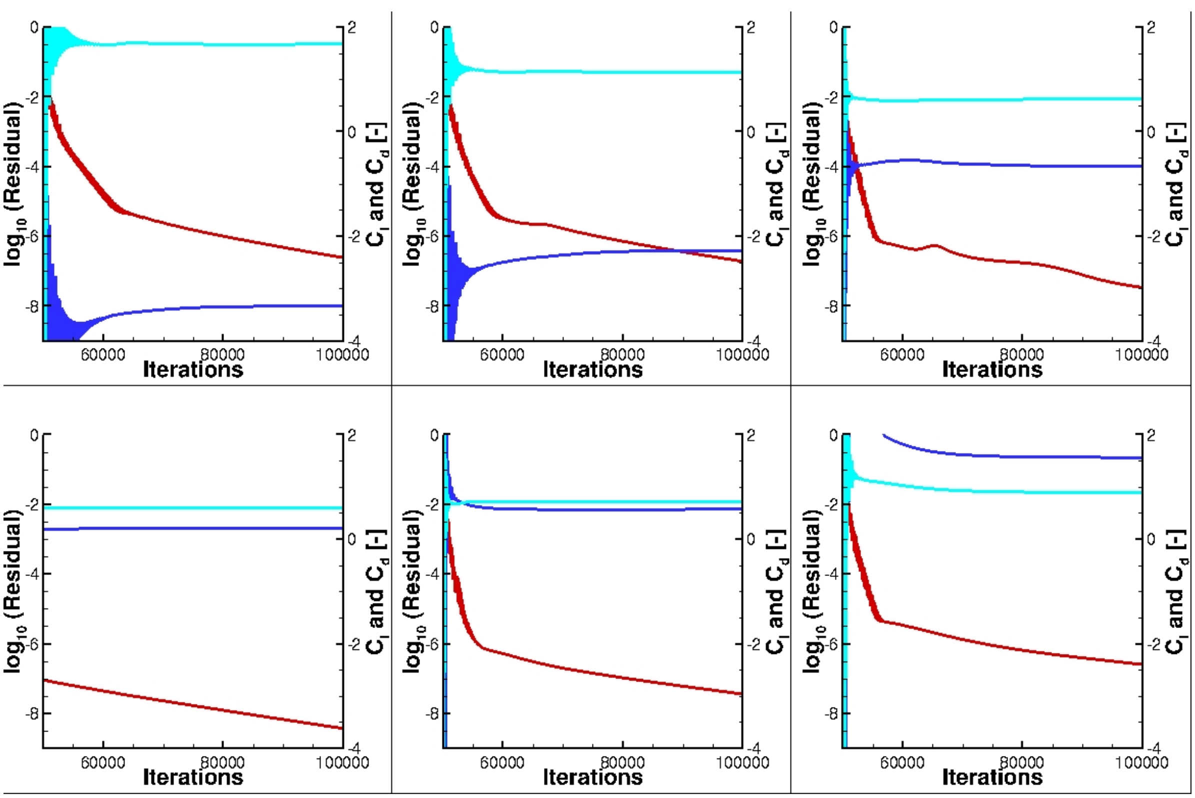

From left to right, starting on top: $\alpha = -20°, -15°, -5°, 0°, +5°$, and $+15°$.
Legend same as shown in Figure 6.

Figure 7: Convergence history of the restart solutions for various α, LRTA.

The first computation was done for $\alpha = 0°$, and its convergence behavior is shown in figure 6 for the lift and drag coefficients and the density residual. While the residual continually decreases in total by seven orders of magnitude (starts at 10^0) the body force coefficients converge to constant values. Figure 7 shows similar convergence histories for the studied angles of attack, $\alpha = -20°, -15°, -5°, 0°, +5°$, and $+15°$. For all calculations the residual drops at least by six orders of magnitude, which is considered sufficient for this purpose.

2.2 RTA Computed by NASA Using the RotCFD Code

Steady RANS computations were executed first by Ganesh Rajagopalan of Sukra Helitek, Inc. and continued by Angello Castro of NASA Ames Research Center using the RotCFD code.[43],[44] The surface definition was provided by Eduardo Solis of Monterey Technologies, Inc., at NASA Ames Research Center.

The operational cases were computed by importing a three-dimensional (3D) model of the RTA into the RotCFD environment. The 3D RTA grid was created using Rhinoceros 5.[45] The Rotor Unstructured Solver (RotUNS) application within RotCFD was used to set up the parameters specified by each case. RotUNS was preferred over the other available applications because it allowed for the creation of an incompressible Navier–Stokes solution that could capture the body geometry more accurately at the expense of increased solver run time. There were eight cases run in total, each using a different angle of attack for the RTA with respect to the oncoming wind. The angles of attack used for each of these eight cases were $\alpha = -15°, -10°, \cdots, 15°$ with a constant side-slip angle of $\beta = 0°$, because a symmetric flow was desired for analysis. The only major difference between the cases was the value of the vector components that specified the wind speed and its direction. In addition, there was a mass-outflow correction (an "open wall" in the boundary surrounding the body) in either one or two of the boundary walls simultaneously, depending on the desired direction that the wind was supposed to exit from.

In all cases the appropriate flight conditions and free-stream velocities were set up in each component by making use of simple trigonometry theorems to decompose the vectors, i.e., $V_x = V_\infty \cos\alpha,\ V_y = 0,$ and $V_z = V_\infty \sin\alpha$ for each case. The x-axis was positive downstream of the wind and parallel to the fuselage length, the y-axis was positive in the starboard direction, and the z-axis was positive upwards in the direction of the rotor hub. The lateral component was zero because there was no side-slip (no yaw). This lack of lateral flow was chosen in part because of the physical limitations of the RTA's supporting stands, which only allow for a pitching rotation of the model (nose pointing up/down), and also as a way to simplify calculations.

The mass outflow correction walls (the "open" walls) were given one of three different configurations depending on angle of attack. For the four $\alpha < 0°$ cases, the walls were placed at the x_{max} and at the z_{min} positions, meaning they were below and behind the body. For the $\alpha = 0°$ case, only a single wall was placed at the x_{max} position (behind the body). Finally, in the remaining three cases where $\alpha > 0°$, the walls were placed at the x_{max} and z_{max} positions (above and behind the body). The overall size of the computational domain was a cube with a border length of $4000\ ft = 248.3\ R$ in all directions, which allowed the solver ample space to develop a steady flow around and towards the body. The final grid is shown in figure 8.

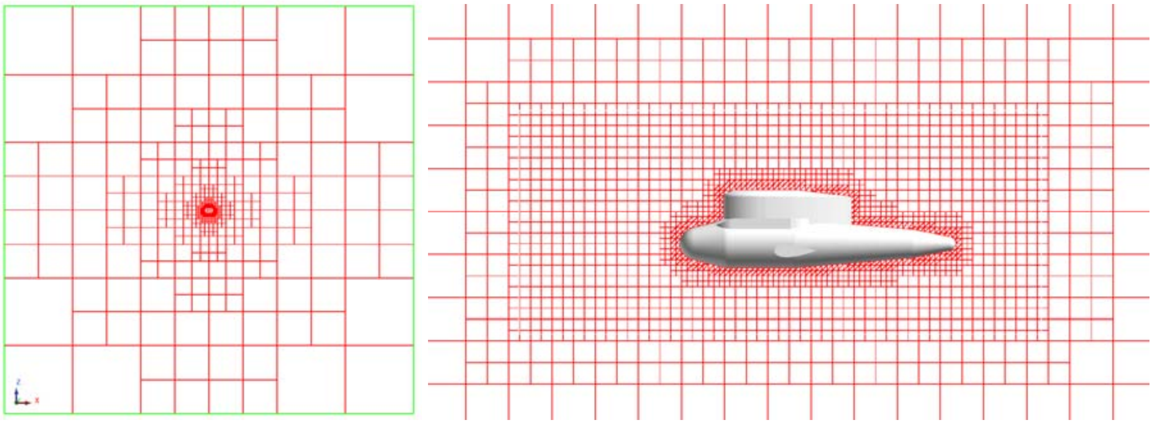

(a) overall computational domain (b) close-up view

Figure 8: CFD computational grid for the RTA.

Each case had a total of 4000 pseudo-time steps with 10 subiterations per step. All cases took approximately 4 hours to run, and they all managed to stabilize successfully. The convergence behavior of the computation until data extraction is shown in figure 9 at the example of the residual of the velocity components for the case $\alpha = 0$. The residual drops by almost three orders of magnitude within the first 500 subiterations, then remains in a constant bandwidth for the rest of the time. Compared to the computations for the LRTA shown in figure 6 and figure 7 the residual does not drop as much, thus the solutions may not be considered as "converged'' rather than "stabilized.''

The rotor radius of the Bo-105 was 16.11 ft. A refinement box, which further refines a specified part of the grid, enclosed a region of interest of $-0.1 \leq z/R \leq 0.2, -1 \leq x/R \leq 1$, and $-1 \leq y/R \leq 1$, with the origin being at the Bo-105 rotor hub center. Within this region, four extraction planes were located at locations $z/R = -0.1, 0.0, 0.1,$ and 0.2, with $z/R = 0$ being at the origin. These extraction planes were chosen to account for the blade tip displacement that occurs during flight because of blade flapping. The resolution used was of 65 points in each x/R and y/R direction, equally distant to each other ($\Delta x/R = \Delta y/R = 0.03125$) in order to make the cases easily comparable to those run with the LRTA.

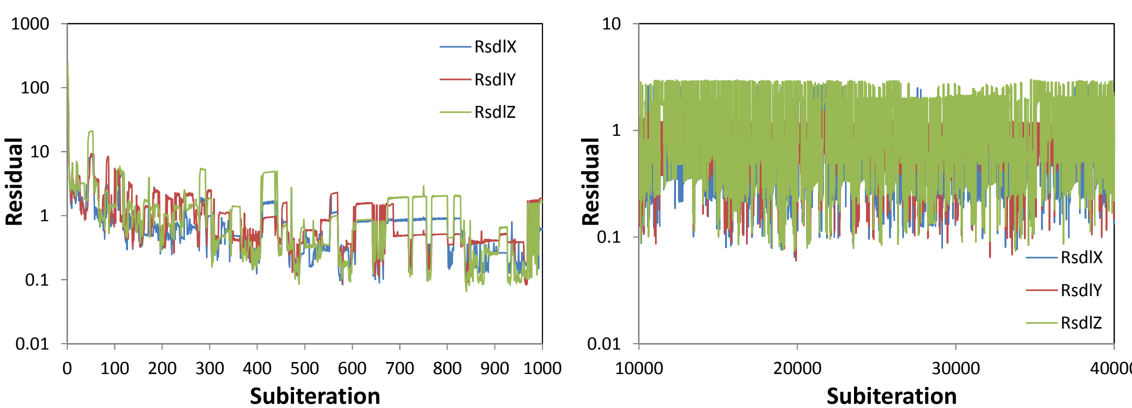

Figure 9: Convergence history of velocity residuals, RTA, $\alpha = 0°$.

Although the entire flow field was necessary to achieve the desired level of post-processing accuracy, there were only four two-dimensional (2D) areas of interest from which the data was to be extracted. These square-shaped planes had dimensions $2R \times 2R$, and were chosen to encapsulate the volume of the rotational span of the Bo-105 rotor blades. The z/R placement of these planes accounts for the blade flapping that occurs during flight, which basically displaces the blade tips up and down by a factor ranging from $-0.1R$ to $+0.2R$. The effects of steady blade coning or built-in precone (usually 2° to 3° up) are also accounted for when using these specifications.

Post-processing involved the use of a Tecplot Focus 2013 R1[46] script that converted the data into six variables: The three nondimensional coordinates x/R, y/R, and z/R, and the nondimensional fuselage-induced velocity components v_{ixf}/V_∞, v_{iyf}/V_∞, and v_{izf}/V_∞, where V_∞ represents the wind speed (or flight speed). The v_{izf}/V_∞ variable was stored as $-v_{izf}/V_\infty$ because, in rotorcraft aerodynamics, the thrust-induced velocity of the rotor is positive downwards for purely historical reasons.

2.3 HART Computed by KU Using the KFLOW Code

Steady RANS computations were executed by Sung Jung of the Aerospace Department of Konkuk University, Seoul, Korea, using the KFLOW code.[47] The surface definition was provided by the HART II International Workshop database.[48] KFLOW is a 3D, structured, unsteady RANS solver, used here to obtain the flow field around the isolated fuselage. The $k-\omega$ Wilcox–Durbin (WD+) scheme is employed for the turbulence model.[49] For the spatial discretization, the inviscid fluxes are calculated using the fifth-order weighted essentially non-oscillatory scheme. The central difference scheme is used for the viscous fluxes. A time-accurate simulation is conducted using a second-order, dual time stepping scheme for the temporal algorithm. The nondimensional time step size used in the present time marching solution is equivalent to a rotor azimuth of $\Delta\psi = 0.2°$. The number of subiterations performed at each physical time step is set to 10. An O-mesh topology for the HART II fuselage configuration along with the Cartesian background grid system was used as shown in figure 10. The near-body fuselage grid consists of about 2.5 million cells while the background off-body grid amounts to 29 million cells.

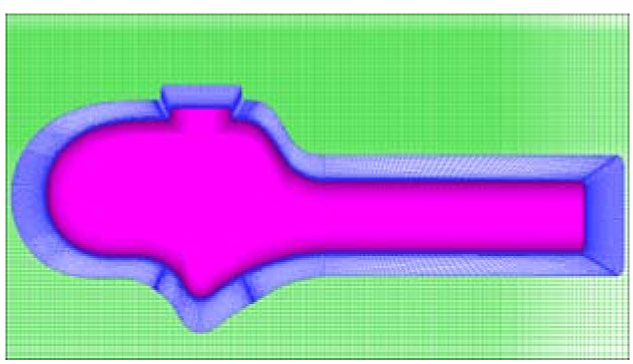

Figure 10: CFD computational grid for the HART II.

The no-slip boundary condition is applied at the solid wall of the fuselage surface. The cell spacing for the first grid point from the wall boundary is sufficiently small keeping $y^+ < 3.0$ and thereby resolving the viscous sub-layer in the turbulent boundary layer. The computation is made using a Linux-based PC cluster system with 2.93 GHz Intel I7-870 processors. All runs use a total of 80 processors. Numerical simulations are performed to obtain the flow field around the isolated HART II fuselage at different shaft angles of attack in low-speed forward flight. The convergent behavior of the steady RANS response is reached with about 6,000 iterations. An example of the convergence behavior is shown in figure 11 at the residual L_2 norm of the density.

The strong curvature of the HART fuselage downstream of the hub fairing causes flow separation even at zero angle of attack. Therefore, the convergence of a residual drops by three orders of magnitude only and remains there, while for streamlined bodies such as the LRTA several orders of magnitude more are obtained as seen in figure 6 and figure 7.

Because of the flow separation the CFD result becomes unsteady, despite the "steady" RANS setup. The data were extracted at the end of the iterations and are an instantaneous solution, not a time-averaged one. Although the turbulent flow structures are less strong than those experienced in a time-accurate unsteady simulation, they still hamper the parameter identification of the math model to be created and therefore need special treatment by ignoring the affected areas or applying a reduced weight for the errors obtained there. One possibility to overcome this situation would be to compute a longer time until a periodicity is obtained and then time-average these data. However, the steady RANS setup is not time-accurate so time-averaging may lead to erroneous results. In such a case, unsteady RANS and time-averaging over a period would be the choice but would significantly increase computational effort.

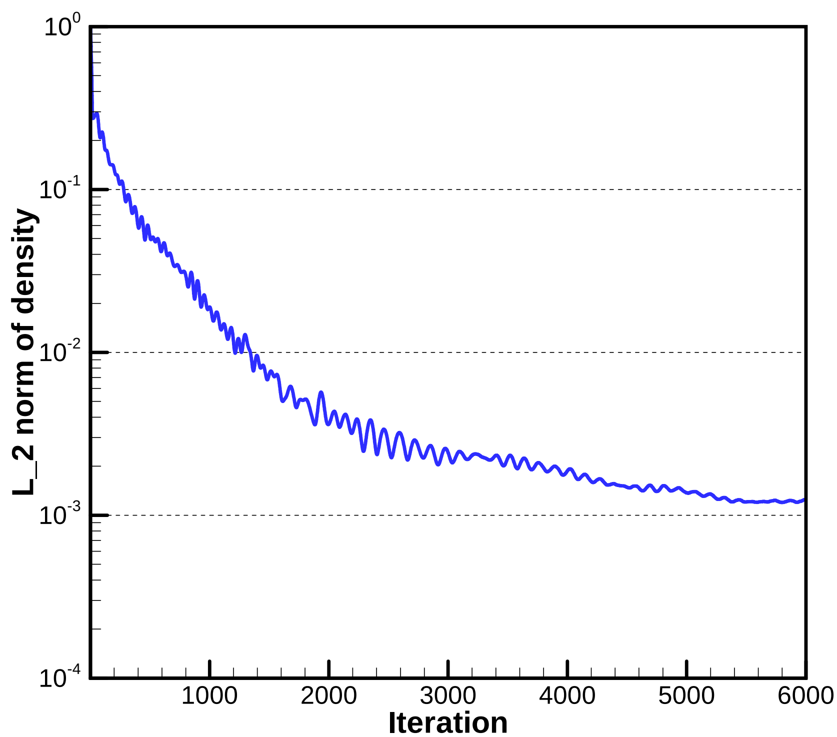

Figure 11: Convergence history, HART, $\alpha = 0°$.

3. Physics Observed in Fuselage-Induced Velocities

3.1 Potential Flow Around a Sphere

Before setting up a math model to represent the physics of the problem and not just a curve-fit to the data distribution, the physics of the problem must be understood. The flow around a body in potential theory is represented by a spatial distribution of sources and sinks, and for a closed body the integral sum of all sources and sinks must be zero. Both the spatial distribution and the strength distribution are identified in potential theory by the requirement of tangential flow as a boundary condition at the surface of the body. As an example, the potential flow around a sphere of radius, R, is shown in figure 12.

Its "fuselage"-induced velocities in incompressible inviscid potential flow are given by $\left(\bar{x} = x/R\,; r = \sqrt{\bar{x}^2 + \bar{y}^2 + \bar{z}^2}\right)$:

$$\frac{v_{ixf}}{V_\infty} = 1 + \frac{r^2 - 3\bar{x}^2}{2r^5}; \qquad \frac{v_{iyf}}{V_\infty} = -\frac{3\overline{xy}}{2r^5}; \qquad \frac{v_{izf}}{V_\infty} = -\frac{3\overline{xz}}{2r^5}$$

For large distances in any direction, the sphere-induced velocities asymptotically approach zero. As a rough estimate, the fuselage is assumed to be similar to one side of a sphere in front of the rotor hub and similar to the other side of the sphere behind the hub, with a cylindrical tube between them. An upwash in the front and a downwash in the rear are expected, with a flow parallel to the tube between. The upwash is confined to the front portion and dying out to the right and left of it. Similarly, the downwash is confined to the rear portion, also dying out to the right and left of it, as sketched in figure 13.

Therefore, in the x-direction a behavior of the upwash somehow proportional to $1/[1 + S_{xu}(\bar{x} - \bar{x}_{u0})^2]$ is expected where $\bar{x}_{u0}$ represents the position of the upwash ahead of the hub as indicated by the "+" in figure 13, and S_{xu} is a factor for the shape of the distribution. A second one, $\bar{x}_{d0}$, characterizes the position of the downwash downstream of the hub, also indicated by a "+," and it will have the same kind of proportionality, $1/[1 + S_{xd}(\bar{x} - \bar{x}_{d0})^2]$. In y-direction the velocity distribution will be somehow proportional to $1/\left(1 + S_y\bar{y}^2\right)$ because $\bar{y}_0 = 0$ due to lateral symmetry, and again S_y is a factor for the shape of the distribution. In z-direction something proportional to $1/[1 + S_z(\bar{z} - \bar{z}_0)^2]$ is expected where $\bar{z}_0$ represents the distance of the body center below the hub as also indicated in figure 13.

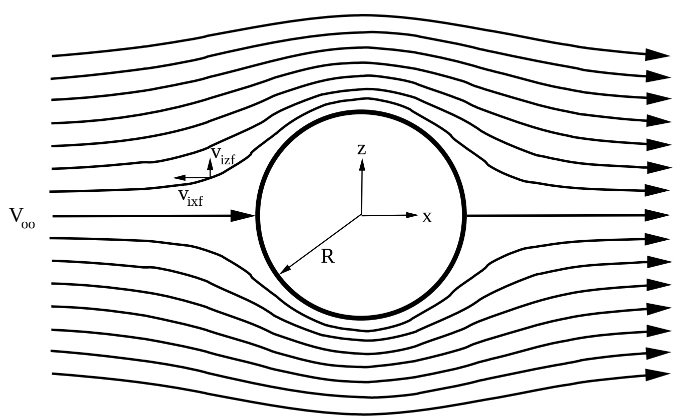

Figure 12: Potential flow around a sphere.

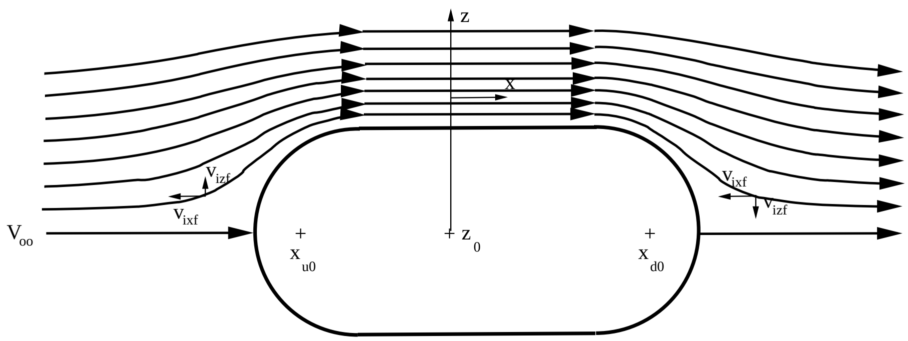

Figure 13: Potential flow around a generic fuselage body.

3.2 Investigation of CFD Data With Respect to Potential Flow Characteristics

In the following, these assumptions are cross-checked by the results of the CFD computations for a comparable range of angles of attack (no side-slip) for all three fuselages. This allows a direct comparison of the general appearance and of individual differences caused by the different shapes. In all cases a plane, $z/R = 0.1$, was chosen. Since the hub center is defined as the origin of the coordinate system, this is a plane, 10 percent radius, above the hub in the outer (potential) flow, sufficiently away from the body's surface and boundary layer.

In figure 14 the fuselage-induced velocity distribution normal to the rotor rotational plane is shown for (a) the LRTA, (b) the RTA, and (c) the HART fuselage. Because no data were available for HART at this angle of attack, they were interpolated linearly from data for $\alpha = -10°$ and $-30°$. In such a nose-down orientation the upwash in the front is quite strong. The usual sign convention is used here where downwash is positive and upwash is negative. The peak values of upwash are close to $v_{izf} \cong -0.11V_\infty$.

Both LRTA and RTA indicate a very small magnitude of downwash downstream of the hub and right and left of the fuselage, while the centerline still indicates upwash. In contrast, the HART fuselage has a rather sharp curvature behind the hub that generates, even in this nose-down condition, a downwash of up to $v_{izf} \cong 0.03V_\infty$. The sting support seems to be responsible for the upwash in the centerline at the downstream end of the data field at $x/R = 1$ because it extends the rotor radius by far, and it is a relatively thick body (see fig. 4). In any case, the asymptotic decay of the induced velocity profiles in both x- and y-directions are clearly visible. In addition,

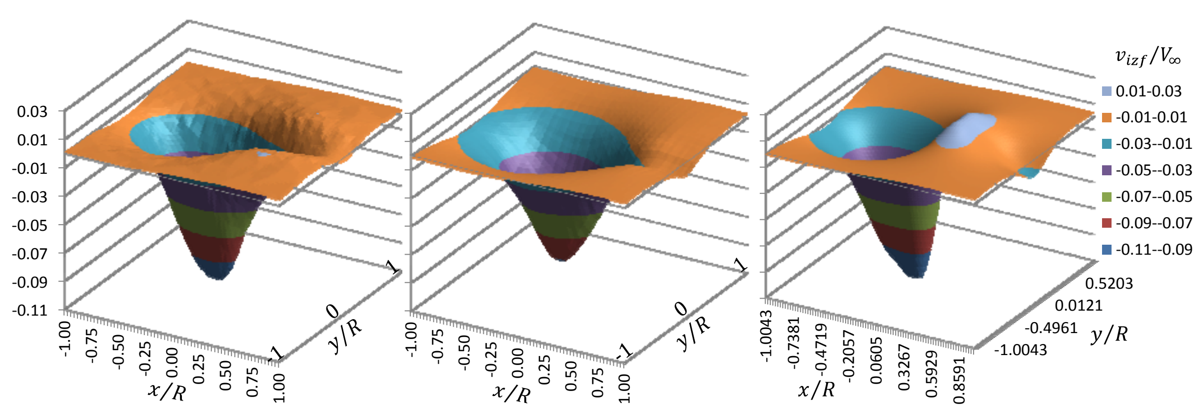

(a) LRTA (b) RTA (c) HART (interpolated)

Figure 14: Fuselage-induced velocity distribution, $\alpha = -20°,\ z = 0.1R$.

the HART fuselage generates the largest values both in upwash and in downwash; the RTA seems to have the smallest values but differences to the LRTA are marginal.

Results for $\alpha = -10°$ are shown in figure 15. The smaller nose-down inclination of the fuselage causes the upwash strength to be reduced. Also, downwash aft of the hub develops in contrast to upwash for $\alpha = -20°$ shown in the previous figure, especially for the HART fuselage. Peak values of upwash are now $v_{izf} \cong -0.1V_\infty$ and for the downwash, $0.04V_\infty$.

The $\alpha = 0°$ condition is shown in figure 16. The peak velocity of upwash in the front and downwash in the rear is almost the same, and again larger for the HART fuselage compared to the LRTA and RTA. The transition from upwash to downwash appears smoothest for the LRTA, sharper for the RTA, and even more pronounced for the HART. The latter also exhibits a secondary hump right downstream of the upwash peak, which is caused by the flow around the relatively sharp corner at the upper fairing of the fuselage model. Such local disturbances need not be modeled because they are within the blade root cutout and cannot affect blade section aerodynamics.

Finally, data are given for a nose-up attitude of $\alpha = 10°$ in figure 17. In this case the downwash strength dominates the upwash, which is especially visible for the HART fuselage. The large HART fuselage curvature aft of the hub generates a strong peak in downwash of $v_{izf} \cong 0.1V_\infty$, which is much larger than that of the LRTA or RTA where $v_{izf} \cong 0.07V_\infty$. However, this also causes flow separation to develop and to show up in the data of the HART fuselage at the downstream end of the figure around the centerline. The spikes there are caused by small-scale local turbulence and are the instant image of an otherwise unsteady phenomenon that occurs periodically or stochastically, depending on the nature of flow separation. The goal of the model to be developed is not to simulate such unsteady effects; the goal is to model the time-averaged mean velocity field. Therefore, such fluctuations need to be eliminated during the parameter identification process either by ignoring the error in these regimes or by significantly reducing it artificially.

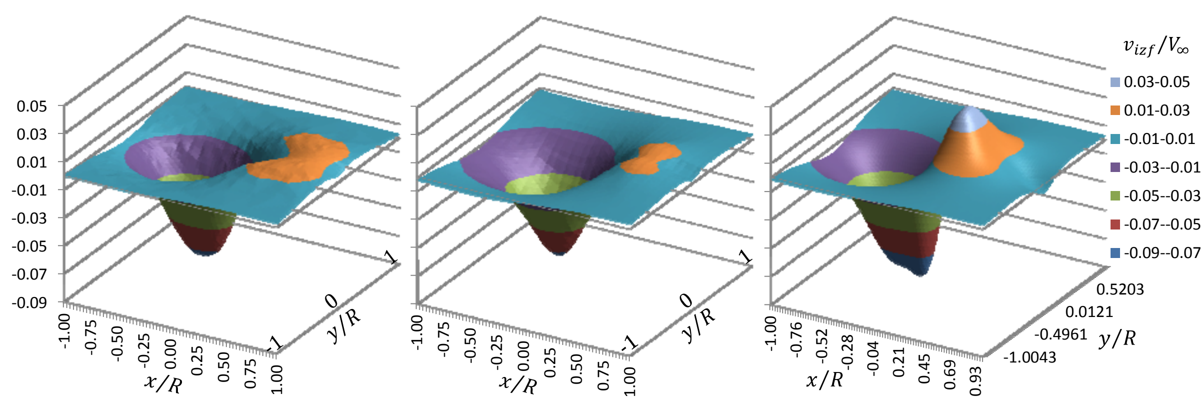

(a) LRTA (b) RTA (c) HART

Figure 15: Fuselage-induced velocity distribution, $\alpha = -10°,\ z = 0.1R$.

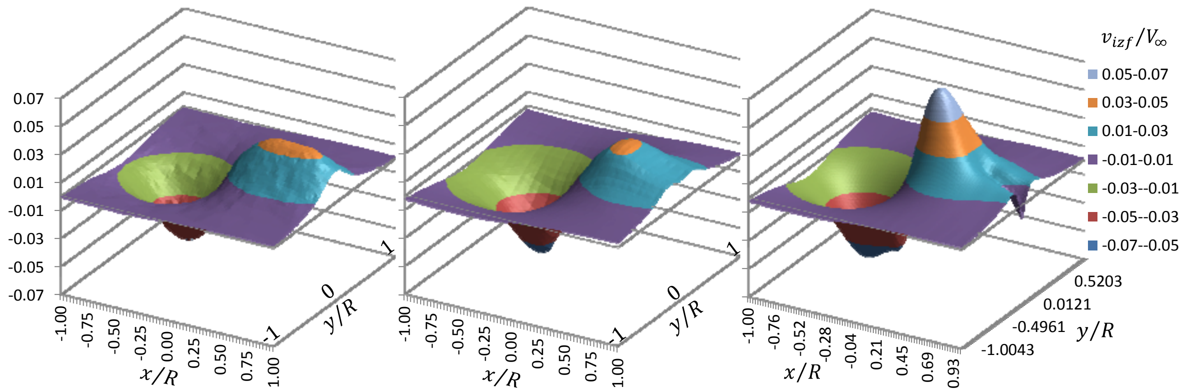

(a) LRTA (b) RTA (c) HART

Figure 16: Fuselage-induced velocity distribution, $\alpha = 0°,\ z = 0.1R$.

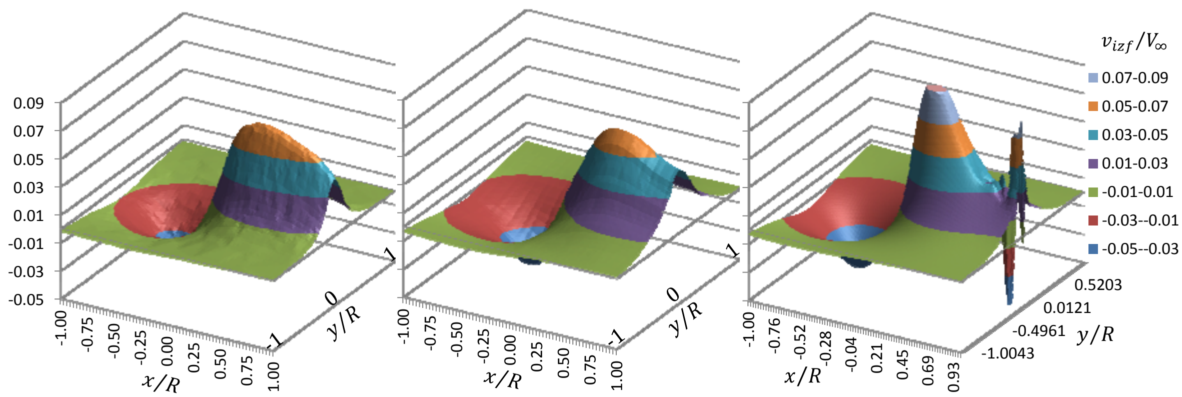

(a) LRTA (b) RTA (c) HART

Figure 17: Fuselage-induced velocity distribution, $\alpha = 10°, z = 0.1R$.

In any case the fuselage-induced velocity distributions always show asymptotic decay for increasing distance to the fuselage. The next step is to investigate the flow field behavior with increasing distance to the fuselage in the z-direction. This is done for the RTA only (fig. 18) but is representative of the general behavior of all fuselages. The scales show that the maximum upwash and downwash peaks of the fuselage-induced velocities reduce roughly by one-half of the value with every increment away from the fuselage.

This is further demonstrated when plotting the peak values of upwash and downwash, as well as the peak-to-peak or $\Delta v_{izf}/V_\infty$ versus the distance from the hub center as shown in figure 19. The decay of upwash and downwash appears to vary inversely to distance from the fuselage center and asymptotically approaches zero for large distances. In terms of their extremes in upwash and downwash of fuselage-induced velocities, the LRTA and RTA are quite similar to each other, while the HART fuselage generates larger peak velocities. This is due to larger curvatures of the HART fuselage in close proximity to the rotor than in the other two cases. Also, the upwash in the front of the LRTA and the RTA fuselages is always larger than the downwash in the rear, while the HART fuselage generates upwash and downwash of comparable magnitude. Again, this behavior is caused by the fuselage shape and especially its curvature. The general behavior, however, is the same for all three fuselages.

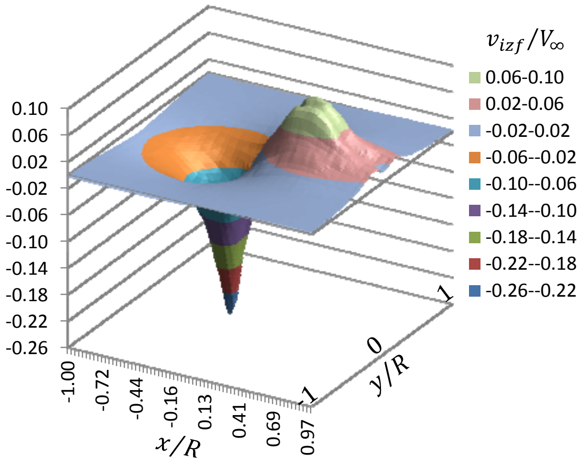

(a) $z/R = -0.1$

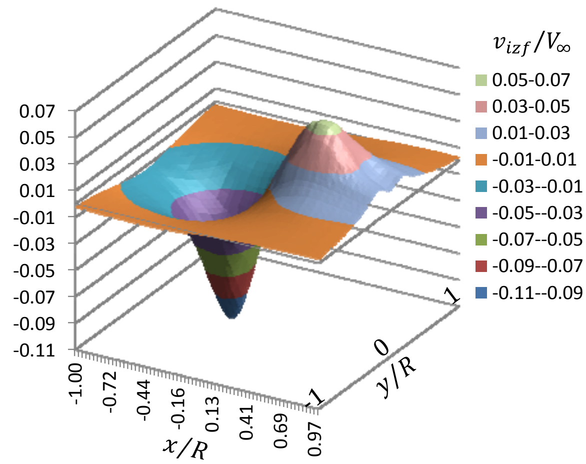

(b) $z/R = 0.0$

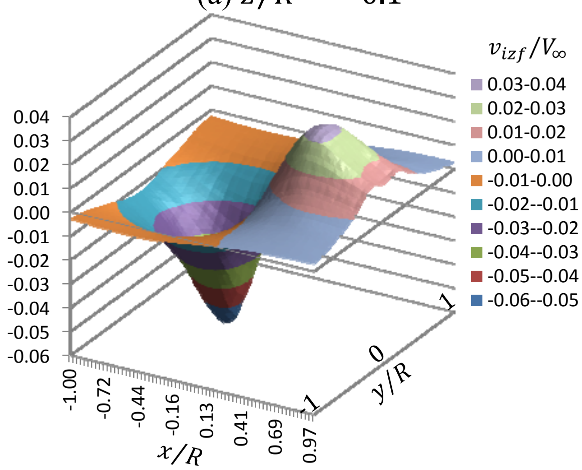

(c) $z/R = 0.1$

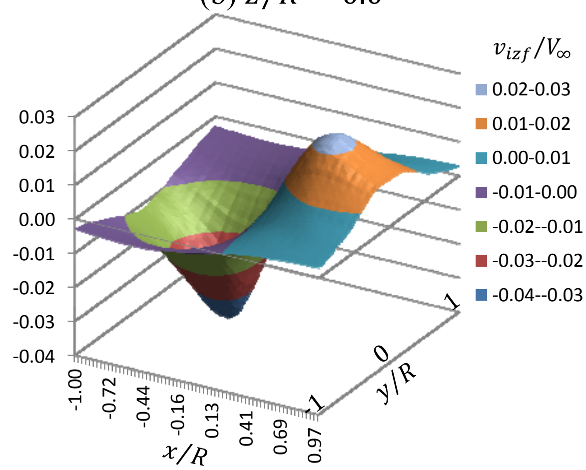

(d) $z/R = 0.2$

Figure 18: Influence of z/R on fuselage-induced velocity distribution, RTA, $\alpha = 0°$.

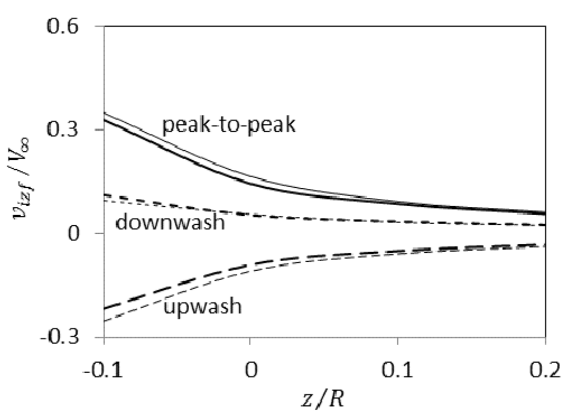

(a) LRTA (thin lines) and RTA (thick)

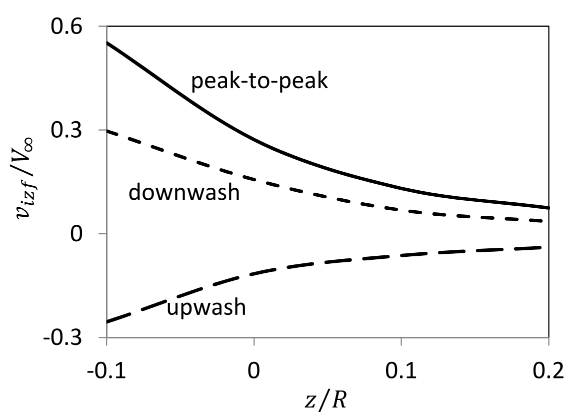

(b) HART

Figure 19: Peak velocities of the fuselages, $\alpha = 0°$.

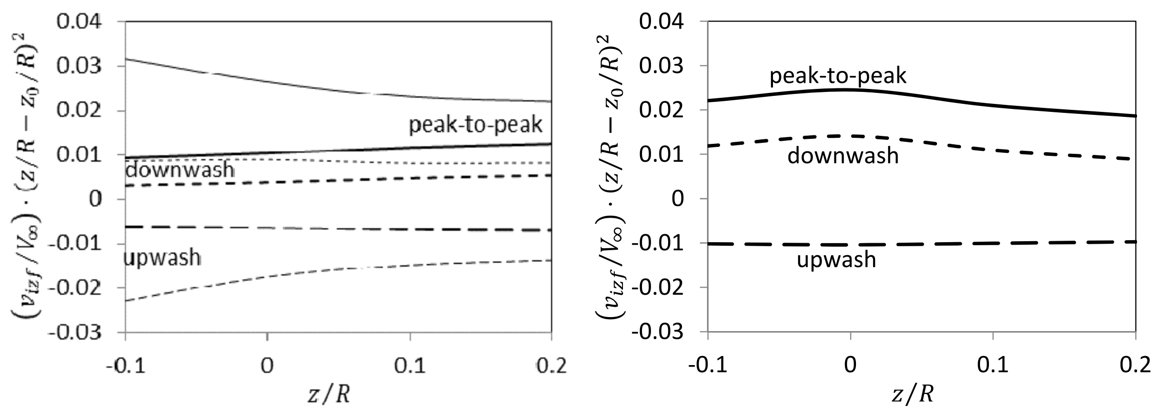

(a) LRTA (thin lines) and RTA (thick) (b) HART

Figure 20: Proof of dependence of the peak velocities on $z, \alpha = 0°$.

In order to check the dependence of these extremes with respect to the z-coordinate these data are multiplied by $(z/R - z_0/R)^2$, which should generate horizontal lines, assuming $S_z \gg 1$. The result is shown in figure 20, and it is clearly visible that the assumed dependence is actually present to a large degree.

Therefore, the general setup of dependencies with respect to x-, y-, and z-coordinates as specified previously appears physically justified and could be used within a model representing the data within the volume of rotor blade motion. Such a model could be accurate within a few percent of the free-stream velocity.

The dependence of fuselage-induced velocity profiles in the symmetry plane is investigated next. Figure 21 shows the change of upwash and downwash velocity with α for all three fuselages at $z/R = 0$.

The most undisturbed velocity profiles are seen in the data of the RTA while the LRTA shows some humps immediately before and aft of the hub fairing, indicated by the ellipses and caused by little kinks in the surface model as seen in figure 4. The upper fairing of the RTA is a streamlined body without such kinks, thus the profiles are clean. For the nose-up angles of attack of $\alpha = 10°$ and $15°$, some moderate flow separation effects downstream of the hub are visible for both the LRTA and RTA. Neither the humps in the velocity profiles nor the separated flow features need to be modeled by the analytical representation of the flow fields. During parameter identification of the model, these disturbances need special treatment—either by reduced error weight in these zones or by totally ignoring the error therein.

The HART fuselage has an even more pronounced sharp-edged fairing close to the hub (see fig. 4), and therefore a stronger influence on the flow field than the LRTA. The ellipses indicate these zones, and the humps in the velocity profiles are much larger than for the LRTA. Note that the data for $\alpha = 15°$ and $-20°$ are interpolated from those at $10°$ and $30°$ or from $-10°$ and $-30°$, respectively. The curvature of the HART fuselage downstream of the hub center causes flow separation that is visible as oscillation in some curves for $x/R > 0.25$. The mean velocity in this area is desired, therefore these spikes need to be ignored during the parameter identification. Often they are so close to each other that the entire area needs to be ignored, especially for the extreme angles of attack from $10° \leq \alpha \leq 90°$ (fig. 22 (a)), but also for side-slip angles in the range of $30° \leq |\beta| \leq 90°$, where such separated flow effects occur on the leeward side (fig. 22 (b)).

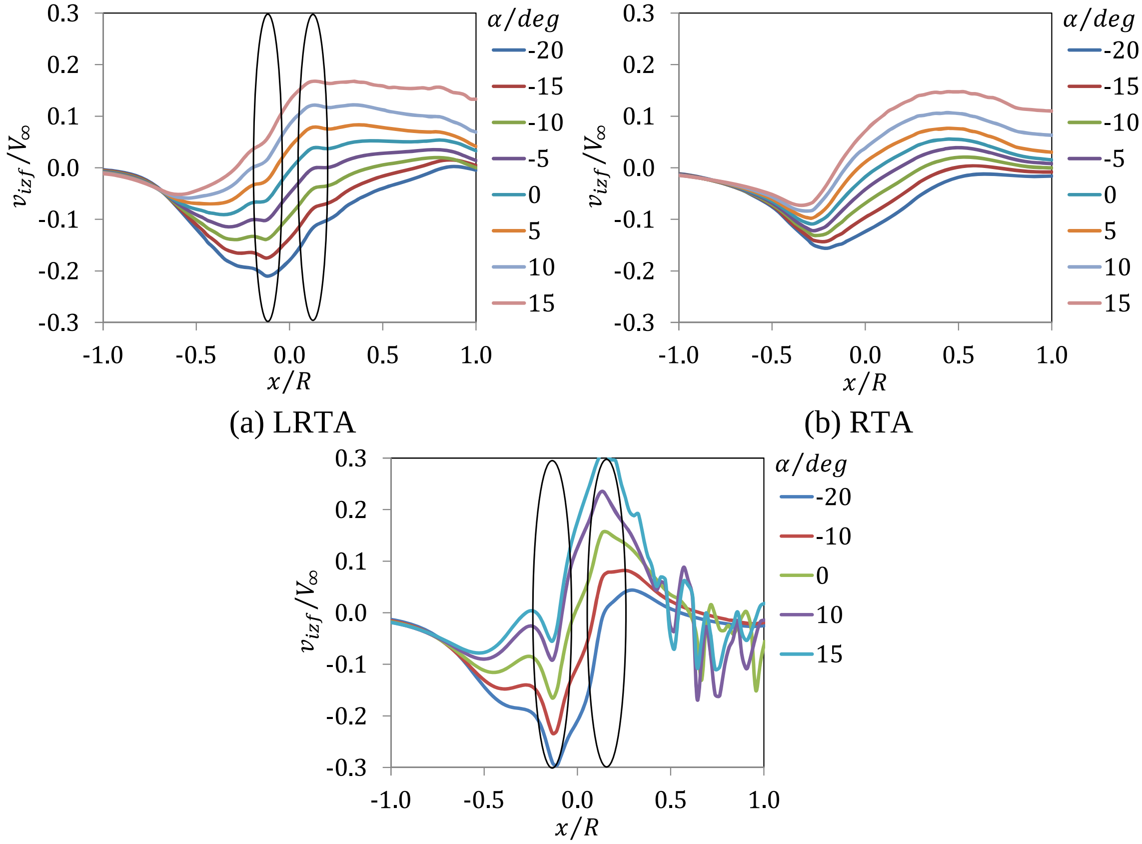

(a) LRTA (b) RTA

(c) HART All figures: $z/R = 0$.

Figure 21: Dependence of fuselage-induced velocity profiles on angle of attack.

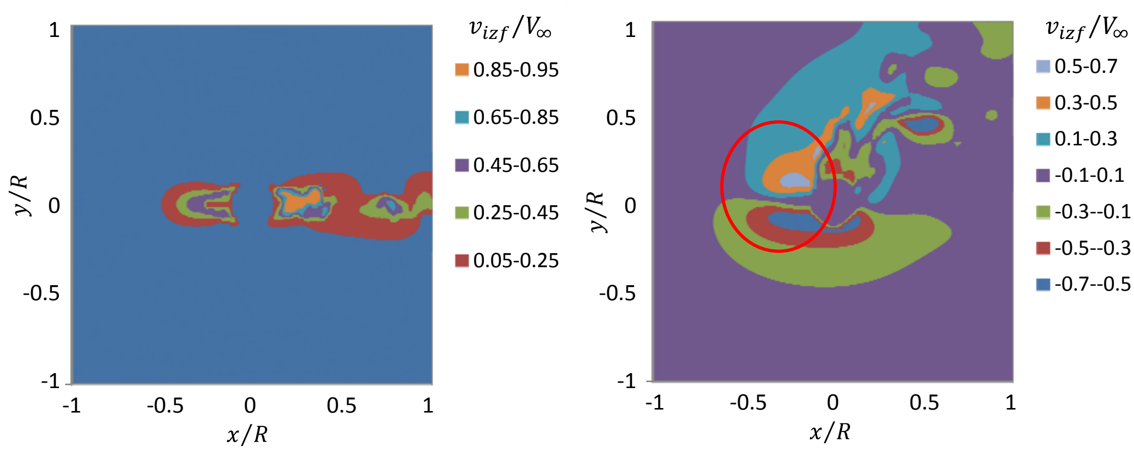

(a) $\alpha = 60°, \beta = 0°, z/R = 0$ (b) $\alpha = 0°, \beta = 60°, z/R = 0$

Figure 22: Large areas of separated flow for large angle of attack or side-slip.

The lateral symmetry of the fuselage-induced velocity profiles is given in figure 23. The curves are taken from a plane passing through the peak upwash for the LRTA at $\alpha = 0°$. In figure 23 (a) the velocity profiles for the various z/R distances to the hub center are given and in (b) these are normalized by the peak velocity in the center. It is obvious that both sides of the velocity profiles are proportional to $(y/R)^{-2}$, and the width of the profile depends on z/R. These observations can be made for the RTA and HART fuselages in a similar way.

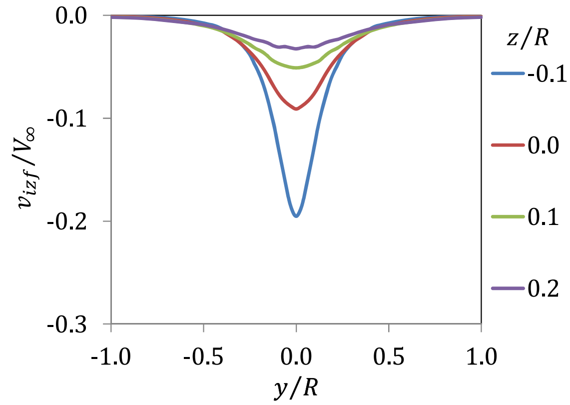

(a) Velocity profile, LRTA

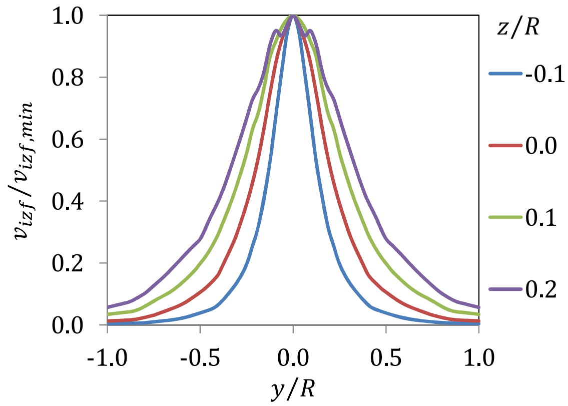

(b) Self-similarity of the normalized profile

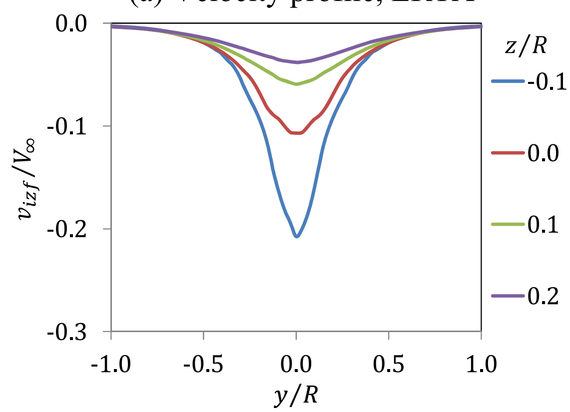

(c) Velocity profile, RTA

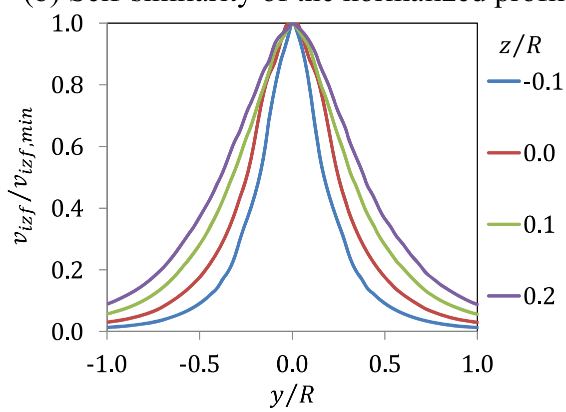

(d) Self-similarity of the normalized profile

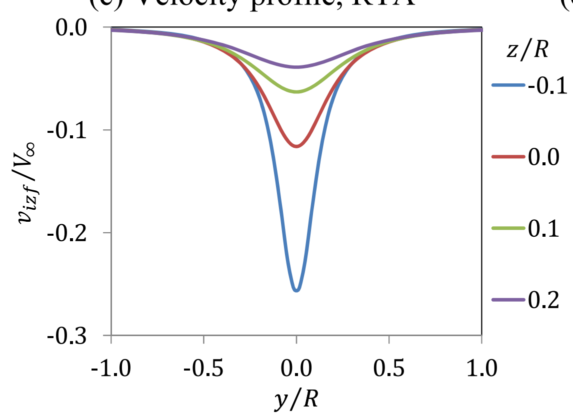

(e) Velocity profile, HART

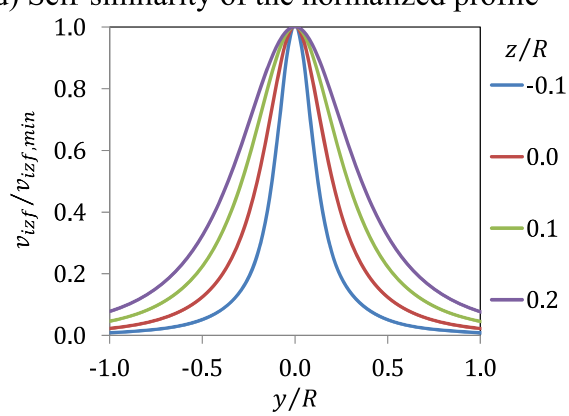

(f) Self-similarity of the normalized profile

Figure 23: Lateral velocity profiles and their dependence on z; $\alpha = 0°$.

3.3 A Generic Example

For better understanding, the underlying idea of the model is explained with a simple example. Based on the velocity distributions observed in figures 18 to 23, the principle is an upwash at the front part of the fuselage, a downwash at the rear part, and an upwash or downwash over the tail boom. Using the superposition principle, one function for each of these effects may be applied; function parameters are the magnitude, the spatial position of the peak value, and a factor adjusting the shape of the function (see fig. 24). Each individual function approaches zero far away from its peak value and is written as

$$v_{izf}/V_\infty = A/[1 + S_x(x - x_0)^n]$$

The amplitude, A, shape parameter, S_x, peak position, x_0, and the exponent, n, for the various contributions are given in table 3.

The shape factor allows for a wide variation of appearances and it can adapt to the velocity distributions observed. The proper values for the parameters can be identified by performing a least squares fit to the data. Because of the superposition principle, this must be done simultaneously for all functions applied. Initial values for the parameters may be arbitrary, but values derived from observation of the CFD data accelerate the identification process.

Table 3: Parameters used for generation of figure 24.

	A	S_x	x_0	n
Upwash	–1	10	–0.4	2
Downwash	1	50	0.25	2
Tail boom	–0.5	20	1	6

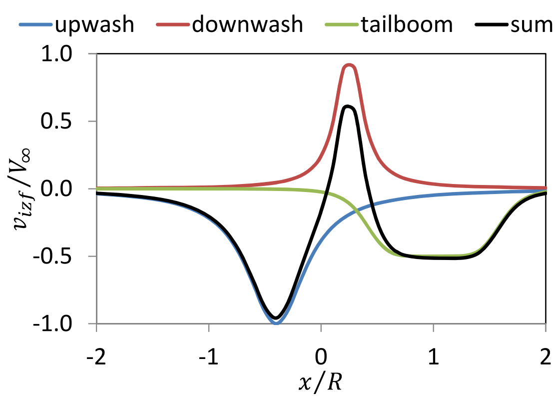

Figure 24: Superposition principle of the model.

4. Semi-Empirical Model of Fuselage-Induced Velocities

4.1 LRTA and RTA Fuselages

An in-depth description of the model is given in van der Wall.[50] Physical considerations from potential theory require that all fuselage-induced velocities must die out far from the fuselage. The magnitude is proportional to $1/r^2$, as seen by the data in figures 16 to 18 or in figure 21. In all angle-of-attack conditions shown, an upwash is found in the front region and a downwash in the rear region, their size and intensity depending on the angle of attack. Therefore, the hypothesis is made to use the superposition principle, i.e., to model the upwash and the downwash by separate functions and then add their results. The general appearance of fuselage-induced velocity isolines as seen in figure 16 or figure 18, is elliptic with different extents in x- and y-directions. This suggests using a function such as

$$\frac{v_{izf}}{V_\infty} = \sum_{j=u,d,t} \frac{A_j}{S_{jx}\left(x/R - x_{j0}/R\right)^2 + S_{jy}(y/R - y_{j0}/R)^2 + 1} \tag{1}$$

wherein A represents the peak value, S_x is a decay factor for the profile of the fuselage-induced velocity distribution in x-direction, S_y is a respective decay factor in the y-direction, and x_0 is the peak position on the x-axis. The sum and its subscript j represent the superposition of individual contributions of the upwash (u), downwash (d), and tail boom (t). For cases with zero side-slip angle, the fuselage-induced velocities are symmetric in the lateral direction. The y-coordinate of the peak value is zero; therefore, y_0 can be eliminated from the formula.

The parameter identification is performed in three steps. First, every z plane for each angle of attack is modeled independently using Eq. (1). Therefore, the dependency of each of the four parameters, $A, S_x, S_y,$ and x_0, for both the upwash function and the downwash function (in total: eight parameters for each of the eight angles of attack times four planes, z/R, in each equals $8 \times 8 \times 4 = 256$ parameters) can be plotted versus z/R for each angle of attack as shown in figure 25 for the upwash and downwash magnitude, in figure 26 for the position of the upwash and downwash peak values, and in figure 27 and figure 28 for the shape factors of the upwash and downwash functions in x- and y-direction.

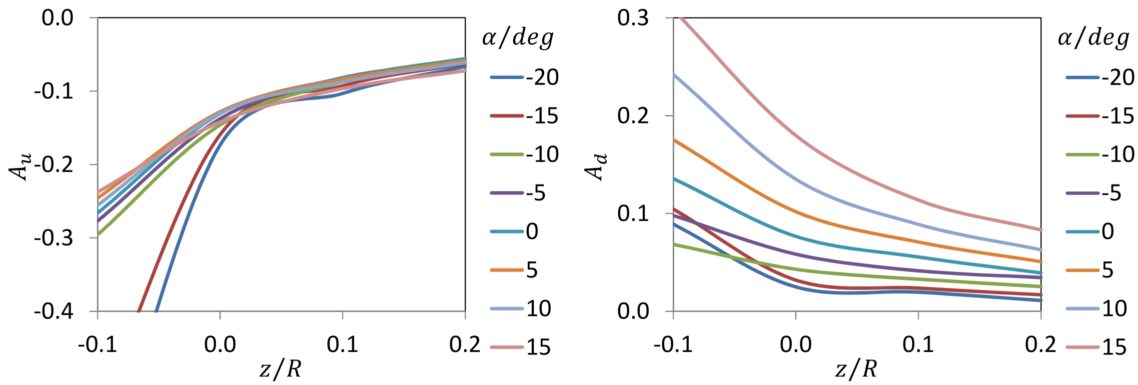

(a) Upwash magnitude (b) Downwash magnitude

Figure 25: Upwash and downwash magnitude dependence on z/R, step 1, RTA.

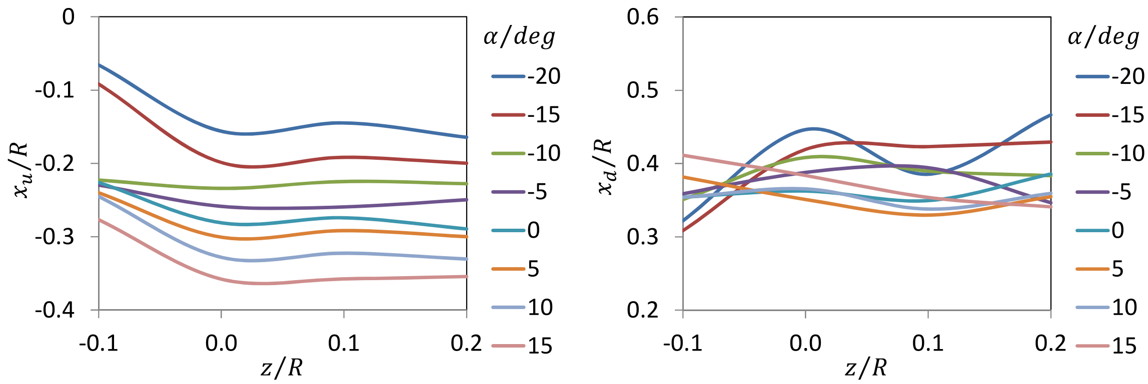

(a) Upwash position (b) Downwash position

Figure 26: Upwash and downwash position dependence on z/R, step 1, RTA.

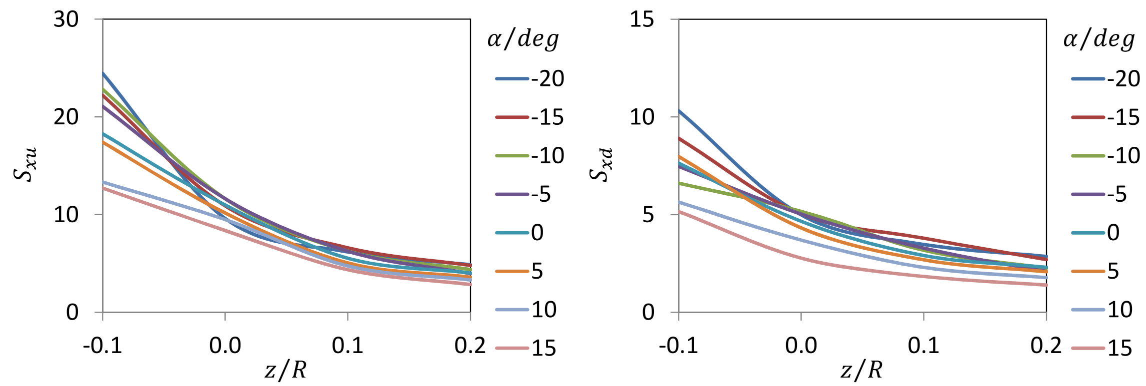

(a) Upwash shape factor, x (b) Downwash shape factor, x

Figure 27: Upwash and downwash x shape factor dependence on z/R, step 1, RTA.

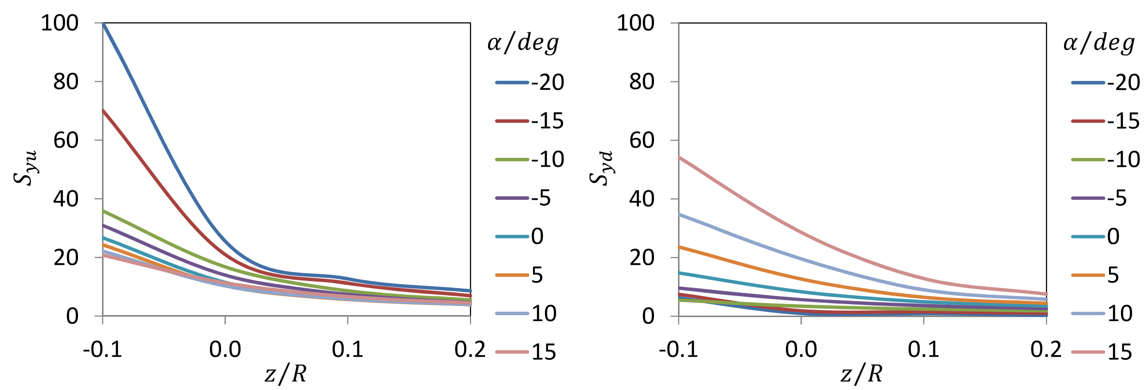

(a) Upwash shape factor, y (b) Downwash shape factor, y

Figure 28: Upwash and downwash y shape factor dependence on z/R, step 1, RTA.

It is found that in general all the A, S_x, and S_y parameters show a dependency as given by the formulae in Eq. (2), while the peak position, x_0, of upwash and downwash are found essentially independent on z/R. The magnitude, A, and the shape factors, S_x and S_y, all are proportional to the inverse of the distance to the fuselage, such that they may be modeled in the form

$$A_j = \frac{A_{j0}}{S_{jA0}\left(z/R - z_0/R\right)^2 + 1}; \quad S_{jx} = \frac{S_{jx0}}{\left(z/R - z_0/R\right)^2}; \quad S_{jy} = \frac{S_{jy0}}{\left(z/R - z_0/R\right)^2} \quad j = u,d,t \tag{2}$$

Therein, S_{A0} represents the respective decay factor for the variation of A in z-direction, with A_0 as the amplitude at $z = z_0$, and z_0 is the position of the maximum of A on the z-axis, which is considered the center of the fuselage, measured from the hub center as the reference coordinate system. The reason for doing so is found in potential theory: the distribution of sources and sinks to generate a contour of fuselage bodies is placed on their respective centerline. By intention S_x and S_y become infinite at $z = z_0$, which allows a smooth variation from upwash on the upper side of the fuselage to downwash on the lower side because then the fuselage-induced velocity becomes zero at $z = z_0$ to avoid a singularity.

The second step of parameter identification is to combine Eqs. (1) and (2) in order to achieve an analytical representation for the entire (x, y, z)-domain.

$$\frac{v_{izf}}{V_\infty} = \sum_{j=u,d,t} \frac{\dfrac{A_{j0}}{S_{jA0}\left(z/R - z_0/R\right)^2 + 1}}{\dfrac{S_{jx0}}{\left(z/R - z_0/R\right)^2}\left(x/R - x_{j0}/R\right)^2 + \dfrac{S_{jy0}}{\left(z/R - z_0/R\right)^2}\left(y/R - y_{j0}/R\right)^2 + 1} \tag{3}$$

This adds 1 parameter for each upwash and downwash function for a total of 10 parameters for each of the 8 angles of attack (reducing the total number to $10 \times 8 = 80$ parameters). All those parameters are then plotted versus the angle of attack to identify this last dependency as shown in figure 29 and figure 30. For convenience the angle of attack has been made nondimensional through division by 90° such that it becomes ± 1 for the extremes of $\alpha = \pm 90°$.

Most of the parameters are essentially linear or quadratic in α, such that the following relations can be used to approximate them (either α or $\alpha/90°$ may be used).

$$\begin{aligned} A_{j0} &= A_{j00} + A_{j01}\alpha + A_{j02}\alpha^2; \quad S_{jy0} = S_{jy00} + S_{jy01}\alpha + S_{jy02}\alpha^2; \\ S_{jA0} &= S_{jA00} + S_{jA01}\alpha; \quad S_{jx0} = S_{jx00} + S_{jx01}\alpha; \quad x_{j0} = x_{j00} + x_{j01}\alpha \quad j = u,d,t \end{aligned} \tag{4}$$

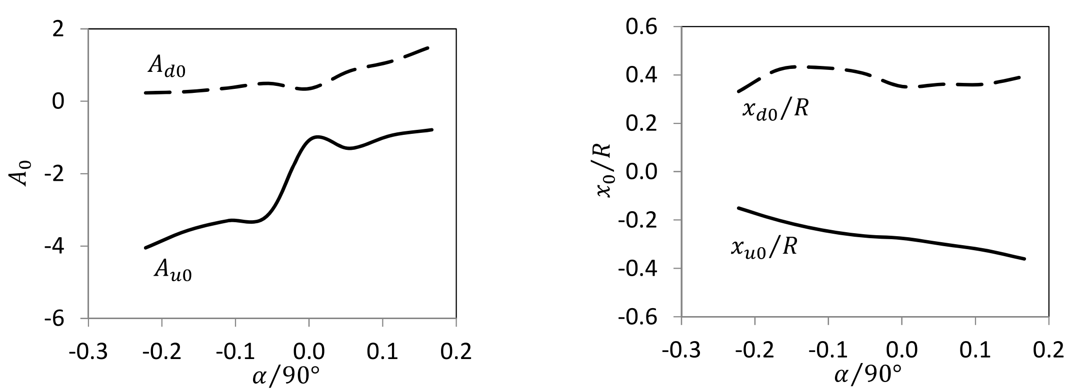

(a) Upwash and downwash magnitude (b) Upwash and downwash position

Figure 29: Upwash and downwash magnitude and position dependence on α, step 2, RTA.

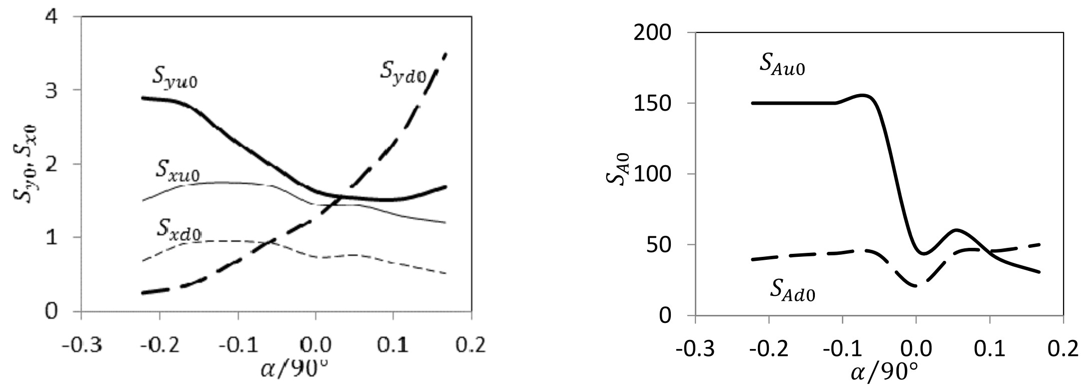

(a) Upwash and downwash shape factor, x and y (b) Upwash and downwash shape factor, z

Figure 30: Upwash and downwash x, y, and z shape factor dependence on α, step 2, RTA.

The third and final step of parameter identification is to identify these additional parameters, wherein A_{00} is the magnitude for $\alpha = 0°$, A_{01} is the variation linear proportional to α, and A_{02} is the variation proportional to the square of α, etc., as given in Eq. (4). Similarly, x_{00} is the peak position for $\alpha = 0°$, and x_{01} is the variation linear proportional to α as seen in figure 29. In total, only 22 parameters result that all have a physical interpretation, and now the entire flow field within the volume of the data given ($-1 \leq x/R \leq +1, -1 \leq y/R \leq +1,$ and $-0.1 \leq z/R \leq +0.2$) can be analytically represented by the math model for all angles of attack $-20° \leq \alpha \leq +15°$ and any in between.

The remaining error between the model and the CFD data can be expressed in percent of the free-stream velocity. Another measure that is likely better suited is to refer the error to the peak-to-peak range of the data within every individual plane, z/R, and separately for every individual operating condition. This represents the percent error of the individual data range.

A sufficient degree of accuracy in average is obtained if the error relative to the peak-to-peak data range within each individual plane is ≤5 percent. This goal is achieved as shown in figure 31, where the mean relative error of the LRTA and the RTA is shown in (a) and (b), respectively, after the first step of parameter identification, and in figure 32 (a) and (b), respectively, after step 3. The smallest errors are obtained in step 1 because this allows the largest degree of freedom with one parameter set for each individual plane, z/R. Step 3 combines all dependencies on $x, y, z,$ and α in one fully analytical model with a few parameters only, thus increasing the overall error. However, it is still below the goal of 5 percent relative error.

Also, the reference to the individual peak-to-peak data range within the planes, z/R, highlights that the mean error is about the same independent of z/R. The minimum error is obtained around $\alpha = 0°$ as might be expected because these are the most "trivial" cases, while any deviation from this condition in terms of angle of attack causes an increase of the mean error, i.e., the fuselage-induced velocity distributions contain nonlinearities that cannot be represented by the simple analytical formulation. This would require a more sophisticated model. However, for the purposes of the model (rotor trim, rotor performance, and wake deflection) this degree of accuracy is deemed sufficient.

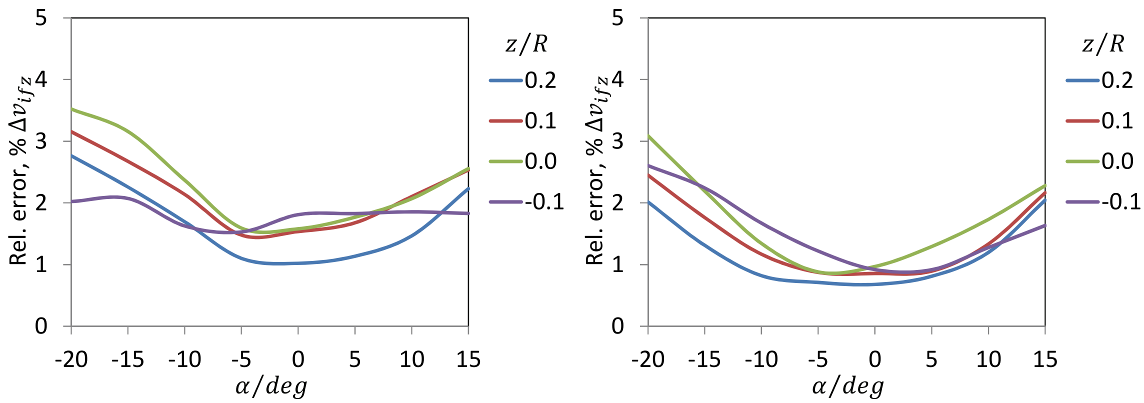

(a) LRTA (b) RTA

Figure 31: Relative error of the model for the LRTA and RTA fuselages, step 1.

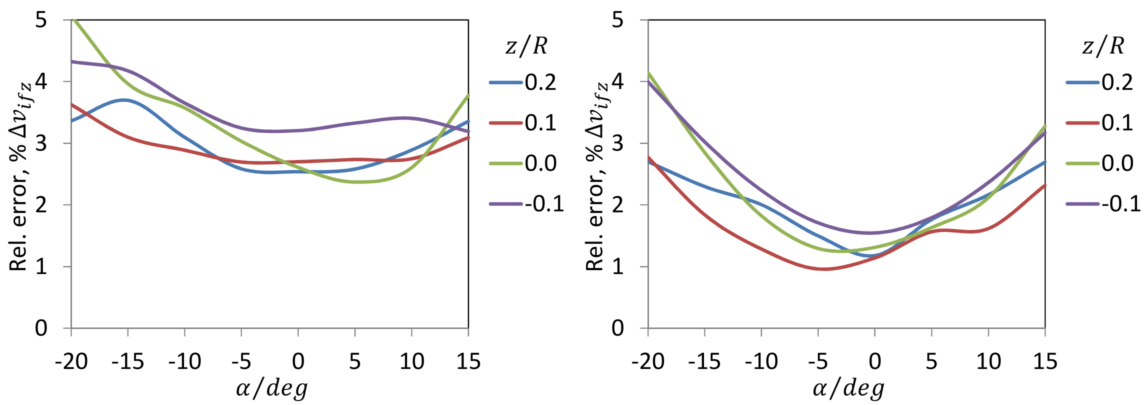

(a) LRTA (b) RTA

Figure 32: Relative error of the model for the LRTA and RTA fuselages, step 3.

4.2 HART Fuselage

Within the small range of angles of attack of the LRTA and RTA fuselages, the same dependence would be sufficient for the HART. Yet, the HART fuselage operational conditions cover a much wider range of angle of attack (and of side-slip angles) than the LRTA and RTA fuselages, and the dependencies of the model parameters on angle of attack and side-slip are much more nonlinear and therefore require a different formulation. Figure 33 shows the fuselage-induced velocity profiles from figure 21 extended to the entire range of angles of attack. As long as the top of the fuselage is on the windward side the flow appears undisturbed, but when it is on the leeward side flow separation shows up in the volume of interest with large turbulences.

A similar observation is made in side-slip conditions as given in figure 34 for the lateral distribution of the fuselage-induced velocities. Again, the leeward side shows strong flow separation and associated turbulence. Because the goal of the analytical model is to provide the steady mean part of the flow, all these disturbances need to be suppressed during the parameter identification process by ignoring them entirely or by reducing the weight of the local errors.

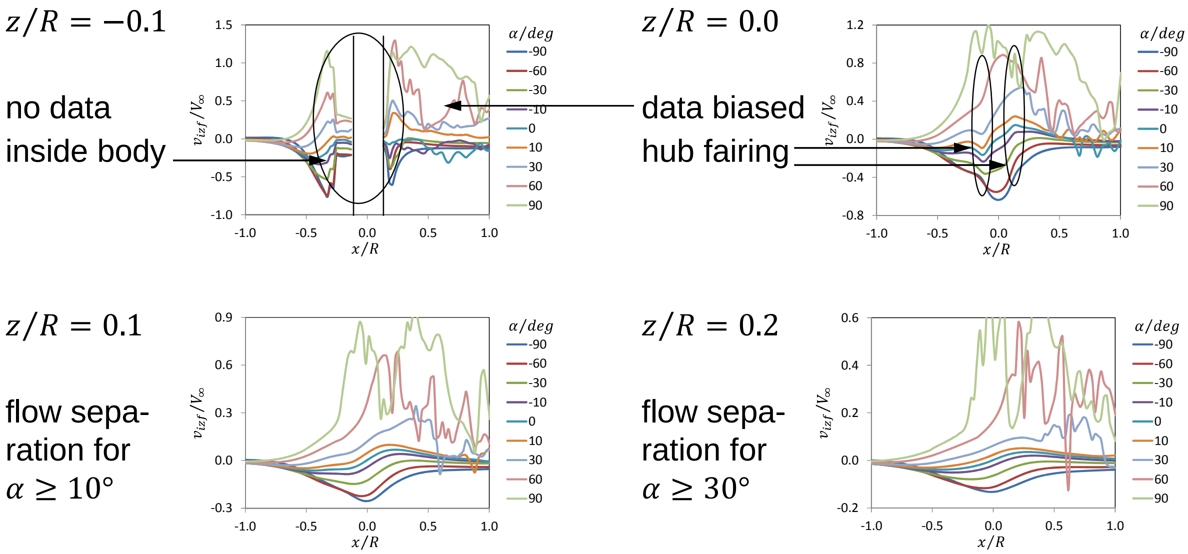

Figure 33: Dependence of fuselage-induced velocity profiles on angle of attack, $\beta = 0°$.

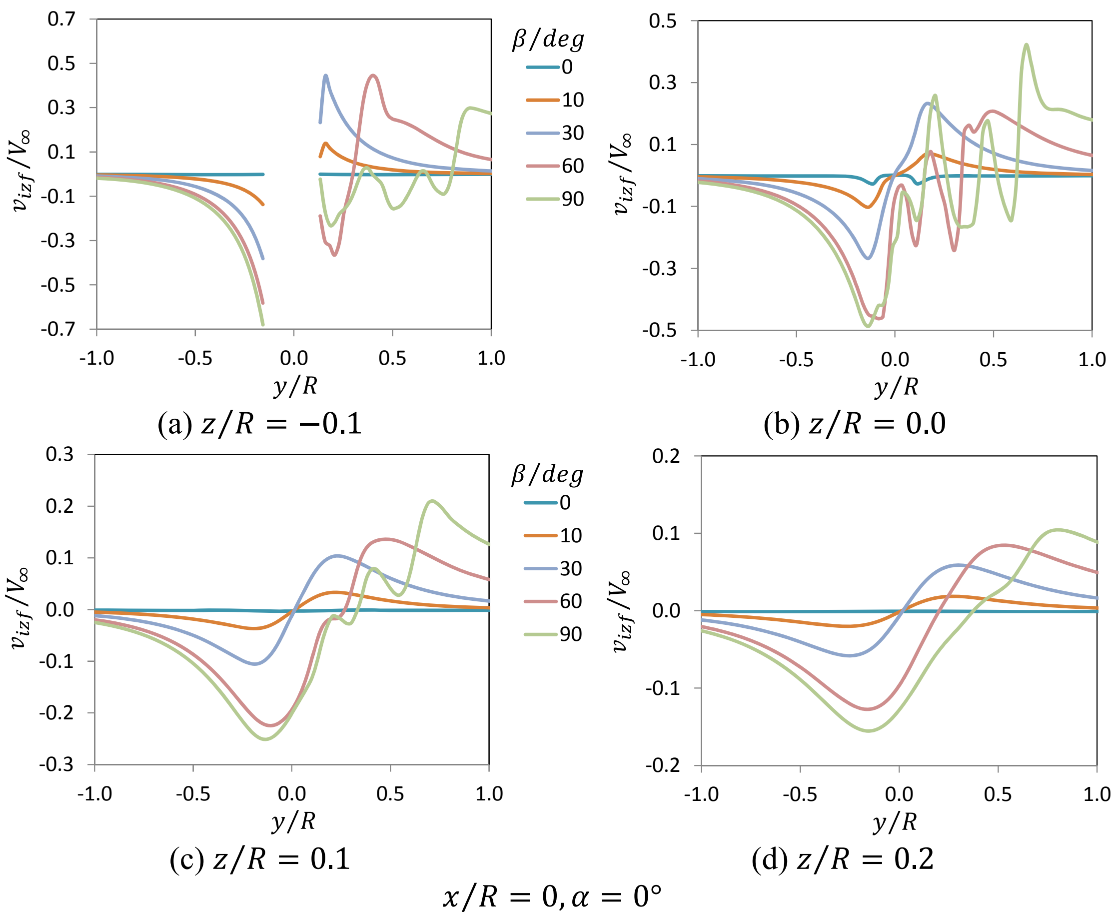

Figure 34: Dependence of fuselage-induced velocity profiles on side-slip angle, HART.

In addition to the upwash and downwash functions used for the LRTA and RTA fuselages, the long, thick tail boom of the HART fuselage shows up with its own contributions large enough to require special attention, thus an additional function is set up for the tail boom influence, superimposed to the other two contributions. The x-position of the tail boom function is pre-set to $x_t/R = 1.0$, assuming a further extension aft of this in a symmetrical way. Because the tail boom is much longer than wide, its impact in x-direction can better be represented by a larger exponent than 2 in Eq. (1); here 6 is chosen instead, but this is subject to judgment. This exponent guarantees a steep decay towards the front of the rotor, and the contribution of the tail boom is practically zero in the front of the disk.

In side-slip conditions the upwash moves to the windward side and the downwash to the leeward side (see fig. 34; the upwash is located around $y/R \cong -0.1$, and the downwash position is largely depending on side-slip angle and varies between $y/R \cong 0.1$ for small β to $y/R \cong 0.7$ for large β). Both move from the fore and aft position roughly to the center at $x/R \cong 0$ for quartering flight, shown later in figure 50.

The tail boom now as well has two features instead of one: it splits into an upwash on the windward side and a downwash on the leeward side (see fig. 35). Therefore, in side-slip conditions the tail boom requires two functions, one for each effect. For $\beta = 60°$ and $y/R > 0.3$ the curve diverges from all others because of flow separation passing this area, also seen later in figure 50, and can be ignored. The same observations can be made for the tail boom as for the fuselage body (where the downwash on the leeward side is located much farther away from it than the upwash on the windward side). The tail boom-induced upwash develops only for $\beta \neq 0°$ and moves with increasing side-slip to $y/R \cong -0.3$ while the downwash, already existing for $\beta = 0°$, moves to $y/R \cong 0.7$, more than twice as far away from the fuselage. The magnitudes of tail boom-induced upwash and downwash also increase with the side-slip angle.

The rest of the procedure is identical to the LRTA and RTA fuselages described previously. In the first step the model is applied to each plane, z/R, and for every angle of attack or side-slip separately. In the second step, the dependence with respect to z/R is identified in the same manner as for the LRTA and RTA, still independently on α and β. In the following, the resulting dependencies on these angles are shown. First, the model is set up for the angle-of-attack range only (no side-slip); second, the model is set up for the side-slip variation (no angle of attack). Finally, a blending for any combination of α and β is established.

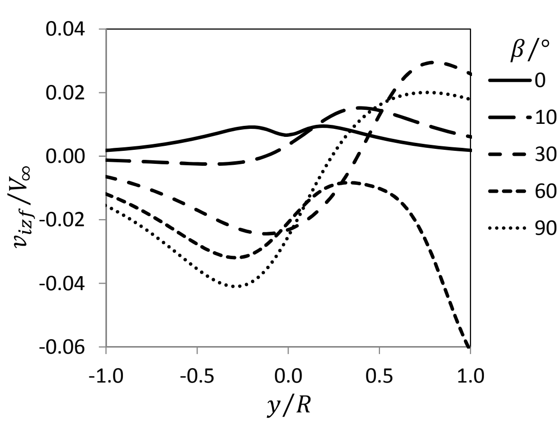

Wind from left, $x/R = 1, z/R = 0.2,\ \alpha = 0°$

Figure 35: Dependence of tail boom-induced velocity profiles on side-slip angle, HART.

4.2.1 Angle-of-Attack Variation

All parameters' variation with respect to angle of attack are shown in figure 36 for the magnitude of the upwash, downwash, and tail boom function; in figure 37 for the x-position of the upwash and downwash (tail boom function is set to $x_t/R = 1.0$) and the shape factor of the peak upwash and downwash with respect to z; and in figure 38 for the shape factors in x- and y-direction.

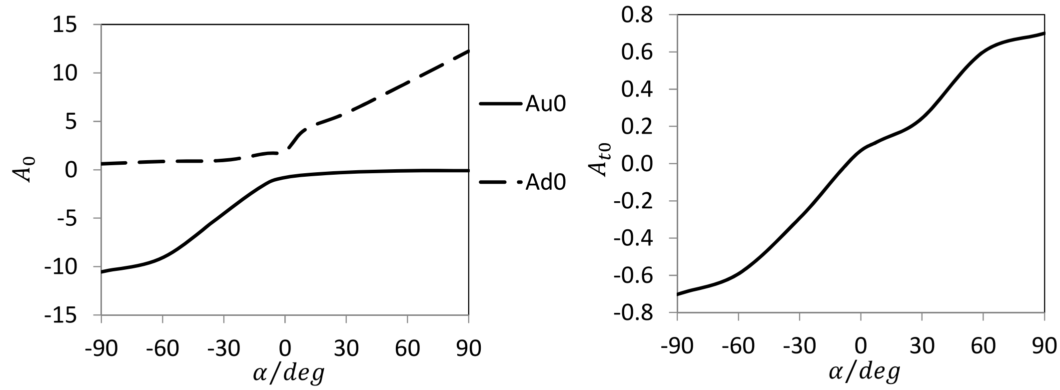

(a) Upwash and downwash (b) tail boom

Figure 36: Dependence of fuselage-induced velocity magnitudes on $\alpha, \beta = 0°$.

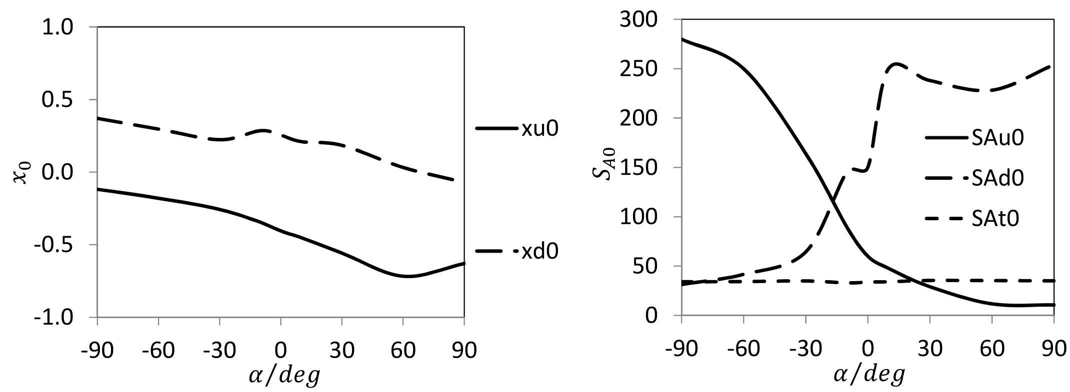

(a) Upwash and downwash position (b) Shape factor, z

Figure 37: Dependence of peak velocity position and shape factor (z) on $\alpha, \beta = 0°$.

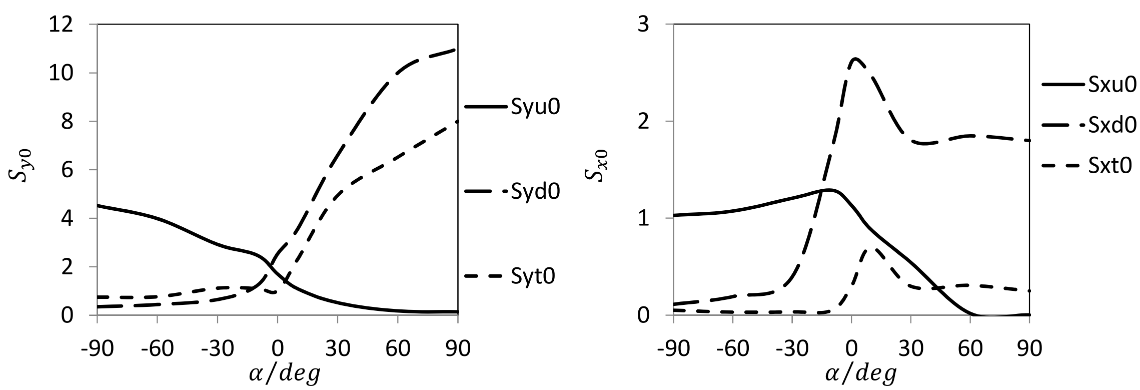

(a) Shape factor, y (b) Shape factor, x

Figure 38: Dependence of shape factors (y, x) on $\alpha, \beta = 0°$.

Most of the dependencies with respect to α show asymptotic behavior to both extremes of the angle of attack with a continuous variation between, while the position of the upwash and downwash appears linear in α. This behavior can be described by two generic functions

$$X^{-} = X_0 \left[\frac{1}{X_1(1-\alpha/90)^6+1} - \frac{1}{X_1+1} \right] \quad \text{or} \quad X^{+} = X_0 \left[\frac{1}{X_1(1+\alpha/90)^6+1} - \frac{1}{X_1+1} \right]$$
$$\text{with } X = A_{j0},\ S_{jA0},\ S_{jx0},\ S_{jy0} \tag{5}$$
$$x_{j0} = x_{j00} + x_{j01}\alpha; \qquad j = u, d, t$$

For convenience, α is made nondimensional in order to vary from –1 to 1. The third and final step of parameter identification is to identify these additional parameters, wherein all parameters indexed by 00 denote those for the case of $\alpha = 0°$, i.e., A_{00} is the magnitude for $\alpha = 0°$, A_{01} is the variation proportional to α, etc., as given in Eq. (4). Similarly, x_{00} is the peak position for $\alpha = 0°$, x_{01} is the variation linear proportional to α as seen in figure 37. In total, only 28 parameters result that all have a physical interpretation, and now the entire flow field within the volume of the data given ($-1 \leq x/R \leq +1, -1 \leq y/R \leq +1,$ and $-0.1 \leq z/R \leq +0.2$) can be analytically represented by the math model for all angles of attack $-90° \leq \alpha \leq +90°$ and any in between. A sufficient degree of accuracy in average is obtained, if the error relative to the peak-to-peak data range within each individual plane in the undisturbed range of data is less than or equal to 5 percent. This goal is achieved as shown in figure 39.

Also, because of the nature of the functions used (see Eqs. (1) and (2)), the fuselage-induced velocities asymptotically approach zero for $(x, y, z)/R \rightarrow \pm\infty$ as required by potential theory. Therefore, the model can also be used outside of the volume of data it is based on. If it is also desired to also approximately compute the fuselage-induced velocities below the fuselage—although no data are extracted to build up a separate model for this region—the following consideration can be applied. Because of the approximate symmetry of the fuselage body with respect to the plane, z_0/R, the flow field below it can be assumed to be

$$\frac{v_{izf}}{V_\infty}(\alpha, z < z_0) = -\frac{v_{izf}}{V_\infty}(-\alpha, z > z_0) \tag{6}$$

using the same coefficients as for the model generated so far.

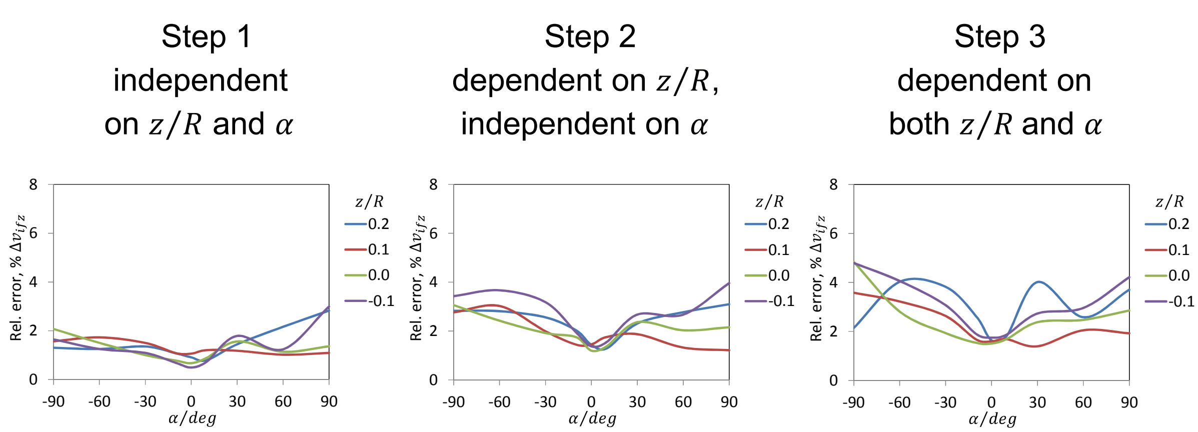

Figure 39: Mean relative error for the angle of attack variation, $\beta = 0°$.

4.2.2 Side-Slip Angle Variation

After the full formulation for the entire range of angle of attack is done, its coefficients for $\alpha = 0°$ are used as the basis of the side-slip-angle modeling. For these cases the same sequence of parameter identification is performed again: first, fully independently for each β and $z/R =$ construction; second, the dependency on z/R is established; third, the full range of side-slip angles including $\alpha = \beta = 0°$ is done. Note that in side-slip conditions the tail boom-induced velocity field is represented by two functions, where one of them is part of the modeling in α and the other one is only present for $\beta \neq 0$.

All parameters' variation after step 2 (analytical representation with respect to z) with regard to side-slip angle are shown in figure 40 for the magnitude and the shape factor in z-direction of the upwash, downwash, and tail boom function; in figure 41 for the x-positions (tail boom function is set to $x_{tu}/R = x_{td}/R = 1.0$) and the y-positions of the upwash and downwash; and in figure 42 for the shape factors in x- and y-direction.

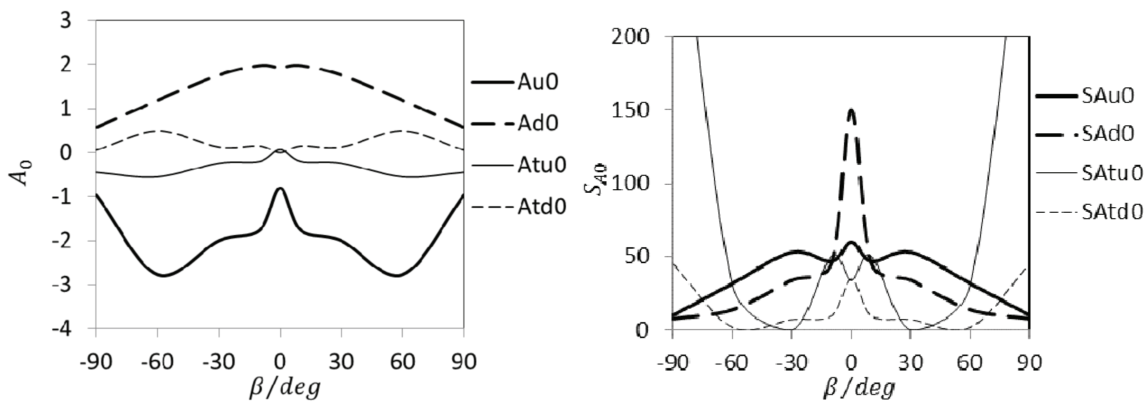

(a) Upwash and downwash (fuselage + tail)

(b) Shape factor upwash and downwash (fuselage + tail), z

Figure 40: Dependence of velocity magnitudes and shape in z-direction on $\beta, \alpha = 0°$.

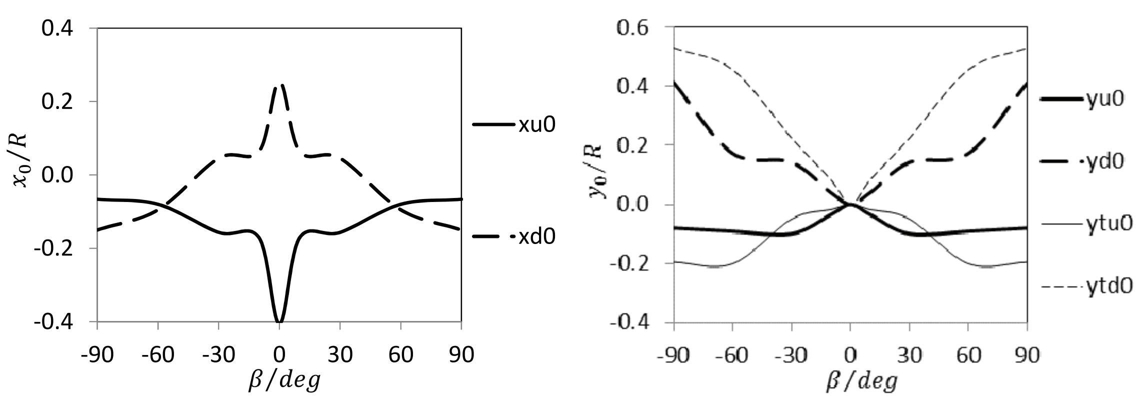

(a) Upwash and downwash x-position

(b) Upwash and downwash y-position (fuselage + tail)

Figure 41: Dependence of position of velocity magnitudes on $\beta, \alpha = 0°$.

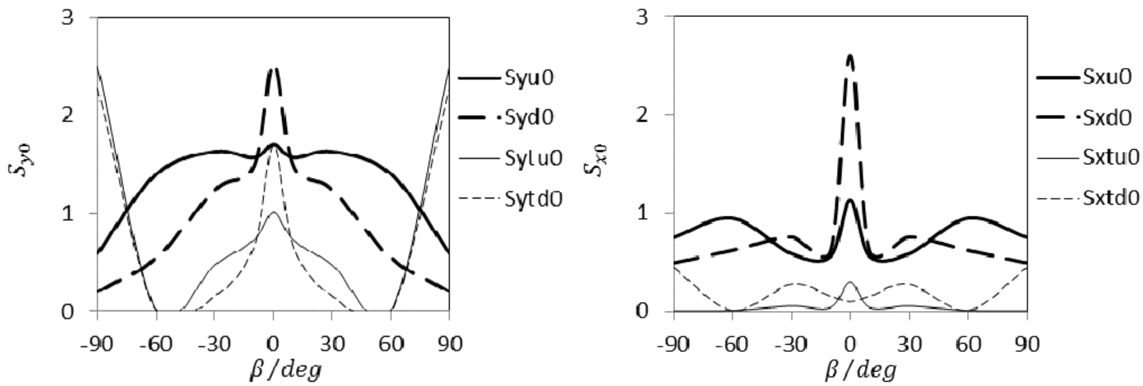

(a) Shape factor, y (fuselage + tail) (b) Shape factor, x (fuselage + tail)

Figure 42: Dependence of shape factors (y, x) on $\beta, \alpha = 0°$.

It appears that all parameters identified within step 2 vary essentially proportional either to $\sin|\beta|$ or to $1 - \cos\beta$.

$$
\begin{aligned}
X^s = X_0 + X_1 \sin|\beta| \quad \text{or} \quad X^c = X_0 + X_1(1-\cos\beta) \\
\text{with} \quad X = A_0,\ S_{A0},\ S_{x0},\ S_{y0},\ x_0,\ y_0
\end{aligned}
\tag{7}
$$

With these formulae the side-slip angle can be introduced analytically into all parameters of the model, and the errors obtained after step 3 for the final model are shown in figure 43. They are a little larger than for the angle-of-attack variation given in figure 39, but the flow separation occurring in side-slip is stronger and covers a wider region than those of the angle-of-attack variation. The mean relative errors here peak at 6 percent of the data range within each plane, z/R, for the range $30° \leq |\beta| \leq 90°$, compared to 5 percent for the angle-of-attack variation, which is deemed acceptable within the scope of this model.

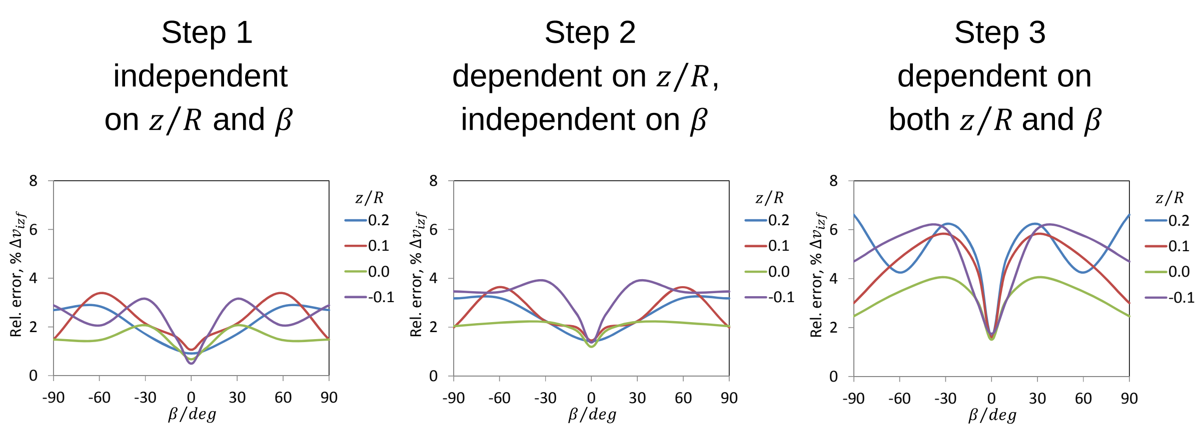

Figure 43: Mean relative error for the side-slip-angle variation, $\alpha = 0°$.

4.2.3 Blending of Angle of Attack and Side-Slip Angle for Arbitrary Combinations

No CFD data are available for mixed operational conditions including angle of attack and side-slip simultaneously. However, some physical considerations help in setting up a blending from the model developed only for α variations and one developed only for β variations, because both of them have an identical parameter set at their intersection of $\alpha = \beta = 0°$. Therefore, only the Δ values of the parameters, set up separately for α and β, need to be blended. The blending is set up in the following way:

$$f_\beta = \cos\alpha \frac{|\beta|}{|\alpha| + |\beta| + 0.0001}; \qquad f_\alpha = 1 - f_\beta \tag{8}$$

All parameters of the model for α variations are then multiplied with f_α, and all parameters of the model for β variations are multiplied with f_β. All $\beta \neq 0°$ with $\alpha = 0°$ cases result in $f_\beta \approx 1$ and $f_\alpha \approx 0$ such that the model for β variations is fully active; all $\alpha \neq 0°$ with $\beta = 0°$ cases result in $f_\beta = 0$ and $f_\alpha = 1$ such that the model for α variations is fully active. All cases with $|\alpha| = 90°$ for whatever β results again in $f_\beta = 0$ and $f_\alpha = 1$ such that the model for α variations is fully active. Any combination in between results in a smooth blending of the parameters from one model to the other.

Keep in mind that this blending is arbitrary to some degree, but results appear quite physical; verification is needed with further CFD computations for a few combined angle-of-attack and side-slip conditions.

5. Comparison of the Model With CFD Data

5.1 Range of Small Angles of Attack, No Side-Slip

For the plane $z/R = +0.1$, a direct comparison of the CFD data with those generated by the model using Eqs. (1), (2), and (4) is given in figure 44 for $\alpha = -20°$ (LRTA and RTA only, no data from HART available). In figure 45 this is done for $\alpha = -10°$, in figure 46 for $\alpha = 0°$, and in figure 47 for $\alpha = +10°$ (all for the LRTA, RTA, and HART fuselages for direct comparison).

In figure 44 ($\alpha = -20°$, so mainly upwash is expected in this nose-down condition) it can be seen first, that the peak value of upwash of the LRTA is little larger than that of the RTA, and second, that the upwash isoline appearance of the LRTA is more stretched in x-direction while the appearance of the RTA is more circular. Also, the LRTA shows some small downwash in the right part of the figure, which is not present in the RTA data. All these issues are essentially reproduced by the model.

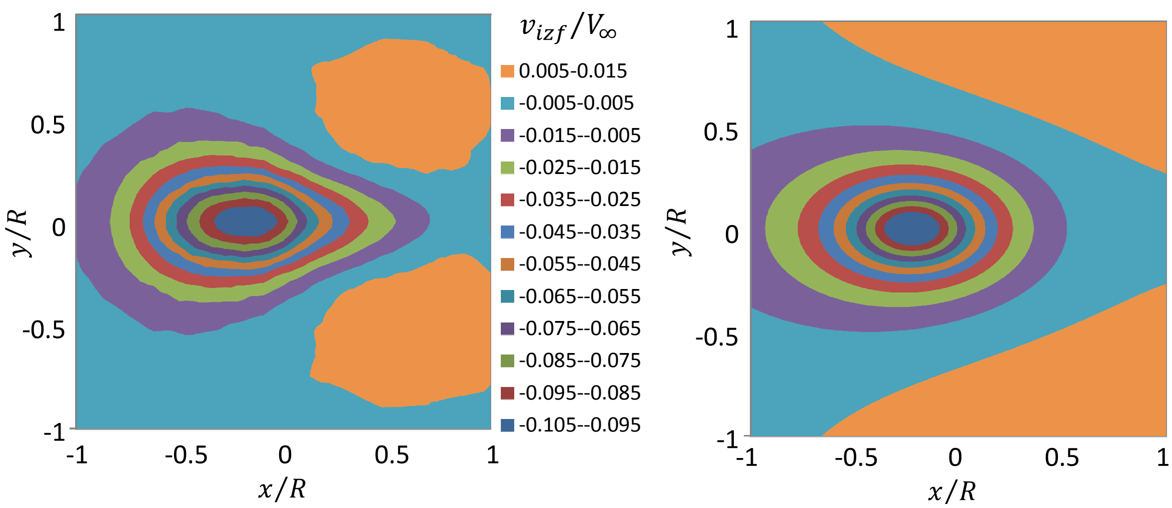

(a) LRTA: CFD data (left), model (right)

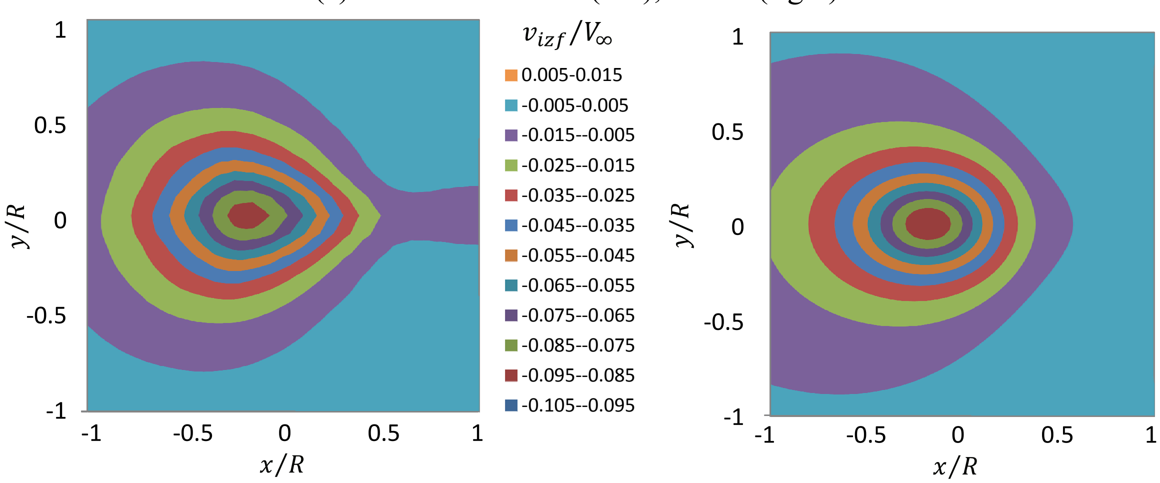

(b) RTA: CFD data (left), model (right)

Figure 44: Comparison of CFD data with model reconstruction, $\alpha = -20°, z = 0.1R$.

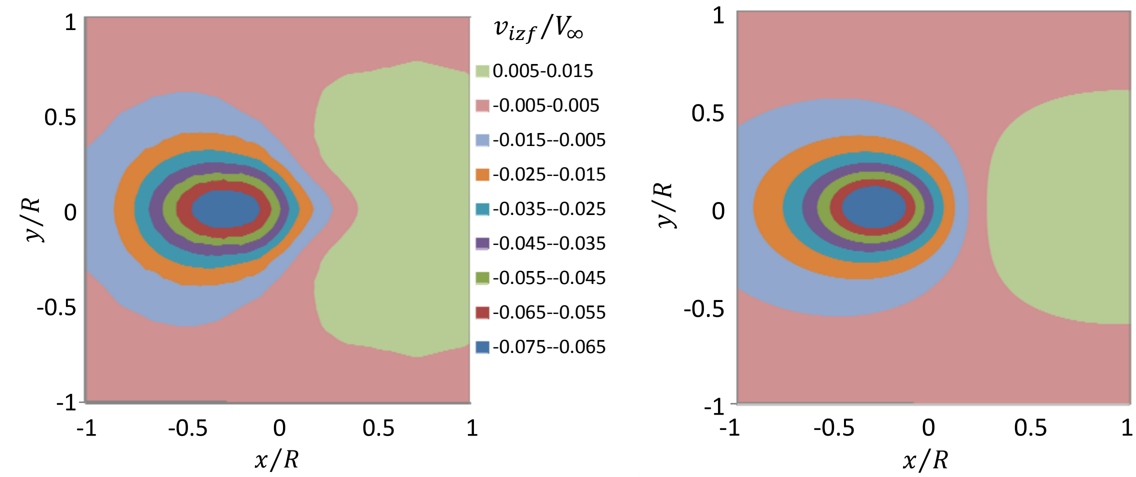

(a) LRTA: CFD data (left), model (right)

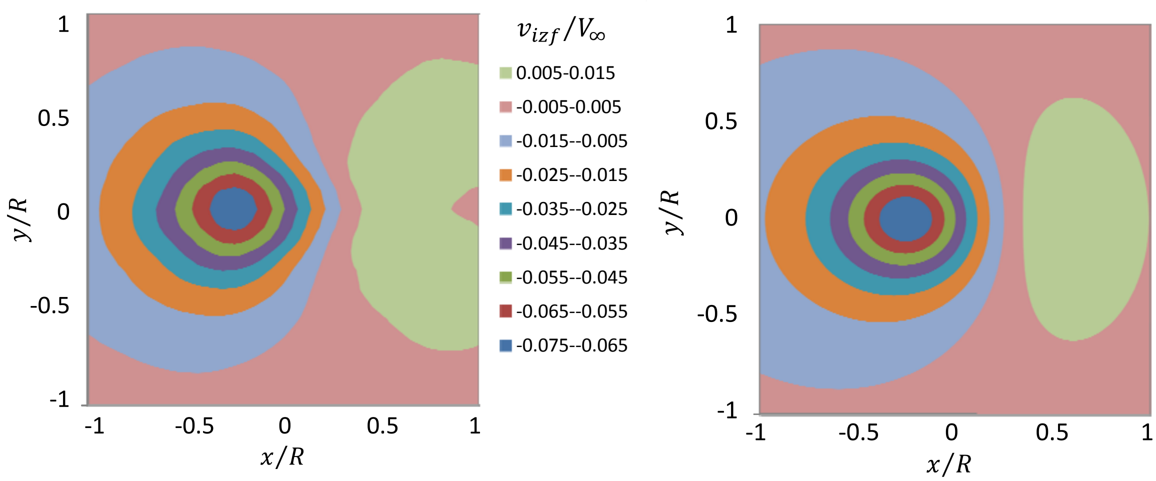

(b) RTA: CFD data (left), model (right)

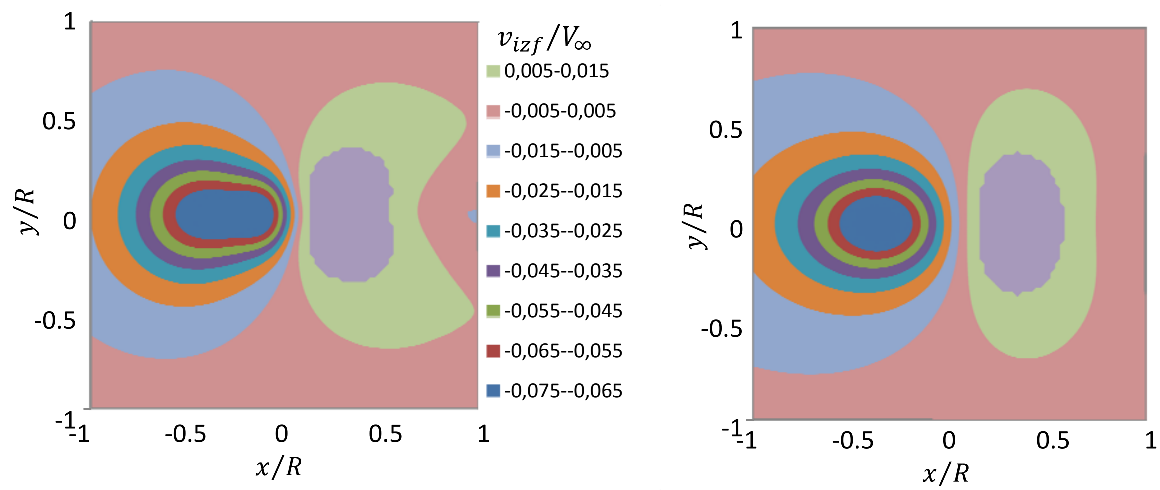

(c) HART: CFD data (left), model (right)

Figure 45: Comparison of CFD data with model reconstruction, $\alpha = -10°, z = 0.1R$.

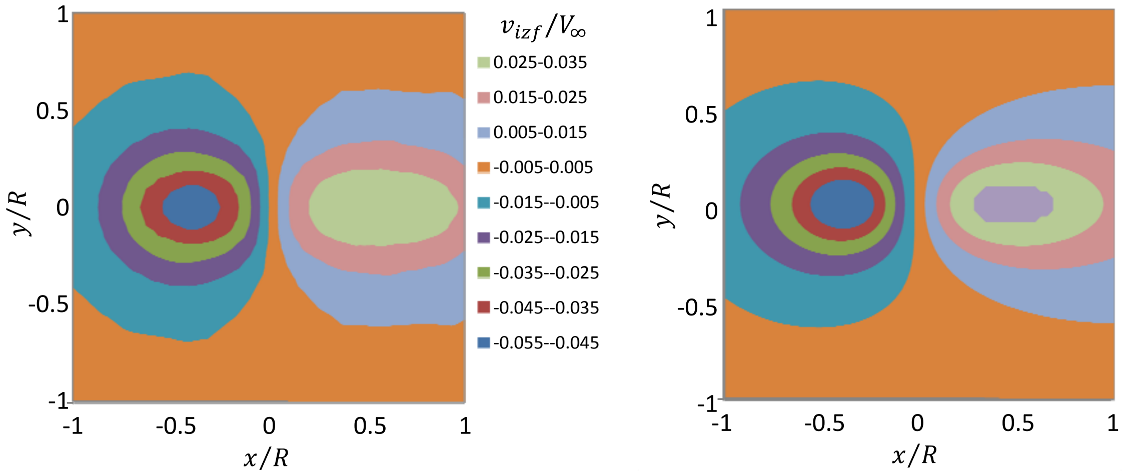

(a) LRTA: CFD data (left), model (right)

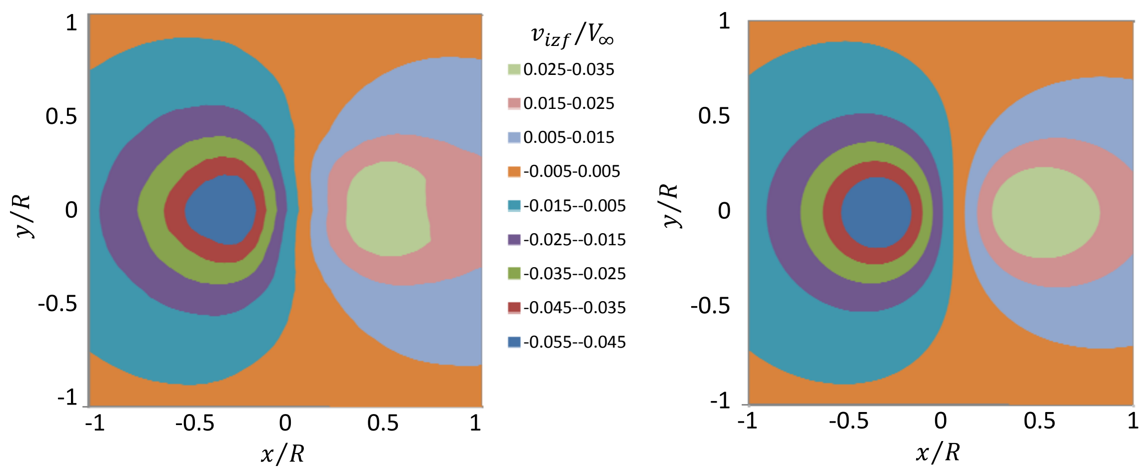

(b) RTA: CFD data (left), model (right)

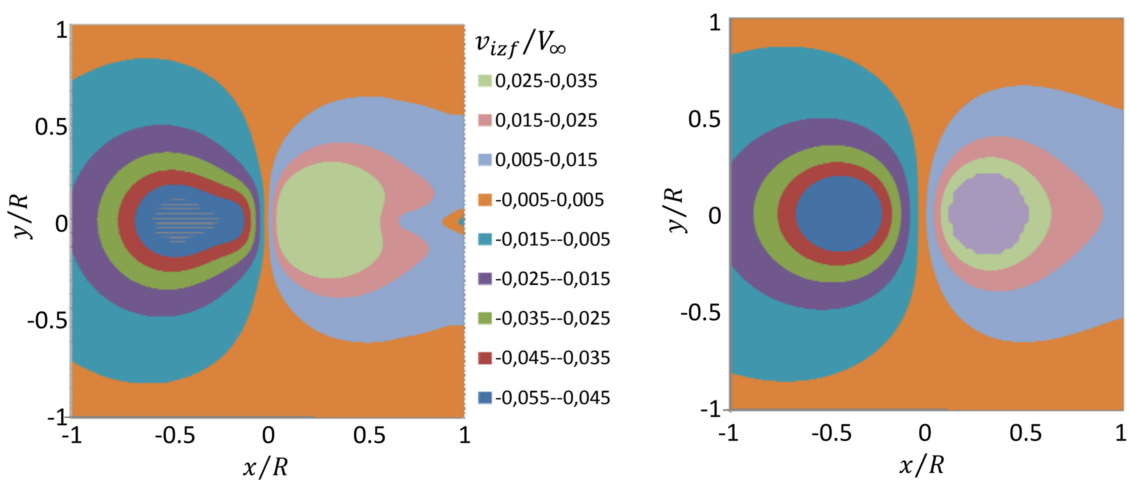

(c) HART: CFD data (left), model (right)

Figure 46: Comparison of CFD data with model reconstruction, $\alpha = 0°, z = 0.1R$.

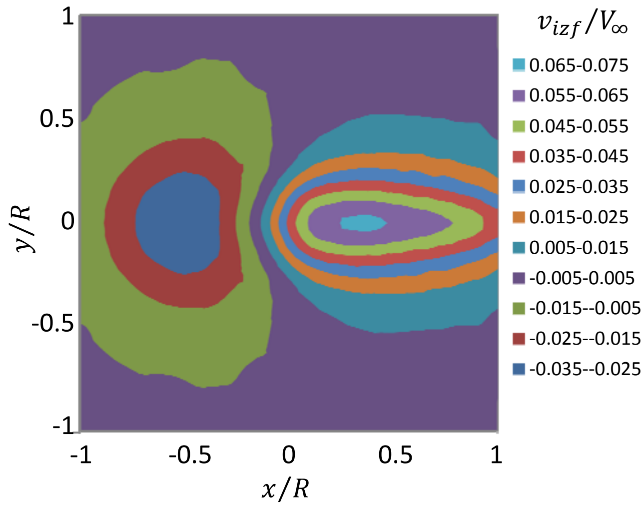

(a) LRTA: CFD data (left), model (right)

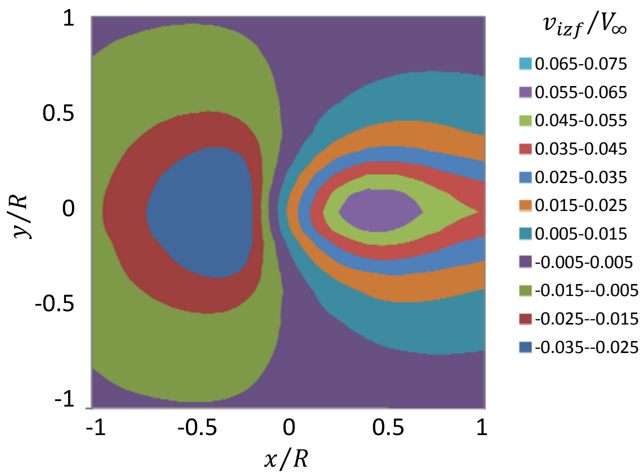

(b) RTA: CFD data (left), model (right)

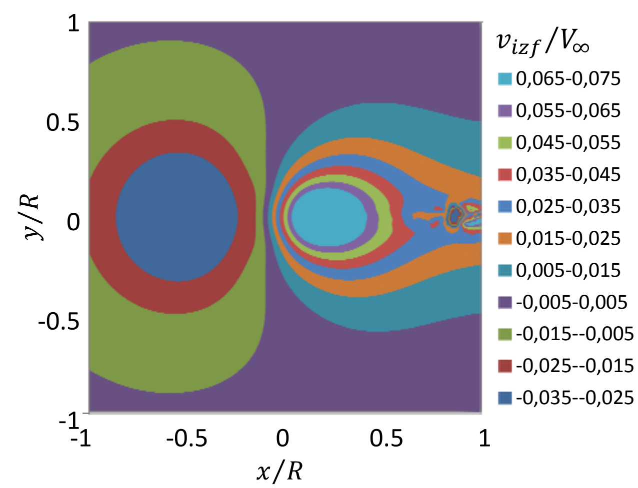

(c) HART: CFD data (left), model (right)

Figure 47: Comparison of CFD data with model reconstruction, $\alpha = +10°, z = 0.1R$.

In all the cases (figs. 45 to 47) the LRTA has slightly larger peak values than the RTA, but the HART has even larger values, clipped by the scale. In general, the overall agreement is good, the peak-to-peak data range is very close between CFD data and the model, and the peak position is well reflected. The variation from mainly upwash for negative angles of attack to similar upwash and downwash strength at $\alpha = 0°$, and to more downwash than upwash for positive angle of attack, is correctly modeled. Although the overall appearance is quite similar, individual differences show up but are reflected by the model.

5.2 Range of Large Angles of Attack (HART Only), No Side-Slip

The range of large angles of attack, $30° \leq |\alpha| \leq 90°$, is covered by CFD data of the HART fuselage only. As long as the angle of attack is negative (nose-down), the rotor operational volume above the fuselage is on the windward side, and clean flow is observed everywhere. In contrast, for positive angles of attack (nose-up) this volume of observation is in the separated flow regime of the leeward side, and strong flow separation with its turbulence shows up in the data. The model is not designed to represent these; therefore they do not show up in the reconstruction, which shows the mean steady component only.

In figure 48 the case of $\alpha = -90°$ is shown in (a), which represents a hovering case with the fuselage blown from above by the rotor downwash, or a vertical climb condition where the total velocity from above is the sum of rotor-induced downwash and the climb velocity. In figure 48 (b) $\alpha = -60°$, which represents a very steep upward climb angle, and in (c) $\alpha = -30°$, which is still a relatively steep climb condition. In figure 49 (a) $\alpha = 30°$ (steep descent), in (b) $\alpha = 60°$ (very steep descent), and in (c) $\alpha = 90°$, which is vertical descent where the fuselage is blown directly from below and the rotor is operating in the wake of it with all the turbulent flow separation of the fuselage body in the center area.

In all of these cases the CFD data are well represented by the model, including the variation from upwash with virtually no downwash at $\alpha = -90°$ to the opposite at $\alpha = +90°$. The tail boom impact on the fuselage-induced velocities is clearly visible in the central aft portion of the images for $|y|/R \leq 0.3, x/R > 0.5$. For negative angles of attack the tail boom generates upwash because of its blockage of the flow, and for positive angles of attack it generates downwash (which is the drag bucket).

The peak values of CFD data especially for $\alpha = -90°$ and $-60°$ in figure 48 (a) and (b), respectively, are not matched well by the model, but this is within the hub center area around $x/R = y/R = 0$. However, everything within the root-cutout of the blade, say, inside a circle of 20 to 25 percent radius, can be ignored anyway because no airfoil of the blade will encounter it any time. As such, the error in this area is allowed to be larger than elsewhere.

Similarly, in figure 49 significant turbulence is seen in the CFD data, which is not matched by the model by intent. Recall that the model is thought to represent a time-averaged fuselage-induced velocity field that will not have any such structures. In the remaining areas of clean and undisturbed flow the comparison of the model with CFD data again leads to good agreement, and even the peak values are matched by the model.

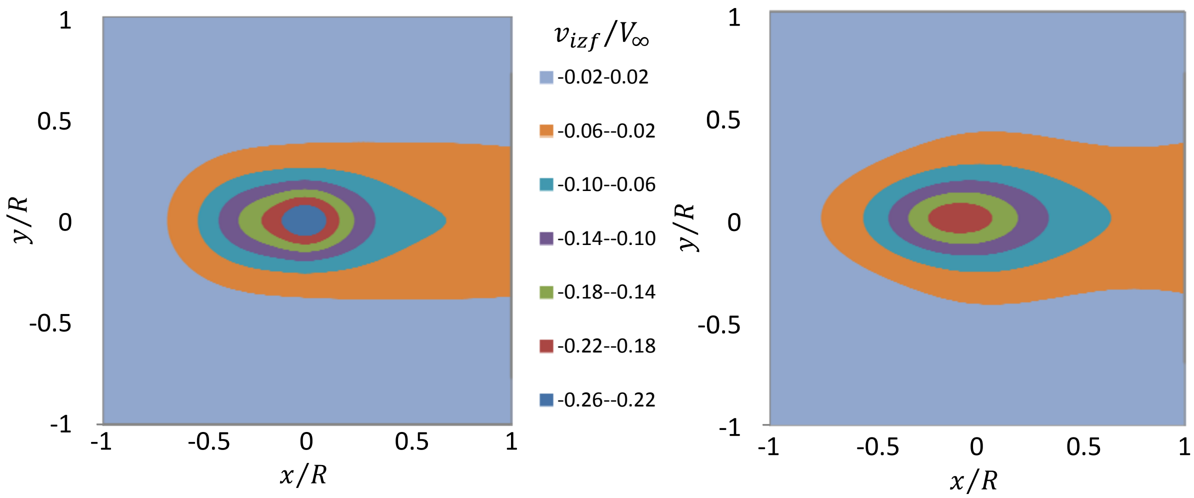

(a) $\alpha = -90°$: CFD data (left), model (right)

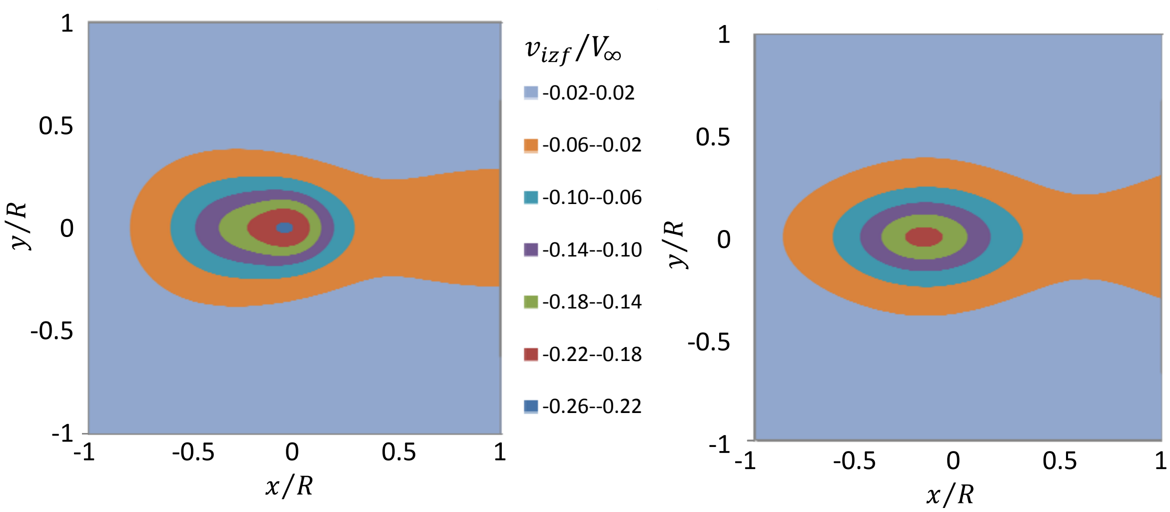

(b) $\alpha = -60°$: CFD data (left), model (right)

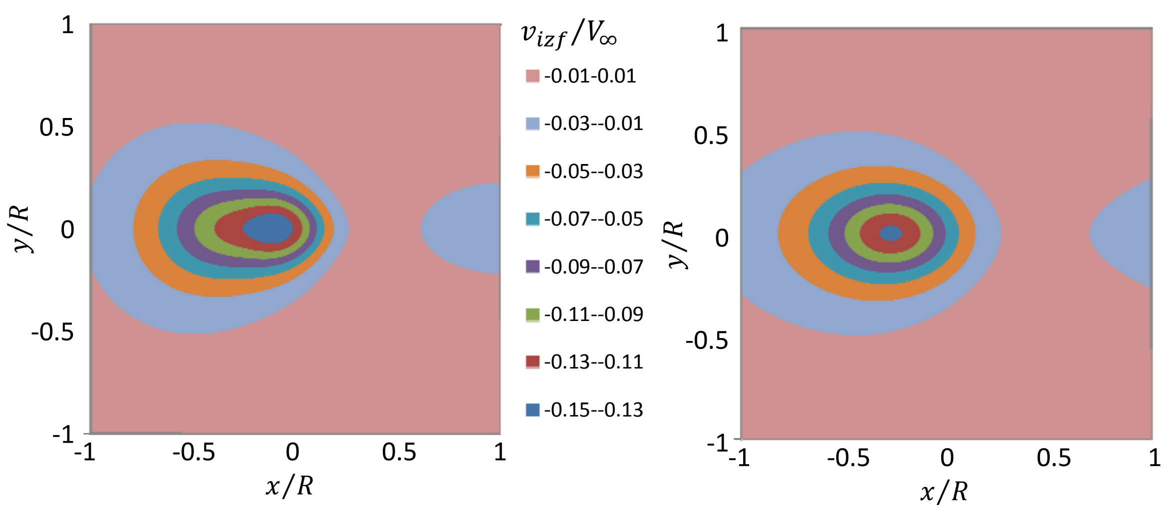

(c) $\alpha = -30°$: CFD data (left), model (right)

Figure 48: Comparison of CFD data with model reconstruction, $\alpha \leq -30°, z = 0.1R$.

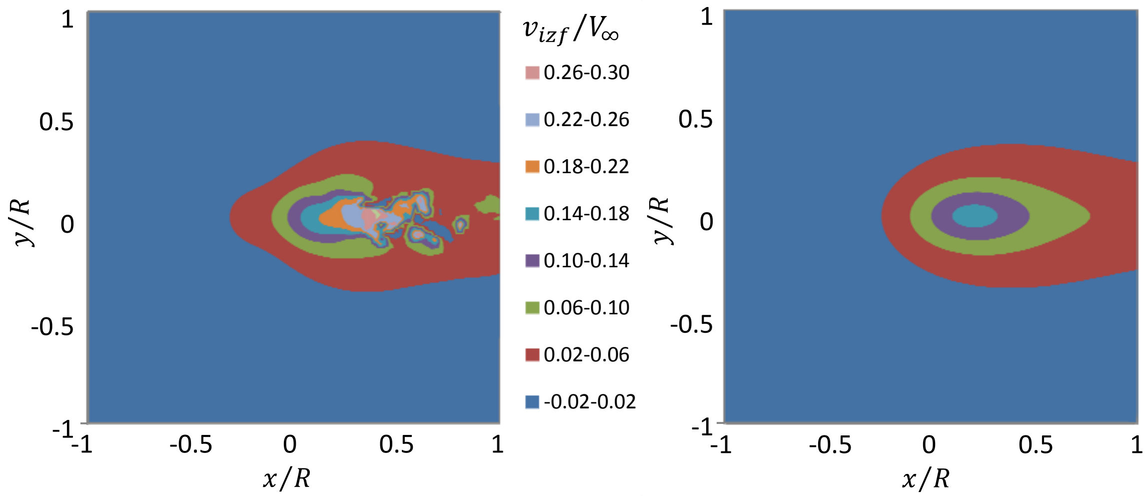

(a) $\alpha = 30°$: CFD data (left), model (right)

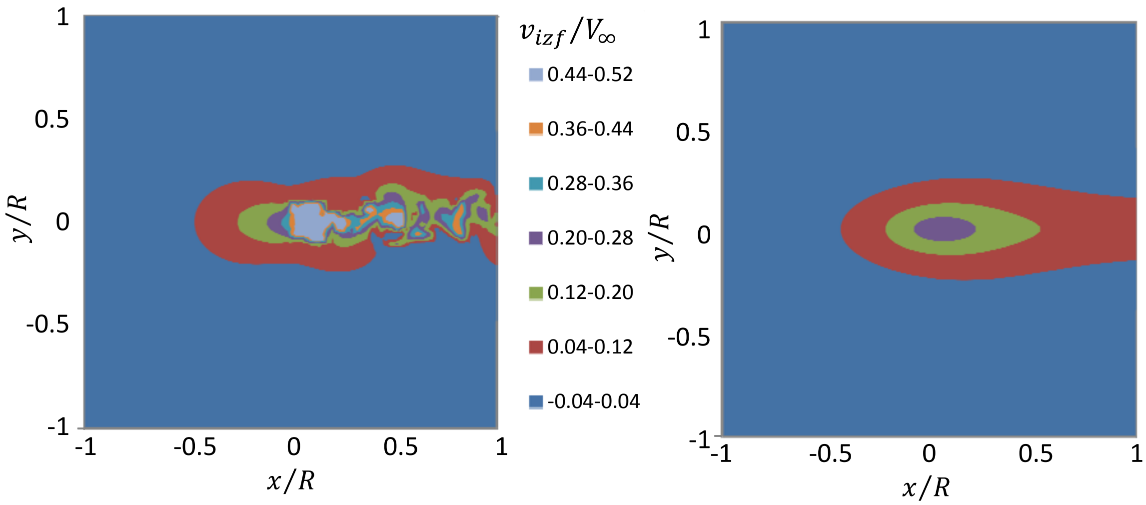

(b) $\alpha = 60°$: CFD data (left), model (right)

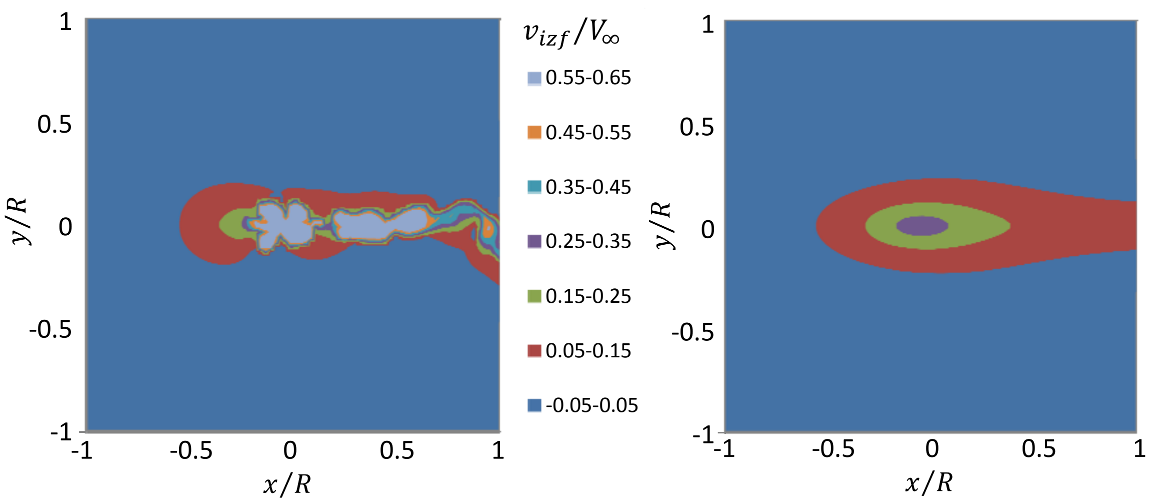

(c) $\alpha = 90°$: CFD data (left), model (right)

Figure 49: Comparison of CFD data with model reconstruction, $\alpha \geq 30°, z = 0.1R$.

5.3 Range of Large Side-Slip Angles (HART Only), No Angle of Attack

The range of large side-slip angles of $30° \leq \beta \leq 90°$ is covered by CFD data of the HART fuselage only. Negative side-slip angles were not computed because the fuselage is laterally symmetric and the results can simply be mirrored, i.e. $v_{if}(x,y,z,-\beta) = v_{if}(x,-y,z,\beta)$. Undisturbed potential theory type of flow is observed for $\beta = 10°$ everywhere and also for all β on the windward side, while on the leeward side flow separation is progressively developing with increasing side-slip angle, starting with $\beta = 30°$. The model is not designed to represent these turbulent separation features; therefore they do not show up in the reconstruction, which shows the mean steady component only. In figure 50 the case of $\beta = 10°$ is shown while figure 51 shows $\beta = 30°$ in (a), $\beta = 60°$ in (b), and $\beta = 90°$ in (c), which represents the quartering flight condition.

In all cases of side-slip the general features are well represented by the model. The maximum upwash peak on the windward side is found much closer to the fuselage centerline than the downwash peak on the leeward side, which appears at a much larger lateral distance to the fuselage. Also, the variation of the x-position of the peak is matched well. Finally, the tail boom effect shows up in an extension of the upwash on the windward side to the rear end of the graphs for $\beta \geq 30°$. The associated impact on the downwash is more visible for smaller side-slip angles, $\beta \leq 30°$, but is still present for larger ones. However, it is hidden in the larger scale range of fuselage-induced velocities at large side-slip angles.

Note that the peak values of fuselage-induced upwash and downwash increase significantly with increasing side-slip angle: the maximum upwash for $\alpha = \beta = 0°$ is about $v_{izf}/V_\infty \approx -0.07$, while for $\alpha = 0°, \beta = 90°$ the ratio grows to about -0.26, which is more than three times larger. The downwash peak is also larger in side-slip conditions than for $\alpha = \beta = 0°$, but its magnitude rises only by a factor of two.

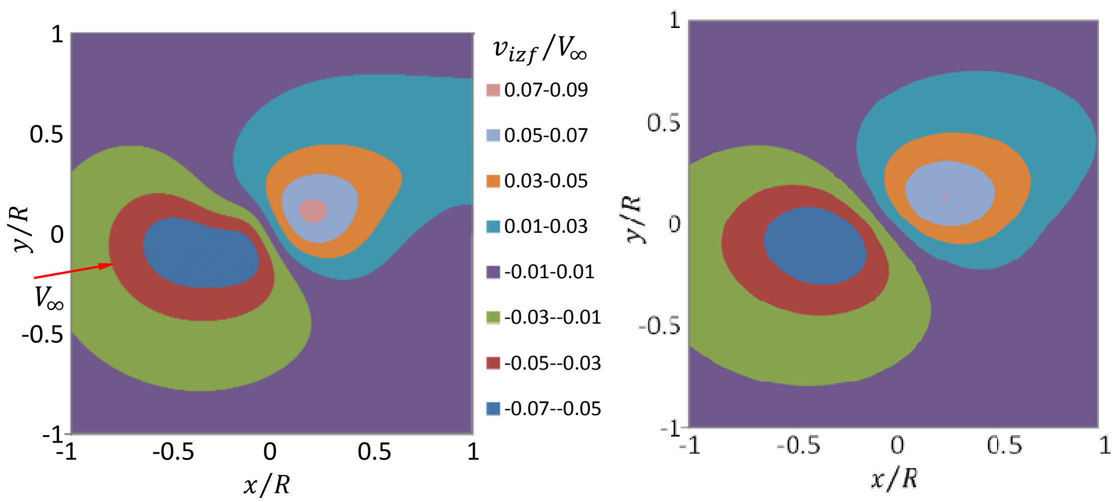

$\beta = 10°$: CFD data (left), model (right); $z/R = +0.1$

Figure 50: Comparison of CFD data with model reconstruction, $\beta = 10°$.

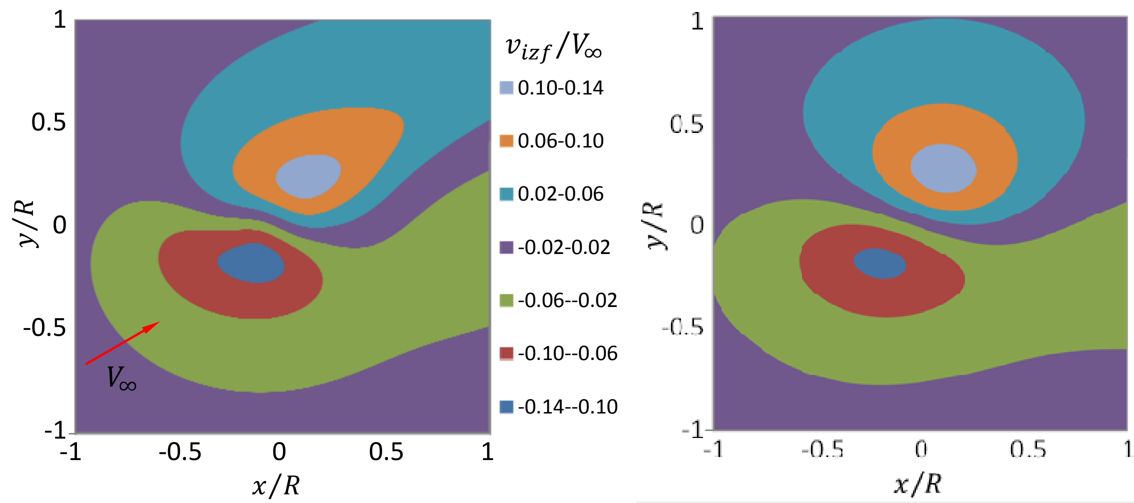

(a) $\beta = 30°$: CFD data (left), model (right); $z/R = +0.1$

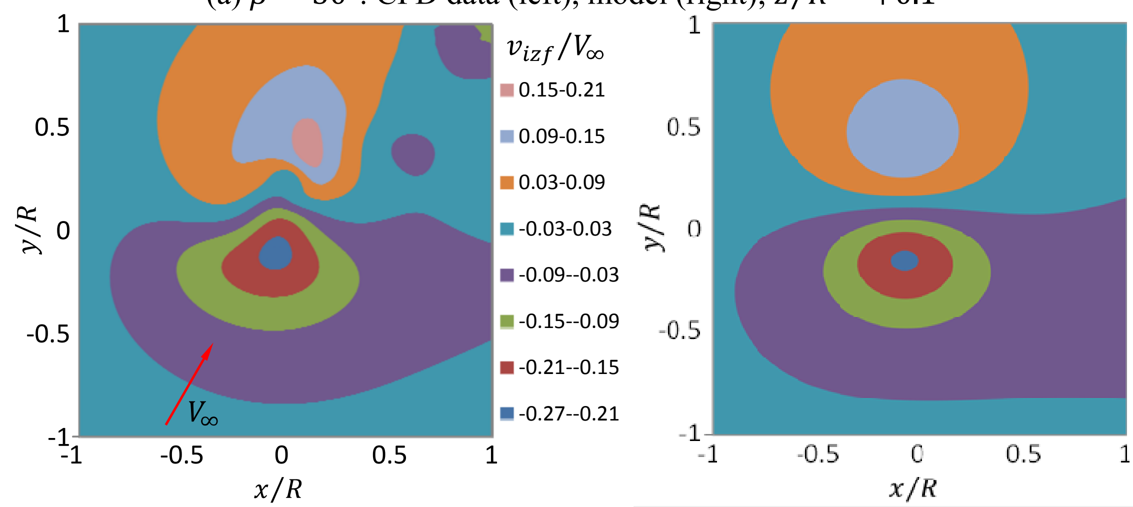

(b) $\beta = 60°$: CFD data (left), model (right); $z/R = +0.1$

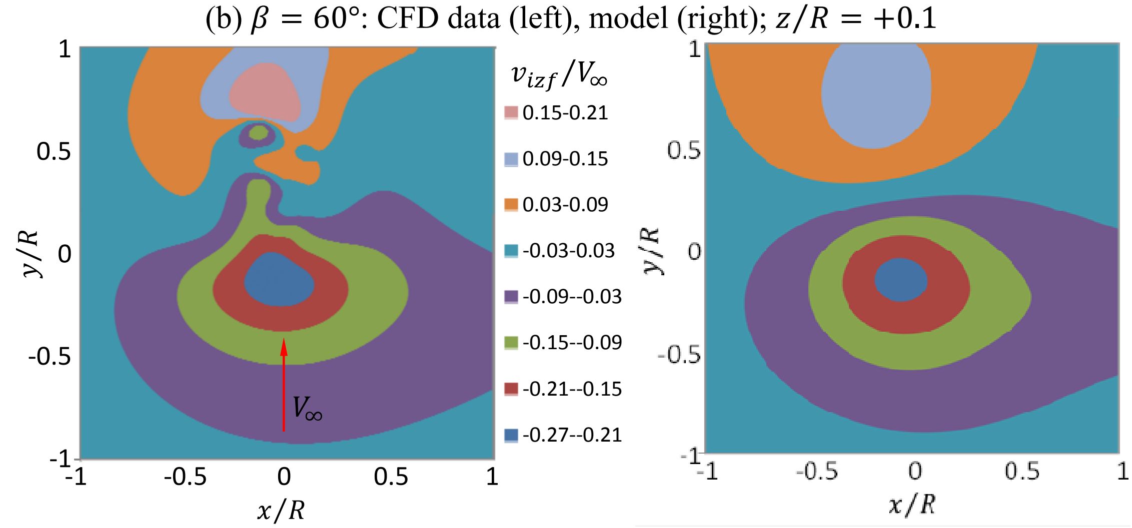

(c) $\beta = 90°$: CFD data (left), model (right); $z/R = +0.1$

Figure 51: Comparison of CFD data with model reconstruction, $\beta \geq 10°$.

6. Model Behavior Outside the Validated Data Range

It is clear by the nature of the functions used that the model will generate fuselage-induced velocities approaching zero for large distances to the fuselage in any direction. However, it may be desired to also have—at least approximately—the fuselage-induced velocity field below the body. This can be achieved by using Eq. (7), and results are given for the symmetry plane, $y/R = 0$, in figure 52 with $\alpha = \beta = 0°$ (same scale for all graphs). The planes of data extraction that form the basis of the model are indicated by the horizontal lines above the fuselage.

As can be seen, the induced velocities on the fuselage centerline are always zero and form the separation between the model used for the upper part and that of the lower part. Again, the velocities die out asymptotically for large distances to the body as required by potential theory. The definition of a body centerline leaves some room for interpretation. For the LRTA and HART it is relatively simple because the body is roughly symmetric in z-direction, but the RTA

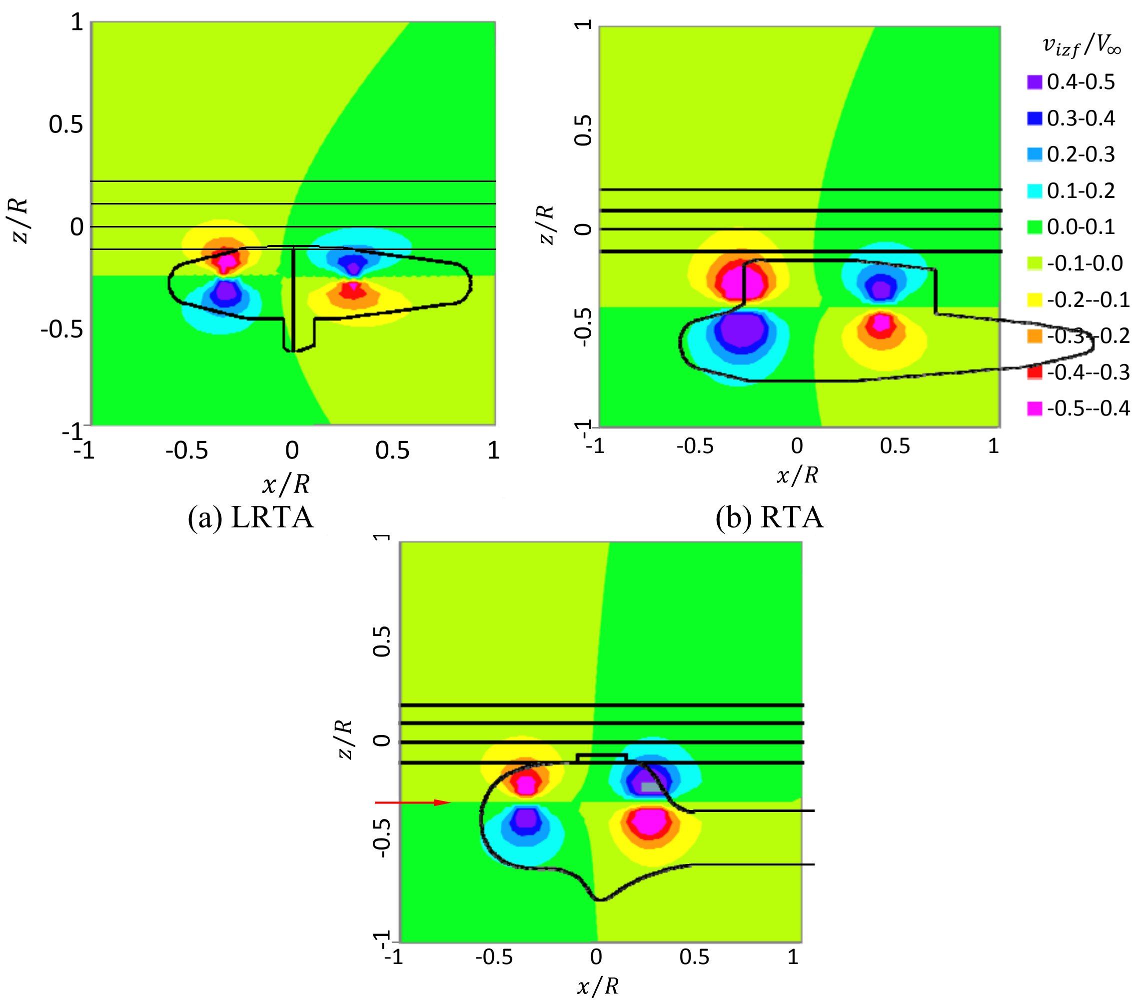

(a) LRTA (b) RTA

(c) HART

Red arrow indicates direction of V_∞, $y/R = 0$.

Figure 52: Usage of the model outside the validated range, $\alpha = \beta = 0°$.

is more difficult; it may be separated into two bodies—one being the long cigar-shaped lower part, the other being the upper fairing.

It must clearly be understood that in the current version of the model the fuselage-induced velocity field below the body centerline is just a mirror image following Eq. (7) and based on the model of the flow above the fuselage: $v_{izf}(\alpha, z < z_0) = -v_{izf}(-\alpha, z > z_0)$. It does not care about any different shapes of the lower side of the fuselage and therefore cannot represent them. However, it leads to physical meaningful flow fields in as much as there is upwash where upwash is expected and the same for the downwash. An example for a positive and a negative angle of attack is given in figure 53 for the LRTA and RTA fuselages. The variation of upwash and downwash intensities and positions can clearly be seen.

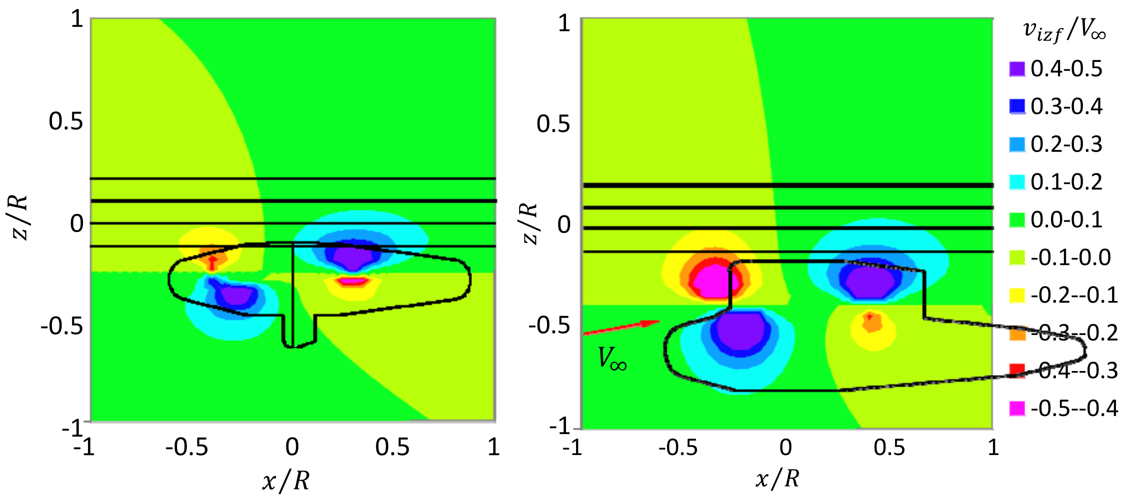

(a) $\alpha = +10°$, LRTA (left), RTA (right)

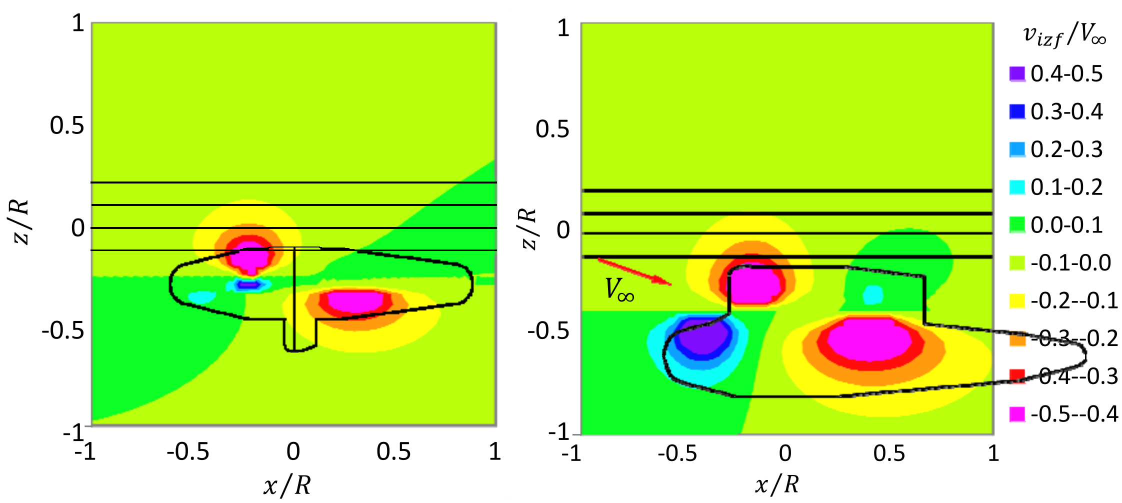

(b) $\alpha = -20°$, LRTA (left), RTA (right)

Red arrow indicates direction of V_∞, $y/R = 0$.

Figure 53: Usage of the model outside the validated range, $\alpha \neq 0°, \beta = 0°$.

Large angles of attack and any side-slip angles were only available for the HART fuselage. Results obtained by the model for the entire range from vertically upward flow to vertically downward flow are shown in figure 54. Comparing figure 54 (a) with (d), or (b) with (c), the mirroring concept is clearly visible. When the fuselage is blown from above in (a), the upwash upon the fuselage represents the blockage of the flow and the upwash below the fuselage represents the wake in the flow. The opposite is seen when the fuselage is blown from below in (d) and there is downwash everywhere; below the fuselage represents the flow blockage and above the fuselage represents the wake. The more moderate angles of attack of $\alpha = -30°$ in (b) and $\alpha = +30°$ in (c) show a mixture with elements from both $\alpha = 0°$ and the extremes in (a) and (d).

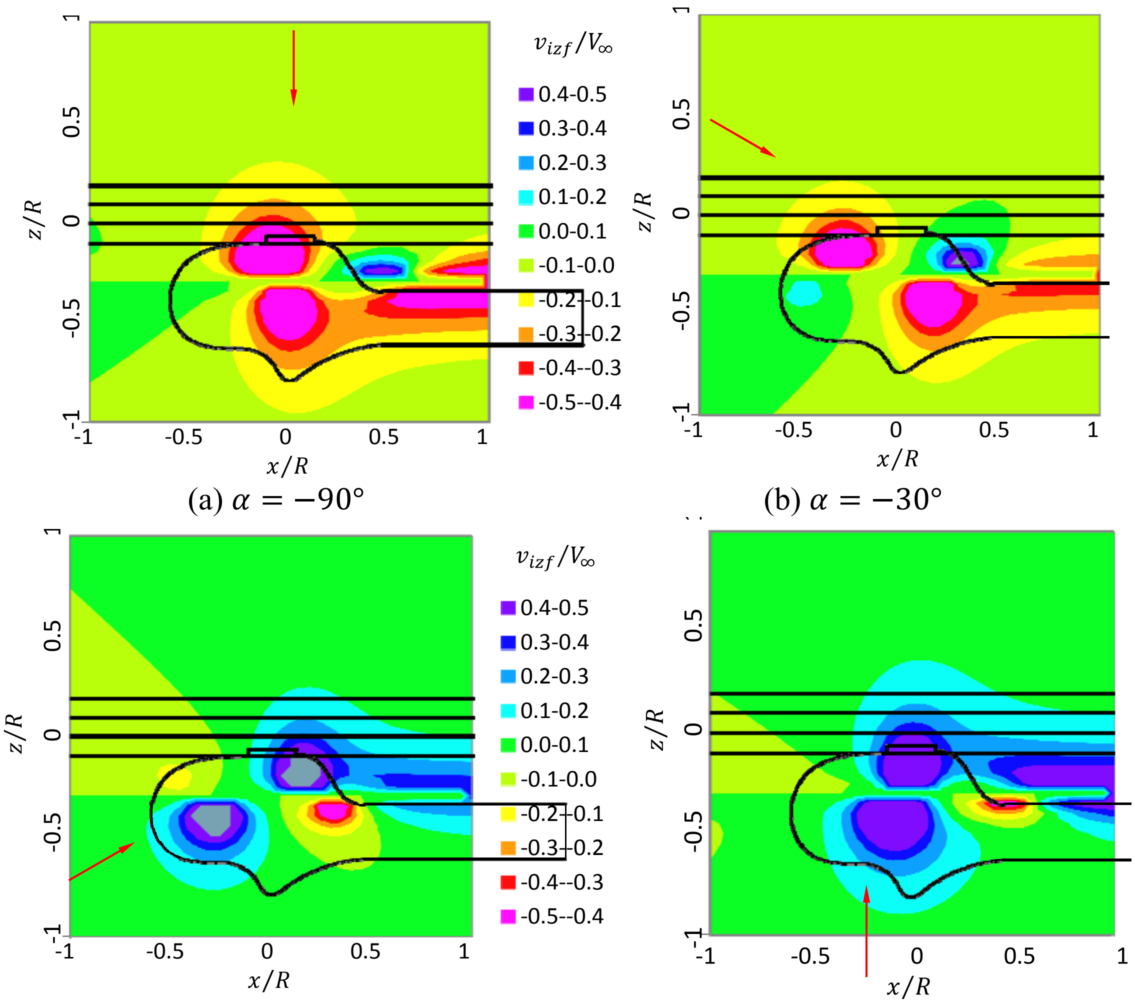

(a) $\alpha = -90°$ (b) $\alpha = -30°$

(c) $\alpha = +30°$ (d) $\alpha = +90°$

Red arrow indicates direction of $V_\infty, y/R = 0$.

Figure 54: Usage of the HART model outside the validated range, $\alpha \neq 0°, \beta = 0°$.

Finally the side-slip results for zero angle of attack are shown in figure 55. It was shown in figure 50 and figure 51 that the peak fuselage-induced upwash velocities on the windward side are closer to the body than the downwash on the leeward side. This is more clearly seen in the velocity distributions in a plane, $x = x_u$ (i.e., a cut through the upwash maximum). Results are shown for both quartering flight directions with the flow coming from the right in figure 55 (a) and from the left in figure 55 (b). Both effects observed previously in figure 50 and figure 51 are more clearly seen now, as there is the position of the fuselage-induced velocity peaks relative to the fuselage center and the intensity of windward side velocities being larger than those of the leeward side.

There is always a pair of upwash and downwash above each other. On the windward side potential flow-like behavior is present: the flow has to go upwards at the upper part of the fuselage in order to go around it, and at the lower end of the fuselage it has to go downwards for the same reason. At the centerline there is no upwash or downwash because this is the streamline of the stagnation point. On the leeward side the opposite is observed, but the wake of the fuselage extends farther away from it and the largest fuselage-induced velocities are more than half a radius away from it. This is due to RANS computation with flow separation. In the case of a full potential method like panel code the flow would be attached everywhere, and the leeward side effects would be a mirror image of the windward side, both with respect to geometry and to intensity.

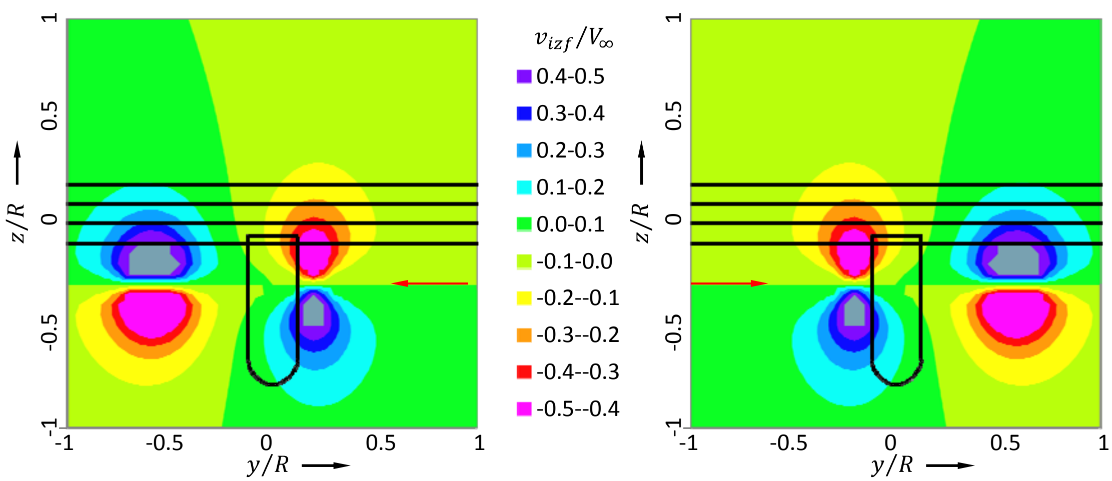

(a) $\beta = -90°$, wind from right (b) $\beta = 90°$, wind from left

View from back, $\alpha = 0°, x = x_u$.

Figure 55: Usage of the HART model in quartering flight.

7. Effect of Fuselage-Rotor Interference on Rotor Trim

7.1 Results From Simple Blade Element Theory

Analytic results can be obtained from simple blade element theory [50] assuming constant inflow, linear steady incompressible 2D aerodynamics, no flapping motion, centrally hinged blades trimmed for zero hub moments and a given thrust coefficient of $C_T = C_W = 0.00484$, and the rotor solidity assumed as $\sigma = 0.07$. Results of a UH-60 size rotor on the LRTA and a Bo105 full-scale size rotor on the RTA are compared with those of a Bo105 model-size rotor on the HART fuselage. For simplicity the fuselage-induced velocities are always taken from a plane, $z/R = 0.05$, which is 5 percent radius above the hub center, and can be interpreted as velocity data taken from the tip path plane with a coning of 2.8° and no forward or lateral tilt of the rotor disk. The results allow a direct comparison of effects on cyclic trim controls when comparing the isolated rotor trim with the one obtained including the fuselage, or the change of thrust when trimming the isolated rotor, keeping the collective fixed and then introducing the fuselage.

The procedure is as follows: first, the fuselage-induced velocity data are computed in polar coordinates for constant radii from 0.3 to 1, in increments of 0.1, and in increments of 10° azimuth for the entire revolution of the rotor blade. Second, for every radial position a Fourier analysis of the fuselage-induced velocity time history is performed, providing the mean steady part and the first two harmonics. Third, these Fourier coefficients are then approximated as a polynomial of third order in radial direction. In this polar coordinate form analytical results can directly be given for (a) trim controls required to keep rotor moments the same as for the isolated rotor when including the fuselage, and (b) change of rotor thrust when keeping collective fixed from the isolated rotor trim and only re-trimming the hub moments by cyclic controls.

These results characterize the main effects of the fuselage presence on the rotor blade aerodynamics and related trim controls. For details of the procedure and formulae see reference [50]. In any case of pure angle of attack without side-slip there will be lateral symmetry of the fuselage-induced flow field such that the Fourier coefficients will contain only cosine terms. Only in side-slip conditions with lateral asymmetry will both cosine and sine terms be present. Considering pure α variations, the fuselage-induced inflow referenced to the tip speed can be written as

$$\lambda_{izf}(r,\psi) = \frac{v_{izf}(r,\psi)}{V_\infty} = \sum_{n=0}^{\infty} \lambda_{izfn}(r)\cos(n\psi); \qquad \lambda_{izfn}(r) = \sum_{j=0}^{J} c_{nj} r^j \tag{9}$$

wherein $J = 3$ appears sufficient for most of the radial distributions. Using blade element velocities to compute the local dynamic pressure (simplified as $V_T^2\,\rho/2$) and the blade element angle of attack, α_a

$$\begin{aligned} &V_T = \Omega R(r + \mu \sin\psi) \qquad V_P = \Omega R \mu \lambda_{izf}(r,\psi) \\ &\alpha_a = \Theta - \arctan(V_P / V_T) \approx \Theta_C \cos\psi + \Theta_S \sin\psi - V_P / V_T \end{aligned} \tag{10}$$

an expression for the thrust increase or decrease due to the fuselage-induced inflow can be derived (A and B are the effective nondimensional radii of the beginning and the end of the airfoiled section of the blade; the approximation makes use of $A = 0, B = 1$).

$$\frac{\Delta C_T}{C_W}=\frac{1}{2\pi}\int_0^{2\pi}\int_A^B\frac{dC_T}{C_W}d\psi=\mu\frac{\sigma\pi}{C_W}\left(\Delta\Theta_S\frac{B^2-A^2}{2}-\sum_{j=0}^{J}c_{0j}\frac{B^{j+2}-A^{j+2}}{j+2}\right)$$
$$\approx\mu\frac{\sigma\pi}{C_W}\left(\frac{\Delta\Theta_S}{2}-\sum_{j=0}^{J}\frac{c_{0j}}{j+2}\right) \tag{11}$$

The cyclic controls required to keep hub moments the same as for the isolated rotor results (the approximation on the right is obtained using $A=0, B=1$) are:

$$\Delta\Theta_C=\mu\frac{\sum_{j=0}^{J}c_{1j}\frac{B^{j+3}-A^{j+3}}{j+3}}{\frac{B^4-A^4}{4}+\mu^2\frac{B^2-A^2}{8}}\approx\frac{8\mu}{2+\mu^2}\sum_{j=0}^{J}\frac{c_{1j}}{j+3}$$
$$\Delta\Theta_S=\mu^2\frac{\sum_{j=0}^{J}\left(c_{0j}-\frac{c_{2j}}{2}\right)\frac{B^{j+2}-A^{j+2}}{j+2}}{\frac{B^4-A^4}{4}+3\mu^2\frac{B^2-A^2}{8}}\approx\frac{4\mu^2}{2+3\mu^2}\sum_{j=0}^{J}\frac{2c_{0j}-c_{2j}}{j+2} \tag{12}$$

As can be seen, the thrust change is dependent on the mean part of the fuselage-induced inflow (c_{0j} with 0 indicating the 0/rev or steady part) and on the change of longitudinal cyclic, $\Delta\Theta_S$, which in reverse is dependent on both the mean and the 2/rev part of the induced inflow. The lateral cyclic depends on the 1/rev part of the fuselage-induced inflow—expected to be dominant at least for small angles of attack—where a large upwash is present in the front and a large downwash is present in the rear of the rotor disk, which represents the 1/rev cosine component exactly.

7.1.1 Effect on Thrust

The difference in thrust with an LRTA body on a UH-60 size rotor, an RTA body on a Bo105 full-scale size rotor, and a HART body on a Bo105 model-scale size rotor—when collective is kept fixed from the isolated rotor trim and cyclic controls are set to keep moments at zero—is shown in figure 56. For this moderate range of angles of attack (though they cover most of the usual flight conditions) the thrust varies between an increase of 6 percent (LRTA, HART) or 10 percent (RTA) for $\alpha=-20°$, where the fuselage upwash is dominant, to a thrust loss of 4 percent for all rotor/fuselage combinations for $\alpha=+10°$, where the fuselage downwash is dominant. When $\alpha=0°$ the upwash and downwash are about balanced; only slight differences are seen depending on the individual fuselage characteristics caused by their shape.

Negative α: Any fuselage blocks the flow to a more or less extent (depending on the fuselage shape and position relative to the rotor upon it) and generates mainly an upwash in the rotor similar to ground effect (but significantly less being mainly confined to the centerline, and to some smaller extent, right and left of it), which effectively increases thrust. The upwash is proportional to the flight speed, as is the thrust increase. The maximum for the full-scale Bo105 rotor/RTA configuration is 10 percent of the weight coefficient, as given previously at an advance ratio of $\mu=0.5$ and $\alpha=-20°$, while only 5 percent for both the UH-60 size rotor on the LRTA and the model rotor on HART. Within the LRTA/RTA angles of attack, the relative impact of the fuselage on rotor thrust is larger for the RTA configuration than for the HART and the LRTA.

$\alpha = 0°$: The upwash in the front and the downwash in the rear are about the same size and total intensity for the LRTA, and practically no influence on thrust is found. For the RTA, and even more so for the HART, there is still more upwash than downwash at this angle of attack. Thus, the effect on thrust is only a small increase of about 2 percent in both cases.

Positive α: The fuselage blocks the flow, so now the rotor is on the leeward side and experiences mainly a downwash with the highest intensity downstream of the hub. The thrust is therefore reducing with a minimum of –4 percent loss for all rotor/fuselage combinations at an advance ratio of $\mu = 0.5$.

As indicated by Eq. (11), for small to moderate advance ratios the thrust change is linear in μ and only for larger advance ratios becomes slightly nonlinear. Also, the nonlinear impact of the longitudinal cyclic, $\Delta\Theta_S$, is smaller than that of the downwash and may even be neglected because this cyclic control variation is small by itself (as seen later in figure 58).

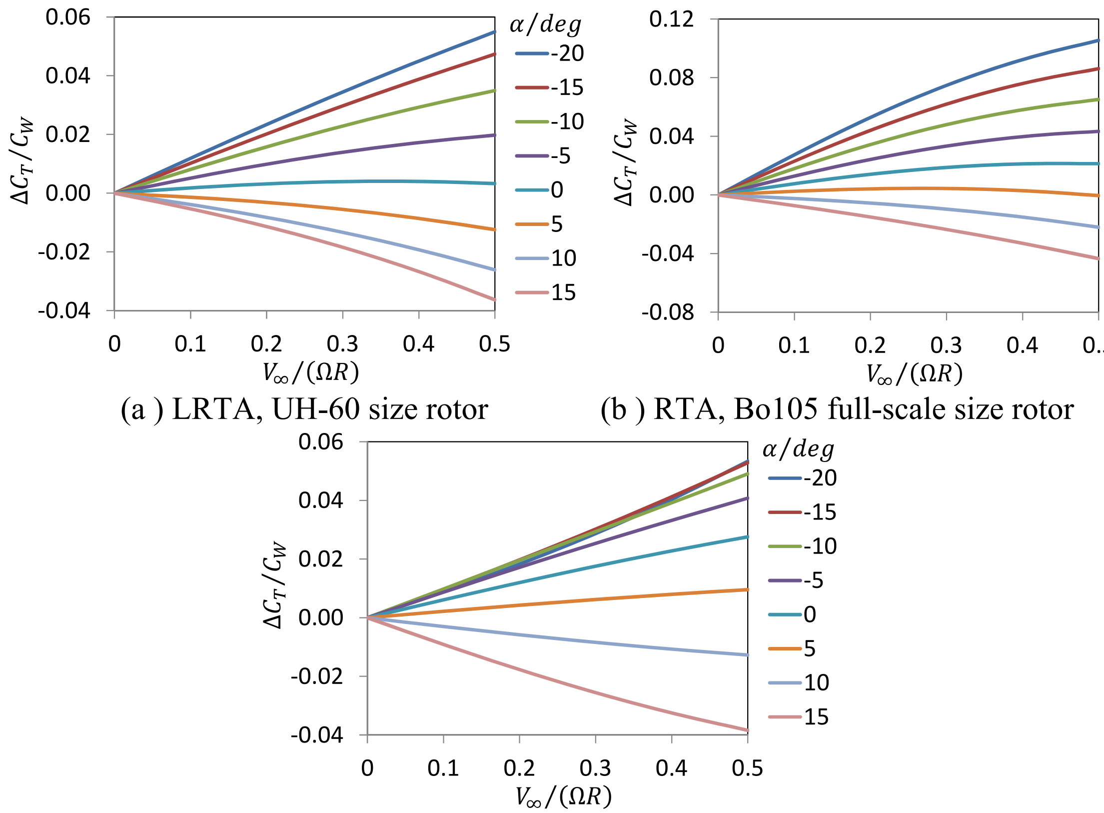

(a) LRTA, UH-60 size rotor

(b) RTA, Bo105 full-scale size rotor

(c) HART, Bo105 model-scale size rotor

Figure 56: Relative thrust change due to fuselage presence.

7.1.2 Effect on Lateral Control

The main upwash/downwash areas appear on the centerline of the fuselages with lateral symmetry, therefore the lateral control, $\Delta\Theta_C$, is affected most. For the range of angles of attack shown here, there always is a strong longitudinal gradient of fuselage-induced flow (i.e., for negative α there is a strong upwash in the front and little downwash in the rear, for $\alpha = 0°$ the upwash in the front and the downwash in the rear are almost the same strength, and for positive α there is a smaller upwash in the front and a stronger downwash in the rear). This affects the blade element angle of attack mainly around azimuths of $\psi = 0°$ and 180°, and the lateral control angle as shown in figure 57. Again, the fuselage-induced flow is proportional to flight speed and the impact on lateral control as well (see Eq. (12)).

For negative α the maximum impact is therefore found at $\mu = 0.5$ with $\Delta\Theta_C$ ranging from 0.5° (LRTA and RTA) to 0.8° for the HART fuselage. With increasing angle of attack the upwash-downwash velocity range increases as well and the impact on $\Delta\Theta_C$ with it; it ranges from 0.9° (LRTA) to 1.2° (RTA, HART). This reflects the varying amount of relative difference in fuselage-induced velocities before and aft of the hub center. Compared to the lengthy cigar-like LRTA or the similar RTA (but with the tower on it), the HART body is more compact and bluff with larger local curvature, generating stronger upwash and downwash fields. For larger positive angles of attack of HART up to +90° (equivalent to vertical descent with the rotor in the separated wake of the fuselage), the downwash dominates both the front and rear above the

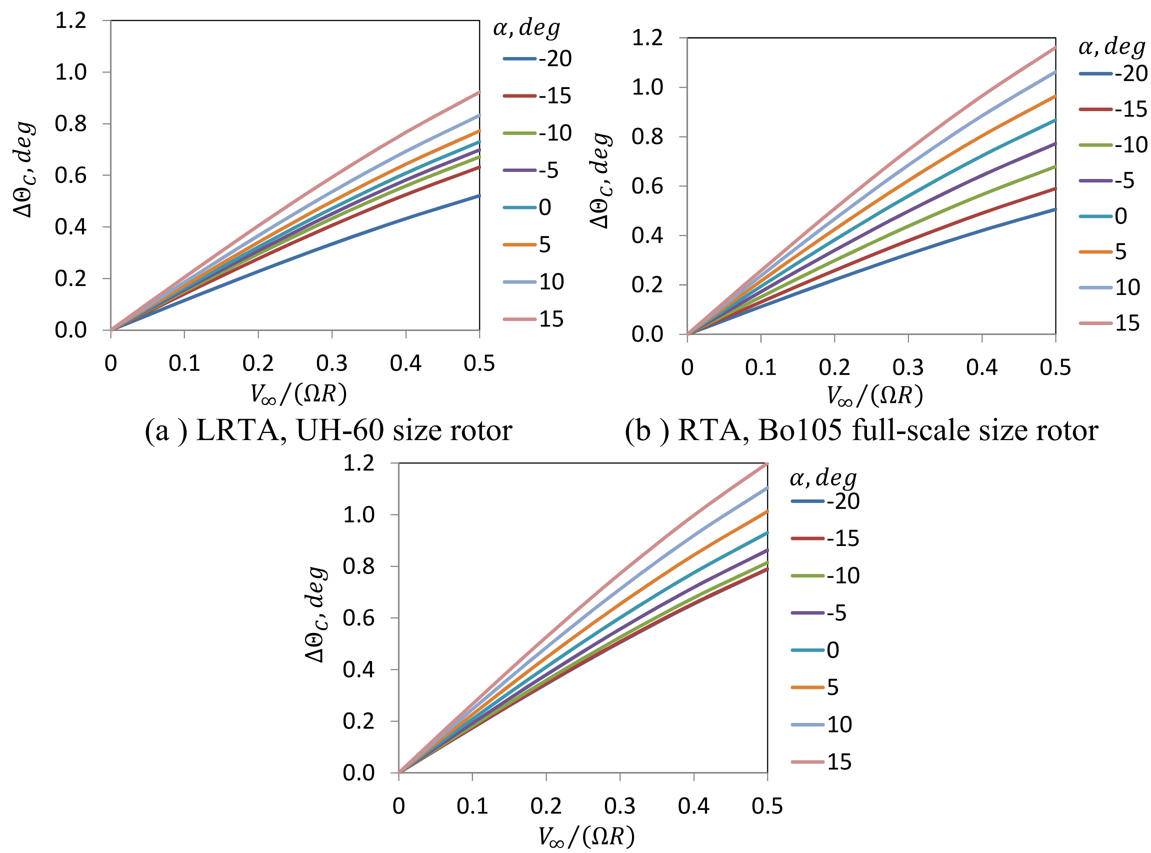

(a) LRTA, UH-60 size rotor (b) RTA, Bo105 full-scale size rotor

(c) HART, Bo105 model-scale size rotor

Figure 57: Change in lateral cyclic control due to fuselage presence.

fuselage, reducing the differences and the need to compensate by cyclic control. Similar behavior can be found for vertical climb ($-90°$, now with the rotor operated on the windward side in a clean, potential-flow-like environment), but there is some stronger difference in the fore-aft distribution of upwash remains and consequently the lateral control is not diminishing as much towards zero (not shown here). The reason is that the fuselage is not symmetrical with respect to a plane of $x/R = 0$; it ends in the front but towards the rear the tail boom is still blocking the flow.

7.1.3 Effect on Longitudinal Control

The longitudinal control angle, $\Delta\,\Theta_S$, is affected mainly by modifications in angle of attack at $\psi = 90°$ and $270°$ rotor blade azimuth positions. Because the flow is coming from the front and the fuselage is symmetrical to the right and left, its induced flow is also symmetrical right and left. The major difference for blade element aerodynamics is that the dynamic pressure is larger on the advancing side than on the retreating side, so the effective angle-of-attack change on the advancing side is less than on the retreating side, but the difference in dynamic pressure increases with advance ratio and is emphasized on the advancing side. However, the overall impact on the longitudinal angle in order to maintain zero hub moments as shown in figure 58 is very small compared to the lateral cyclic control.

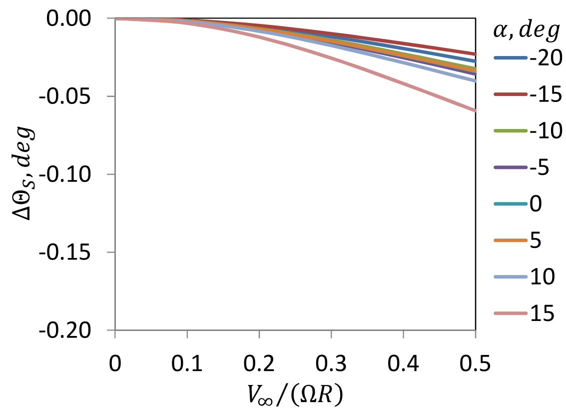

(a) LRTA, UH-60 size rotor

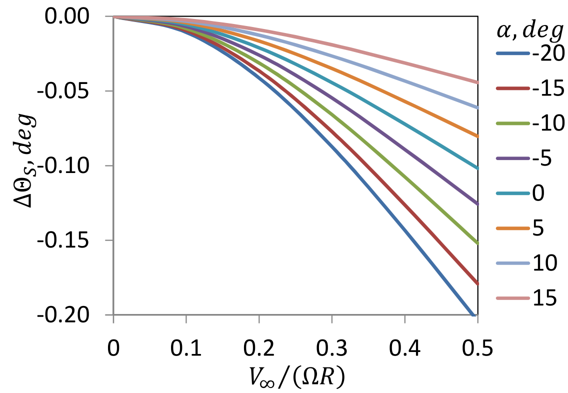

(b) RTA, Bo105 full-scale size rotor

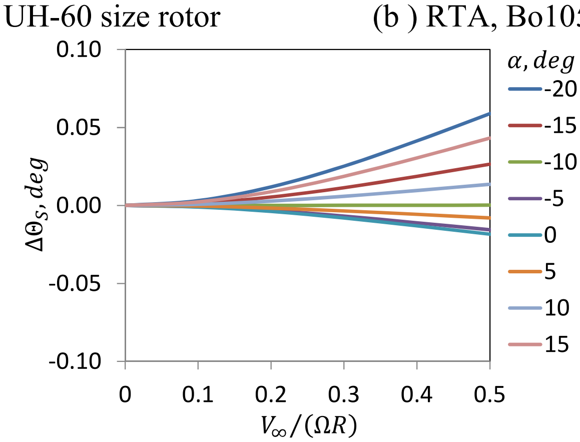

(c) HART, Bo105 model-scale size rotor

Figure 58: Change in longitudinal cyclic control due to fuselage presence.

The LRTA and RTA are quite similar in their results and show a dependency on the advance ratio that is essentially quadratic in μ as indicated by Eq. (12) with largest values obtained at $\mu = 0.5$. However, the LRTA fuselage indicates the change in longitudinal control is $0.05°$ maximum, while the RTA reaches $0.2°$, interestingly, with opposite trend; for the LRTA the control increases with increasing α, but for the RTA it is opposite. In the case of HART, the most negative values of $\Delta\Theta_S$ are obtained for $\alpha = 0°$, and for any deviation from it the longitudinal control always becomes positive up to $0.06°$. This behavior is caused by the mixture of 0/rev and 2/rev fuselage-induced downwash contributions as seen in Eq. (12) and the dependence of both on the angle of attack. However, the overall impact of the fuselage on the longitudinal control is small compared to the lateral control.

7.2 Results From Nonlinear Rotor Simulation

7.2.1 Bo105 Model Rotor With Bo105 Fuselage in Descent

In any case, such effects need to be verified by either experiment or fully nonlinear simulation. One such validation was performed recently using the Bo105 wind tunnel model as reference on a scaled Bo105 fuselage including the tail boom and empennage.[51] The operating condition was a 6° descent case at an advance ratio of $\mu = 0.151$ with strong blade-vortex interaction noise. The panel code aerodynamics were coupled to a comprehensive rotor code, HOST from Airbus Helicopters, Inc., that performed the trim of the rotor and solved for the blade elastic motion.[52] In a first run the isolated rotor was run using an incompressible unsteady panel model in combination with a free wake (denoted as “No FUS” in figures 59 to 61). A second run included the panelized fuselage below the rotor, incorporating the fuselage-induced flow field on the rotor blade elements, but also on all of the free-wake vortex lattices (denoted as “FUS”). The third run replaced the fuselage by the simple analytical model of the Bo105 fuselage-induced velocities (component normal to the rotor disk only and denoted as “FUSForm”).

Results are shown in figure 59 for the elastic blade motion. Compared to the isolated rotor, the inclusion of the fuselage does not significantly change the elastic blade motion in torsion or flapping. Replacing the panelized fuselage by the simple analytical model generates the same results almost line on line with the panelized fuselage.

A more detailed view is shown in figure 60 for the example of blade section airloads at 87 percent radius, including test data. Again, the results obtained with the panelized fuselage and with the simple analytical fuselage-induced velocity model are almost line on line, indicating that the model does represent the fuselage flow field accurately in this case. This is also visible in the acoustic pressure time histories shown in figure 61, which—especially on the advancing side—appear to be sensitive to the presence of a fuselage. The microphone data on the advancing side indicate a difference between the isolated rotor wake geometry, including the panelized fuselage. These differences are also present when replacing the panelized fuselage by the analytical model.

The advantage of using the analytical model versus the fully panelized fuselage was that CPU time could be reduced by about 30 percent, which represents the share of the fuselage panel code in the overall panel method plus free-wake CPU effort.

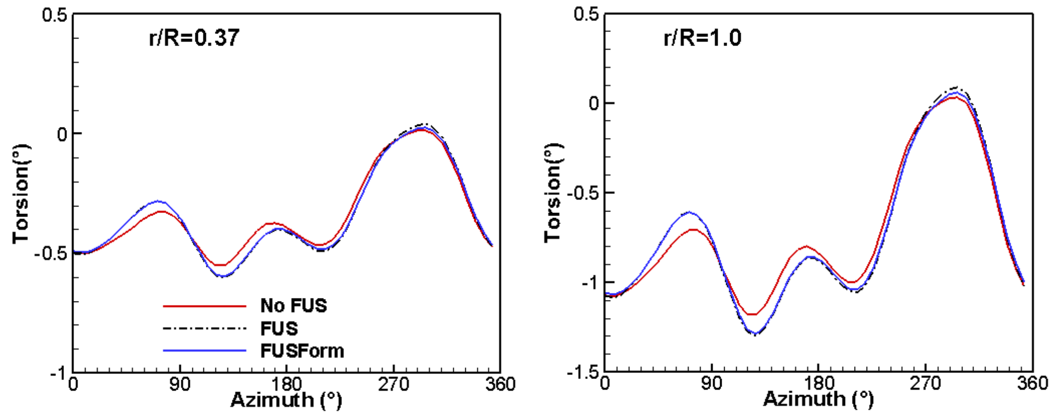

(a) Blade elastic motion relative to pilot control and pre-twist, from reference [51].

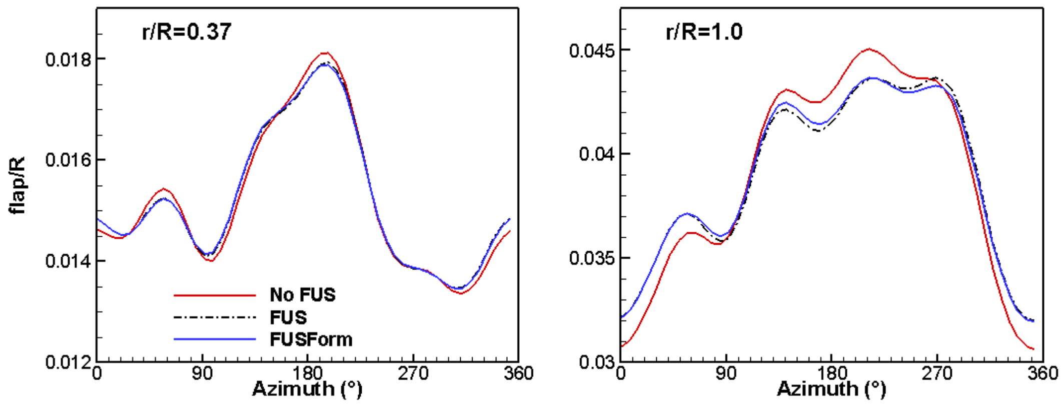

(b) Blade elastic flapping motion (including precone)

Figure 59: Comparison of blade motion for different fuselage modeling, from reference [51].

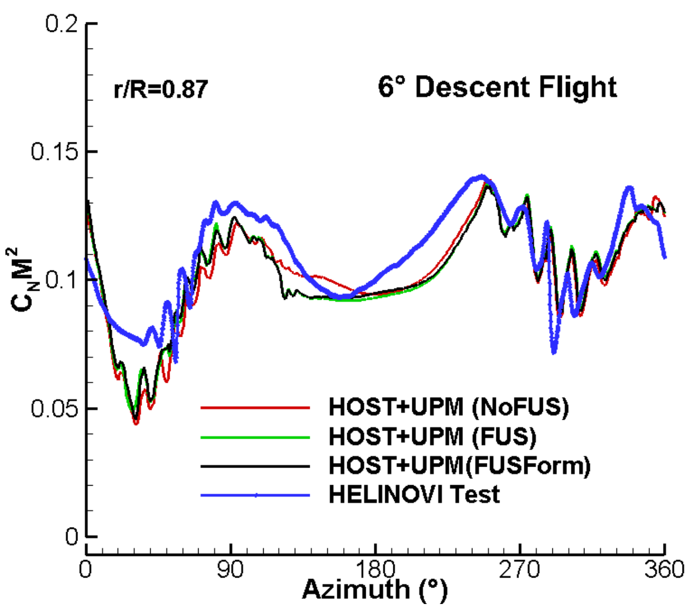

Figure 60: Normal force coefficient at 87 percent radius, from reference [51].

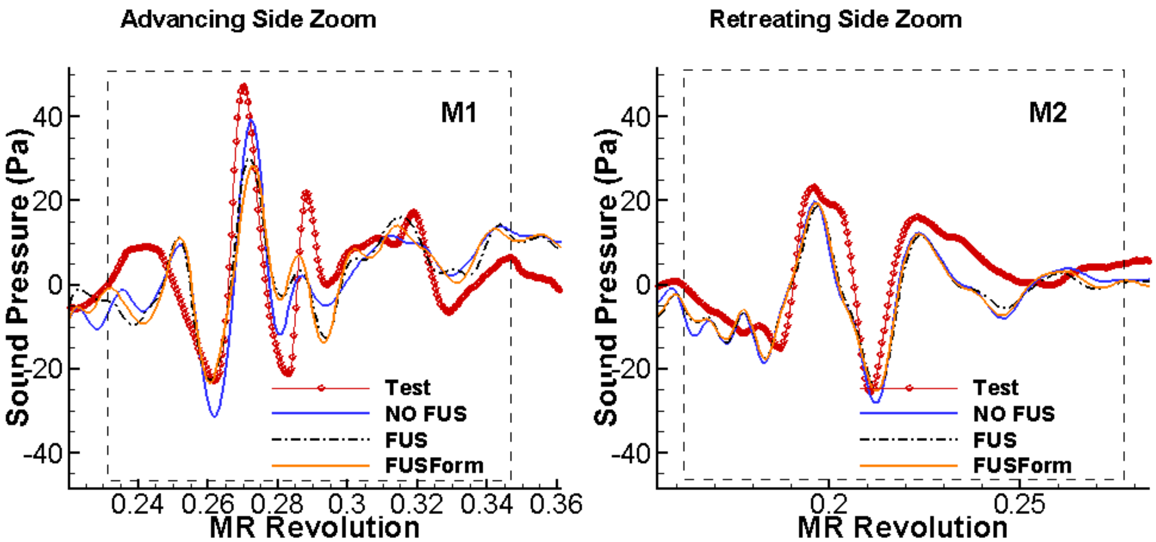

Figure 61: Acoustic pressure time histories, from reference [51].

7.2.2 LRTA, RTA, and HART: Fuselage Effect When Re-Trimming the Rotor

DLR's rotor simulation program S4[53],[54] was used with the Mangler–Squire downwash model[55] and nonlinear unsteady aerodynamics,[56] only using the first flapping mode as blade degree of freedom in order to have best possible comparability to the analytic results shown previously. Trim is performed for prescribed shaft angle of attack, flight speed, thrust coefficient, and zero hub moments. A first run comprises the isolated rotor without the fuselage; the second run includes the fuselage model, and the difference in trim allows for comparison with the previous simplified analysis. The Bo105 hingeless rotor system has a strong transmission of blade flapping moments at the root and a blade response phase much less than 90°, while the prior simple analysis assumed rigid blades with a central hinge and a flapping response phase of 90°. It is expected that this will mainly modify the longitudinal control angle results.

First, for simplicity, a re-trim to the isolated rotor thrust and moments is done using collective and cyclic controls. In this case, the change in collective should be proportional to the change of thrust shown before. Second, for some cases the collective of the isolated trim are also kept fixed and only cyclic controls are used to re-trim the moments, allowing a direct comparison with analytic results especially with respect to the change in thrust due to the fuselage presence. Because this procedure is performed manually using S4, it is more time consuming and done only for a few points for cross-checking. Additionally, the results are compared to those obtained with the Bo105 full-scale rotor on the RTA.

a. Fuselage effect on collective control

In general the trend is the same for both rotor-fuselage combinations (see fig. 62). Negative α increases the thrust as shown before and the trim requires less collective control, $\Delta\Theta_0 < 0°$, in order to keep the thrust constant; positive α acts the opposite way. The different shapes of the fuselages result in different collective required for re-trim, especially for positive angles of attack. An advance ratio of zero (hover) is not included, because this represents a fuselage angle of attack of $\alpha = -90°$ (rotor downwash from above) and no fuselage-induced data are available for such a condition for both LRTA and RTA. However, physical consideration predicts a

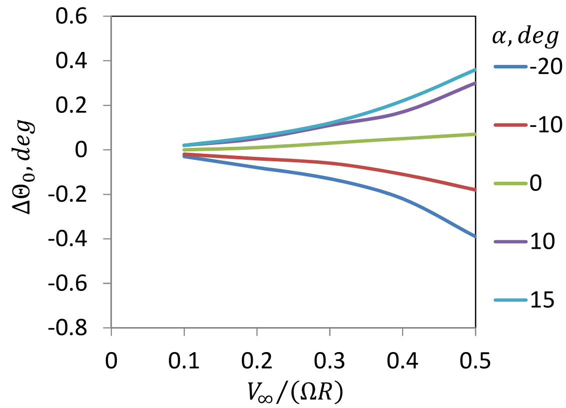

(a) Bo105 rotor on down-scaled LRTA

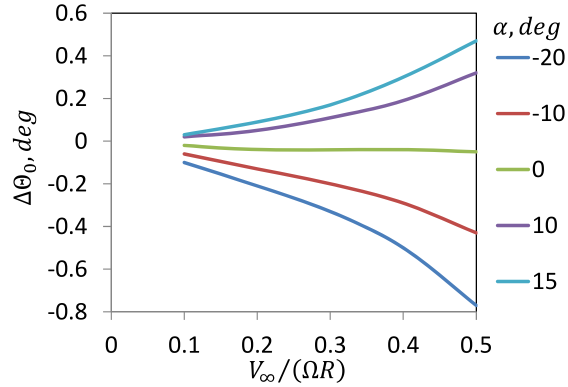

(b) Bo105 rotor on RTA

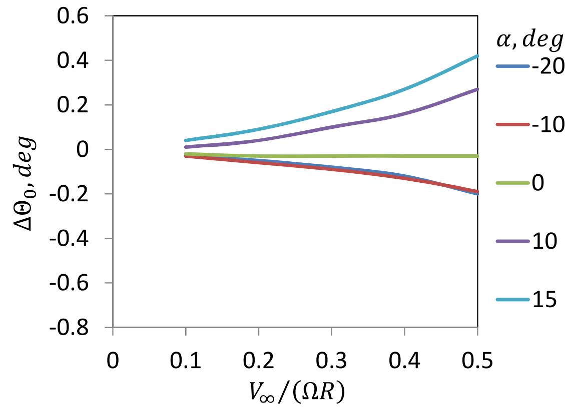

(c) Bo105 model rotor on HART

Figure 62: Effect of fuselage on collective, thrust re-trimmed to isolated rotor.

blockage of the flow, i.e., similar to ground effect, and therefore less collective than required to trim the isolated rotor should result. Cyclic controls should not be affected in this case, because of lateral symmetry and almost fore-aft symmetry of the fuselage-induced velocity expected in such conditions.

While LRTA and HART results are quite similar in this range of angle of attack, the RTA appears to induce a stronger variation of mean fuselage upwash or downwash, depending on angle of attack, and causes larger changes in collective especially for $\alpha < 0°$.

b. Fuselage effect on lateral control

The upwash in the front combined with a downwash in the rear requires strong lateral control for re-trimming, which can be seen in figure 63. This is the dominant impact of a fuselage below a rotor. Different shapes of the RTA and HART fuselage result in different magnitudes of lateral control, especially for negative angles of attack. The HART fuselage maintains a strong relative difference in upwash and downwash, requiring a large lateral control for this entire range of fuselage incidences. These results are obtained for the same condition as before, i.e., re-trimming the rotor-fuselage combination to the same hub thrust and moments as the isolated rotor.

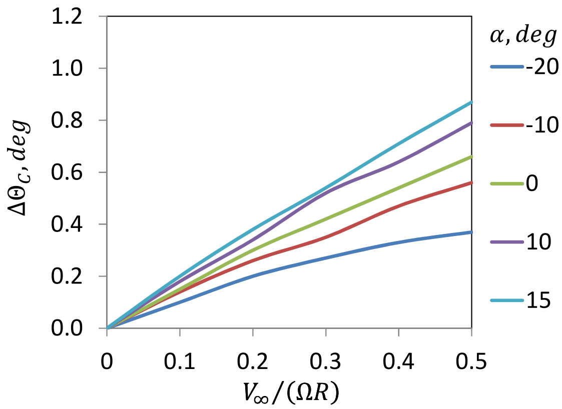

(a) Bo105 rotor on down-scaled LRTA

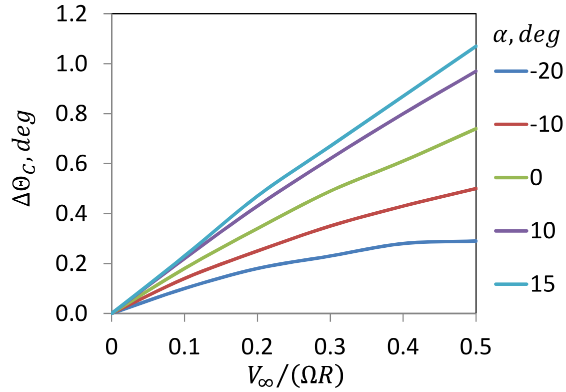

(b) Bo105 rotor on RTA

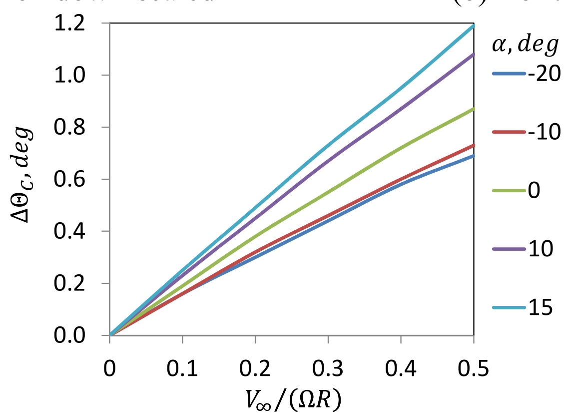

(c) Bo105 model rotor on HART

Figure 63: Effect of fuselage on lateral cyclic, thrust re-trimmed to isolated rotor.

c. Fuselage effect on longitudinal control

Compared to the simple theory results shown previously where the impact of the fuselage on the longitudinal control was found marginal, the nonlinear simulation shown in figure 64 is found more significant, depending on the type of blade attachment to the hub. For small to moderate advance ratios of $\mu \leq 0.2$, the theoretical results are seen here (marginal to negligible impact), but for larger advance ratios the nonlinear aerodynamics and the different trim philosophy influence the results. The simple theory did not re-trim the thrust but rather kept the collective constant. At high advance ratios, collective and longitudinal control are strongly coupled such that both affect thrust and hub moments in a similar order of magnitude, in contrast to small advance ratios.

Therefore, the trim to the same thrust is at least partly responsible for the larger impact of the fuselages on longitudinal control seen here, compared to simple analytical results shown previously. Also, the blade attachment (articulated in simple theory vs. hingeless in simulation) plays a role. The transmission of flap moments of the hingeless Bo105 system requires larger changes in the control angle than the articulated rotor system that transmits only shear forces at the hinge offset location. For positive fuselage angles of attack the results of both fuselages are quite similar, while for negative ones the HART fuselage has less impact on longitudinal control than the RTA, similar to the variations in collective shown in figure 62.

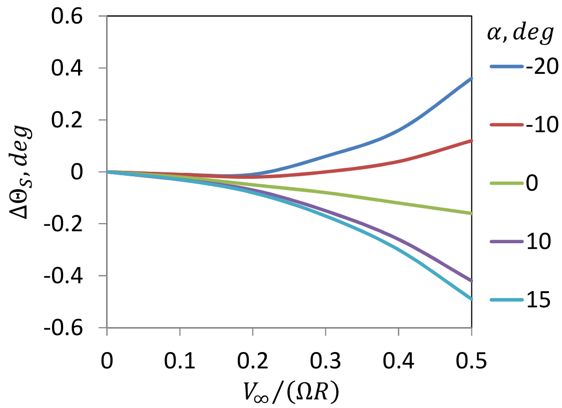

(a) Bo105 rotor on down-scaled LRTA

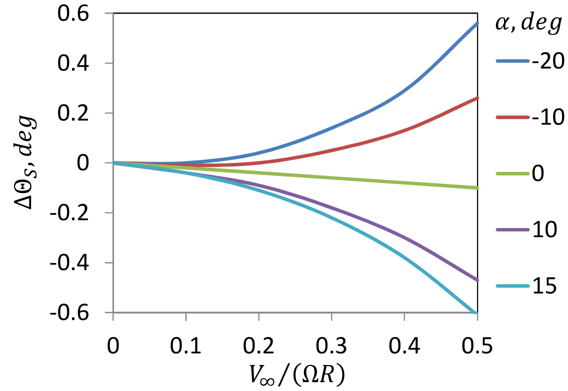

(b) Bo105 rotor on RTA

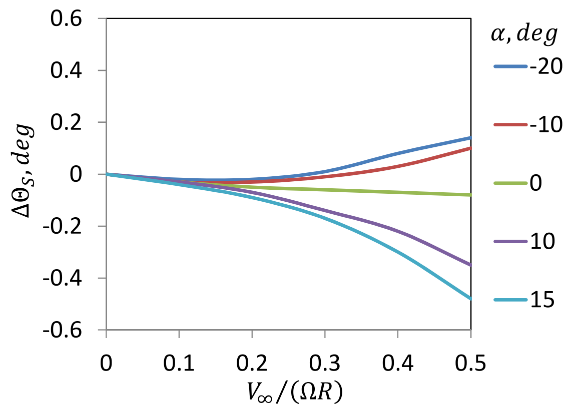

(c) Bo105 model rotor on HART

Figure 64: Effect of fuselage on longitudinal cyclic, thrust re-trimmed to isolated rotor.

d. Fuselage effect on rotor power

Finally the differences in rotor power are shown in figure 65. A fuselage incidence around 0° has a balanced upwash and downwash and therefore only marginal impact on rotor power. When the fuselage incidence is positive (nose up), then a dominating downwash is generated that leads to an increase of power. Contrary, and more effective, is a nose-down inclination of the fuselage, which generates a dominating upwash in the rotor disk—similar to ground effect—reducing power required compared to the isolated rotor. As for the collective control at zero advance ratio, no data are available for the same reasons mentioned there. In such a case, physical consideration predicts an induced upwash over the body caused by the rotor downwash blowing vertically from above on the fuselage, which again is similar to ground effect so a slight power reduction is expected. This represents $\alpha = -90°$.

7.2.3 LRTA, RTA, and HART: Fuselage Effect When Keeping Collective Fixed

A manual trim is required instead of an automated trim using DLR's S4 rotor code and is much more cumbersome, but it allows for cross-checking the theoretical results of Section 6 better than the trim to the same thrust and moments as used in the previous section. This was performed for both rotors only for the highest advance ratio of $\mu = 0.5$. The lines are from the simple theory results, and the symbols are the results from nonlinear simulation with collective kept fixed from isolated rotor trim.

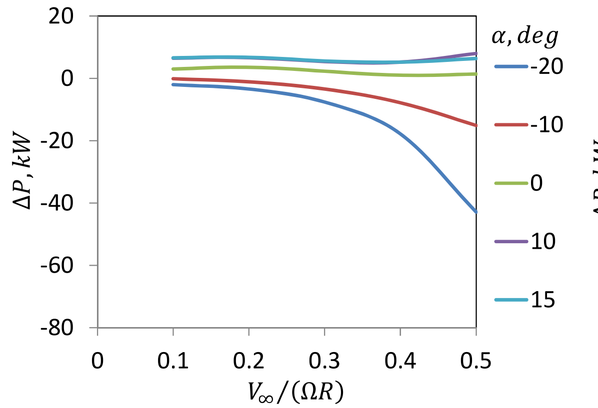

(a) Bo105 rotor on down-scaled LRTA

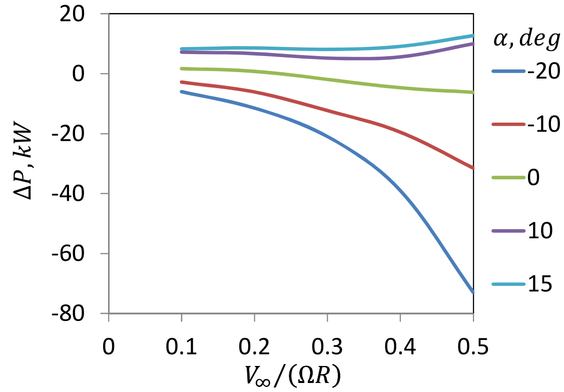

(b) Bo105 rotor on RTA

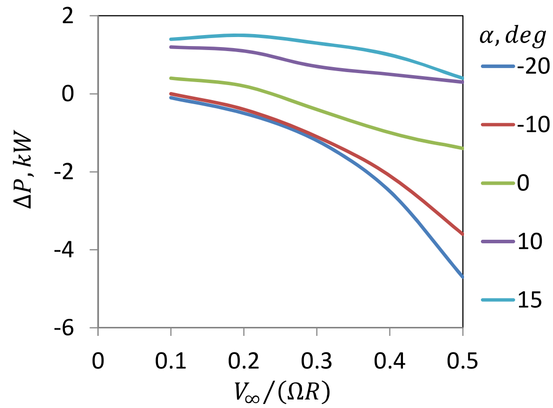

(b) Bo105 model rotor on HART

Figure 65: Effect of fuselage on rotor power, thrust re-trimmed to isolated rotor.

a. Fuselage effect on collective control

Now that the collective is kept fixed from the isolated rotor trim, and only cyclic controls are used for trimming the hub moments to zero, the thrust changes when the fuselage is taken into account are shown in figure 66. The lines are results from simple theory (repeated from figure 56) and the symbols denote nonlinear simulation results.

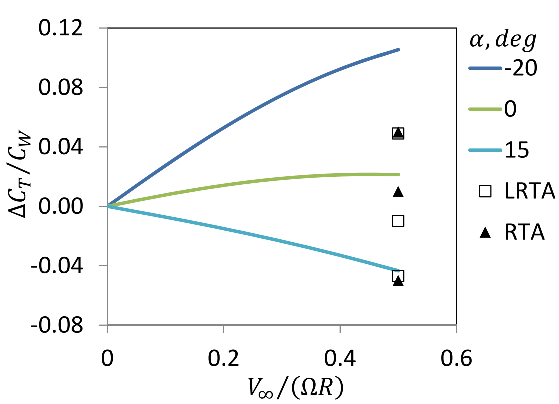

(a) LRTA and RTA

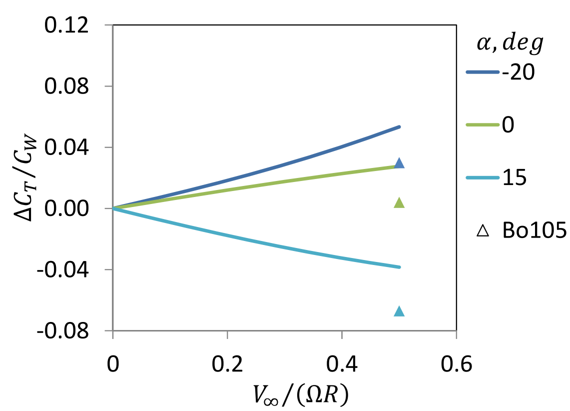

(b) HART

Figure 66: Effect of fuselage on rotor thrust, collective fixed from isolated rotor trim.

In general the simple theory agrees quite well with the nonlinear simulation, especially with the relative changes of thrust, while the absolute values show an offset between theory and simulation. For 0° fuselage incidence and re-trim to thrust, a very small reduction of collective was seen in figure 56. Keeping collective fixed, a comparable small thrust increase is found here. For positive fuselage incidences more increase of collective was needed than reduction of collective for negative incidences (fig. 56). Keeping collective fixed results in more thrust loss for positive incidence than thrust increase for negative incidence.

b. Fuselage effect on lateral control

The impact of the fuselage influence on lateral control is shown in figure 67. Trends and magnitude are predicted by nonlinear simulation very close to the analytical results. The magnitudes are little smaller in the nonlinear simulation (symbols), and this is caused by assuming the fuselage-induced velocities in a plane of $z/R = 0.05$, while the analytic results (lines) are based on a plane of $z/R = 0$ where the fuselage-induced velocities are larger, and the cyclic control needed to eliminate their effect on trim is larger as well. The HART fuselage causes the largest induced velocities for negative angles of attack and larger trim control changes than the LRTA or RTA.

c. Fuselage effect on longitudinal control

Compared to the trim performed in the previous section (fig. 64), the agreement with the simple theory is much better now for the longitudinal control shown in figure 68. The reason is in the difference of trim: In figure 64 the thrust was re-trimmed to that of the isolated rotor, while both the simple analytic results and the nonlinear simulation in figure 68 keep the collective fixed from the isolated rotor trim and only make use of the cyclic controls to re-trim the hub moments. Smaller magnitudes of the nonlinear simulation relative to the simple analytical theory stem from the difference of fuselage-induced velocity extraction in the plane, $z/R = 0.05$, in the former, and $z/R = 0$ in the latter.

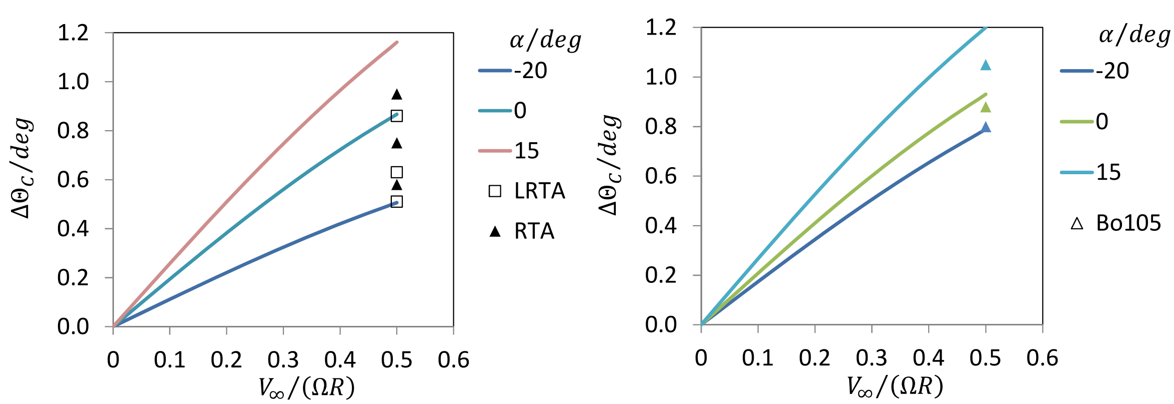

(a) LRTA and RTA (b) HART

Figure 67: Effect of fuselage on lateral control, collective fixed from isolated rotor trim.

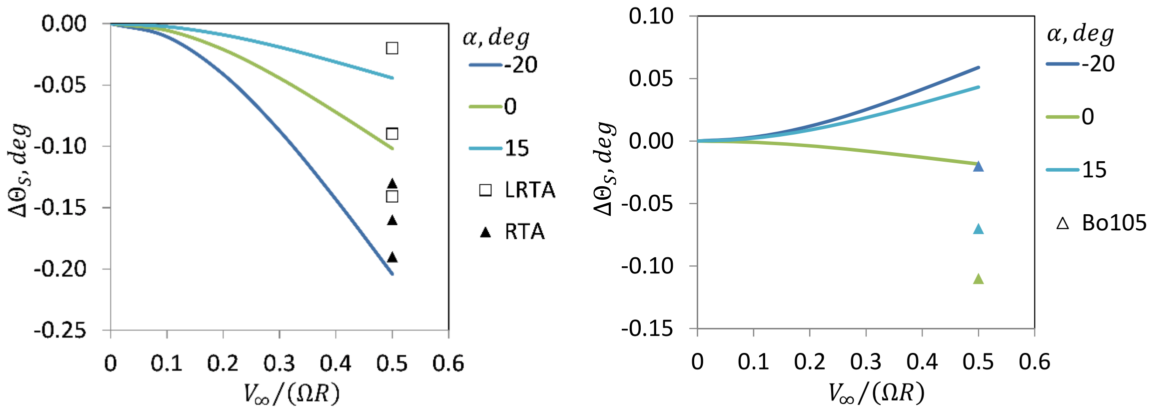

(a) LRTA and RTA (b) HART

Figure 68: Effect of fuselage on longitudinal control, collective fixed from isolated rotor trim.

d. Fuselage effect on rotor power

The power shown in figure 69 is not given in percent, because the reference power in each condition is very different from each other, and the percent value is not comparable. For the LRTA no additional computations have been made, therefore only results for the Bo105 full-scale rotor on the RTA and the model-scale rotor on the HART are shown. As a basic reference, the total power of the isolated Bo105 model rotor for the case of $\mu = 0.5, \alpha = -20°$ is $P = 208\,kW$, so the power increase of $\Delta P = 1.6\,kW$ represents an increase of almost 0.8 percent. On the other extreme, for $\alpha = +15°$ the power of the isolated rotor is negative (windmill state): $P = -31.8\,kW$ and the power difference including the fuselage and keeping the isolated rotor collective fixed is $\Delta P = 6\,kW$, i.e., about 19 percent. This illustrates the uselessness of percent values in power, at least in this context. The trend is similar for the Bo105 full-scale rotor on the RTA: When keeping the trimmed thrust constant, the change of power reflects the change of induced velocity introduced by the fuselage. When keeping collective fixed from the isolated rotor, the increase or decrease of thrust dominates and inverses the change of power due to fuselage-induced velocity.

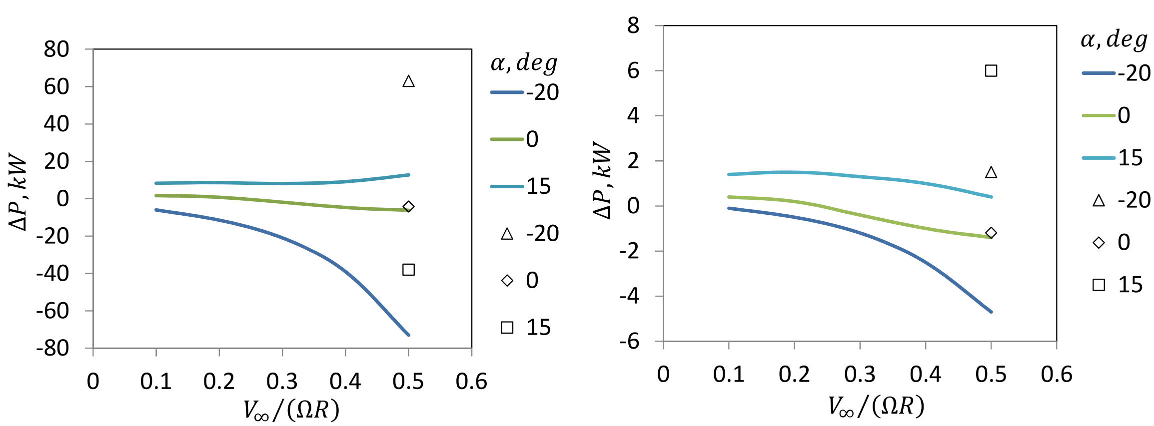

(a) RTA (b) HART

Figure 69: Effect of fuselage on power, collective fixed from isolated rotor trim.

In a helicopter flight situation the latter must be expected, because the rotor thrust must carry both the vehicle weight and also the fuselage download due to rotor downwash/fuselage interaction, while the latter is ignored in an isolated rotor trim. In hover, the rotor downwash acts on the fuselage as if it is in a vertical climb. In any forward flight situation, the rotor downwash impinges on the fuselage from above, modifying its effective angle of attack and dynamic pressure relative to the isolated fuselage. This also causes additional download of the fuselage that the rotor has to carry in addition to the weight, increasing its total thrust. However, this part of the interactional problem remains unsolved and is not part of the current investigation.

8. Conclusions

An analytical mathematical model is presented to approximately compute the fuselage-induced flow field of the LRTA, RTA, and HART fuselages normal to the rotor rotational disk (that is, in shaft axis direction) within the volume of rotor blade operation as defined by $-1 \leq x/R \leq +1, -1 \leq y/R \leq +1,$ and $-0.1 \leq z/R \leq 0.2$. This covers a blade flapping motion with a precone of about 3° due to mean rotor thrust and a blade flapping of 8° amplitude as may develop during flight.

The model reflects the major elements of the fuselage flow field with an average error less than 5 percent of the peak-to-peak data range within each level, z/R, of this volume for the entire range of angle of attack, and an average error less than 6 percent for the entire range of side-slip angles. The model also predicts physical meaningful values outside the validated volume, which by no means claims these are correct or accurate, rather that they are plausible. However, the fuselage angle-of-attack range is strictly limited to $-20° \leq \alpha \leq +15°$ for the LRTA and RTA fuselages (no side-slip) and to $-90° \leq \alpha \leq +90°$ for the HART fuselage, which covers all forward flight conditions from vertical climb to vertical descent. For the HART fuselage, side-slip angles in a range of $-90° \leq \beta \leq +90°$ are also modeled, representing quartering flight to the right or left in the limits. In addition, any combination of angle of attack and side-slip may be computed for the HART fuselage. Although these are not yet validated with CFD data and are of pure predictive nature, the model results in smooth transition between available data.

The purpose of usage is within comprehensive rotor codes such as CAMRAD II or DLR's S4. Two applications are considered for this model:

a) Blade element aerodynamics: modification of local angle of attack and dynamic pressure.
b) Rotor wake: prescribed or free-wake perturbations due to fuselage presence.

The first application will modify blade loading, especially in fast flight because the fuselage-induced velocities scale with flight speed. They will change rotor thrust and moments, and trim control angles. The second application can affect blade-vortex interaction (BVI) locations and rotor noise radiation, but this effect is considered minor because these BVI locations are at lateral positions farther away of the fuselage where the fuselage-induced velocities are rather small and therefore the wake perturbations are as well.

Results found by using this model are (angle-of-attack variations only):

a) Effect on thrust (or collective control)
   The mean value of fuselage-induced velocities is about zero for zero angle of attack, so the impact on thrust or collective to re-trim thrust is about zero as well. Nose-down (negative) angles of attack cause an upwash in average and a thrust increase, or smaller collective to re-trim the rotor; nose-up (positive) angles act opposite. The effect is essentially linear in advance ratio and nonlinear in angle of attack.

b) Lateral cyclic control
   The upwash in the front half of the disk, combined with the downwash in the rear half of the disk, requires large lateral cyclic control angles up to 1° and more to re-trim the rotor. The effect is essentially linear in advance ratio and nonlinear in angle of attack. In the extremes, when $\alpha = \pm 90°$, the fore-aft asymmetry almost vanishes (upwash or downwash everywhere with only little fore-aft imbalance).

c) Longitudinal cyclic control
Compared to the lateral control, the fuselage effect on longitudinal control is much less. This is due to the lateral symmetry of the fuselage-induced velocity field. The effect is essentially quadratic in the advance ratio and nonlinear in angle of attack; it vanishes for $\alpha = \pm 90°$ because then the difference in dynamic pressure on the advancing and retreating side no longer exists.

d) Rotor power
The fuselage impact on power consumed by the rotor is dependent on trim philosophy. When re-trimming to the isolated rotor thrust, the fuselage-induced mean upwash (generated in nose-down angles of attack) acts similar to a ground effect and reduces power, while nose-up angles cause a mean induced downwash and an increase in power. In opposite, when keeping the collective fixed from the isolated rotor trim, the upwash of nose-down angles of attack causes a thrust increase, which causes an increase in power as well. Similarly, in nose-up angles of attack the mean downwash generated reduces the thrust of the rotor and with it the power required. The truth of a free-flying helicopter may be somewhere in between because the fuselage aerodynamic loads also vary from the isolated fuselage condition to one with a rotor on top of it in close proximity. Then, the rotor downwash will cause additional fuselage (down)loads that the rotor has to carry by additional thrust. The magnitude of this effect still has to be evaluated and will be highly dependent on operational conditions.

9. References

[1] Sheridan, P.F., and Smith, R.P.: Interactional Aerodynamics – a New Challenge to Helicopter Technology. *JAHS*, **25** (1), (1980).

[2] Huber, H., and Polz, G.: Studies on Blade-to-Blade and Rotor-Fuselage-Tail Interferences. *Aircraft Engineering and Aerospace Technology*, **55** (10), (1983).

[3] Keys, C., and Wiesner, R.: Guidelines for Reducing Helicopter Parasite Drag. *JAHS*, **20** (1), (1975).

[4] Leishman, J.G., and Bi, N.: Aerodynamic Interactions Between a Rotor and a Fuselage in Forward Flight. *JAHS*, **35** (3), (1990).

[5] Bi, N., and Leishman, G.: Experimental Study of Rotor/Body Aerodynamic Interactions. *AIAA Journal of Aircraft*, **27** (9), (1990).

[6] McVeigh, M.A., Grauer, W.K., and Paisley, D.J.: Rotor/Airframe Interactions on Tiltrotor Aircraft. *JAHS*, **35** (3), (1990).

[7] Bagai, A., and Leishman, J.G.: Experimental Study of Rotor Wake/Body Interactions in Hover. *JAHS*, **37** (4), (1992).

[8] Betzina, M.D., Smith, C.A., and Shinoda, P.: Rotor/Body Aerodynamic Interactions. *VERTICA*, **9** (1), (1985).

[9] Smith, C.A., and Betzina, M.D.: Aerodynamic Loads Induced by a Rotor on a Body of Revolution. *JAHS*, **31** (1), (1986).

[10] Le Pape, A., Gatard, J., and Monnier, J.-C.: Experimental Investigations of Rotor–Fuselage Aerodynamic Interactions. *JAHS*, **52** (2), (2007).

[11] Crouse, G.L., Leishman, G.J., and Bi, N.: Theoretical and Experimental Study of Unsteady Rotor/Body Aerodynamic Interactions. *JAHS*, **37** (1), (1992).

[12] Berry, J., and Bettschart, N.: Rotor/Fuselage Interaction: Analysis and Validation With Experiment. 53rd AHSF, Virginia Beach, VA, April 29–May 1, 1997.

[13] Wilby, P.G., Young, C., and Grant, J.: An Investigation of the Influence of Fuselage Flow Field on Rotor Loads and the Effects of Vehicle Configuration. *VERTICA*, **3** (2), (1979).

[14] Rand, O.: Influence of Interactional Aerodynamics on Helicopter Rotor/Fuselage Coupled Response in Hover and Forward Flight. *JAHS*, **34** (4), (1989).

[15] Rand, O., and Gessow, A.: Model for Investigation of Helicopter Fuselage Influence on Rotor Flowfields. *AIAA Journal of Aircraft*, **26** (5), (1989).

[16] Mavris, D.N., Komerath, N.M., and McMalhon, H.M.: Prediction of Aerodynamic Rotor-Airframe Interactions in Forward Flight. *JAHS*, **34** (4), (1989).

[17] Schillings, J., and Reinesch, R.: The Effect of Airframe Aerodynamics on V-22 Rotor Loads. *JAHS*, **34** (1), (1989).

[18] Lorber, P.F., and Egolf, T.A.: An Unsteady Helicopter Rotor-Fuselage Aerodynamic Interaction Analysis. *JAHS*, **35** (3), (1990).

[19] Crouse, G.L.: Active Control of Vibratory Airloads Induced by Helicopter Rotor-Fuselage Interactions. AIAA Paper 93-1363-CP, AIAA/ASME/ASCE/AHS/ASC 34th Structures, Structural Dynamics, and Materials Conference, La Jolla, CA, April 19–21, 1993.

[20] Quackenbush, T.R., Lam, C.-M.G., and Bliss, D.B.: Vortex Methods for the Computational Analysis of Rotor/Body Interaction. *JAHS*, **39** (4), (1994).

[21] Wachspress, D.A., Quackenbush, T.R., and Boschitsch, A.H.: Rotorcraft Interactional Aerodynamics With Fast Vortex/Fast Panel Methods. *JAHS*, **48** (4), (2003).

[22] Kenyon, A.R., and Brown, R.E.: Wake Dynamics and Rotor-Fuselage Aerodynamic Interactions. *JAHS*, **54** (1), (2009).

[23] Yamauchi, G.K., and Johnson, W.: Analysis of Axi-symmetric Body Effects on Rotor Aerodynamics Using Modified Slender Body Theory. AIAA Paper 84-2204, AIAA 2nd Applied Aerodynamics Conference, Seattle, Washington, Aug. 21–23, 1984.

[24] Kelly, M.E., and Brown, R.E.: The Effect of Blade Aerodynamic Modeling on the Prediction of the Blade Airloads and the Acoustic Signature of the HART II Rotor. 35th European Rotorcraft Forum, Hamburg, Germany, Sept. 22–25, 2009.

[25] Nam, H.J., Park, Y.M., and Kwon, O.J.: Simulation of Unsteady Rotor–Fuselage Aerodynamic Interaction Using Unstructured Adaptive Meshes. *JAHS*, **51** (2), (2006).

[26] Renaud, T., O'Brien, D., Smith, M., and Potsdam, M.: Evaluation of Isolated Fuselage and Rotor-Fuselage Interaction Using Computational Fluid Dynamics. *JAHS*, **53** (1), (2008).

[27] Wagner, S., Dietz, M., and Embacher, M.: Influence of Grid Arrangements and Fuselage on the Numerical Simulation of the Helicopter Aeromechanics in Slow Descent Flight. 15th International Conference on Computational and Experimental Engineering and Sciences Conference (ICCES08), Honolulu, HI, March 17–22, 2008.

[28] Lim, J.W., and Dimanlig, A.C.B.: An Investigation of the Fuselage Effect for HART II Using a CFD/CSD Coupled Analysis. 2nd International Forum on Rotorcraft Multidisciplinary Technology, Seoul, Korea, Oct. 19–20, 2009.

[29] Lim, J.W., and Dimanlig, A.C.B.: The Effect of Fuselage and Rotor Hub on Blade-Vortex Interaction Airloads and Rotor Wakes. 36th European Rotorcraft Forum, Paris, France, Sept. 7–9, 2010.

[30] Sa, J.H., Kim, J.W., Park, S.H., You, Y.-H., Park, J.-S., Jung, S.N., and Yu, Y.H.: Prediction of HART II Airloads Considering Fuselage Effect and Elastic Blade Deformation. 4th AHS International Meeting on Advanced Rotorcraft Technology and Safety Operations (Heli Japan), Saitama, Japan, Nov. 1–3, 2010.

[31] Jung, S.N., Sa, J.H., You, Y.H., Park, J.S., and Park, S.H.: Loose Fluid-Structure Coupled Approach for a Rotor in Descent Incorporating Fuselage Effects. *AIAA Journal of Aircraft*, **50** (4), (2013).

[32] Park, J.S., Sa, J.H., Park, S.H., You, Y.H., and Jung, S.N.: Loosely-Coupled Multibody Dynamics-CFD Analysis for a Rotor in Descending Flight. *Aerospace Science and Technology*, **29** (1), (2013).

[33] Lim, J.W., Wissink, A., Jayaraman, B., and Dimanlig, A.: Helios Adaptive Mesh Refinement for HART II Rotor Wake Simulations. 68th AHSF, Ft. Worth, TX, May 1–3, 2012.

[34] Biava, M., and Vivegano, L.: Simulation of a Complete Helicopter: A CFD Approach to the Study of Interference Effects. *Aerospace Science and Technology,* **19** (1), (2012).

[35] van der Wall, B.G.: Extensions of Prescribed Wake Modeling for Helicopter Rotor BVI Noise Investigations. *CEAS Aeronautical Journal*, **3** (1), (2012).

[36] Stepniewski, W.Z., and Keys, C.N.: *Rotary-Wing Aerodynamics*, ISBN 0486646475, Dover Publications, 1984, pp. 275-283

[37] Dreier, M.E.: *Introduction to Helicopter and Tiltrotor Flight Simulation*, ISBN-13: 978-1-56347-873-4, AIAA Education Series, Reston, VA, 2007

[38] Leoni, R.D.: *Black Hawk: The Story of a World Class Helicopter*, ISBN 978-1-56347-918-2, AIAA Library of Flight, Reston, VA, 2007.

[39] Gerhold, T., Galle, M., Friedrich, O., and Evans, J.: Calculation of Complex Three-Dimensional Configurations Employing the DLR-TAU-Code. AIAA Paper 97-0167, 35th AIAA Aerospace Sciences Meeting & Exhibit, Reno, NV, Jan. 6–9, 1997.

[40] Spalart, P., and Allmaras, S.: A One-Equation Turbulence Model for Aerodynamic Flows. AIAA Paper 92-0439, 30th AIAA Aerospace Sciences Meeting & Exhibit, Reno, NV, Jan. 6–9, 1992.

[41] N.N. *POINTWISE USER MANUAL*, Pointwise, 213 South Jennings Ave, Fort Worth, TX 76104-1107, 2012.

[42] Lapeira, L., Wiegers, B., and Hafemann, W.: *$C^2A^2S^2E$-2 User-Guide*, Version 1.0, 2013.

[43] Rajagopalan, R.G., Baskaran, V., Hollingsworth, A., Lestari, A., Garrick, D., Solis, E., and Hagerty, B.: RotCFD, a Tool for Aerodynamic Interference of Rotors: Validation and Capabilities. AHS Future Vertical Lift Aircraft Design Conference, San Francisco, CA, Jan. 18–20, 2012.

[44] Young, L.A., and Rajagopalan, R.G.: Simulated Rotor Wake Interactions Resulting From Civil Tiltrotor Aircraft Operations Near Vertiport Terminals. 51st AIAA Aerospace Sciences Meeting Including the New Horizons Forum and Aerospace Exposition, Grapevine, TX, Jan. 7–10, 2013.

[45] https://www.rhino3d.com/ accessed May 22, 2015.

[46] http://www.tecplot.com/ accessed May 22, 2015.

[47] Kim, J.W., Park, S.H., and Yu, Y.H.: Euler and Navier–Stokes Simulations of Helicopter Rotor Blade in Forward Flight Using an Overlapped Grid Solver. AIAA paper 2009–4268, 19th AIAA CFD Conference, San Antonio, TX, June 22–25, 2009.

[48] van der Wall, B.G.: A Comprehensive Rotary-Wing Database for Code Validation: The HART II International Workshop. Aeronautical Journal of the Royal Aeronautical Society, **115** (1163), (2011); Erratum in: **115** (1166), (2011).

[49] Park, S.H., and Kwon, J.H.: Implementation of k-ω Turbulence Models in an Implicit Multigrid Method. AIAA Journal, **42** (7), (2004).

[50] van der Wall, B.G., Bauknecht, A., Jung, S.N., and You, Y.H.: Semi-Empirical Modeling of Fuselage-Rotor Interference for Comprehensive Codes: The Fundamental Model. CEAS Aeronautical Journal, **5** (4), (2014).

[51] Yin, J., van der Wall, B.G. and Wilke, G.: Rotor Aerodynamic and Noise Under Influence of Elastic Blade Motion and Different Fuselage Modeling. 40th European Rotorcraft Forum, Southampton, UK, Sept. 2–5, 2014.

[52] Benoit, B., Dequin, A.-M., Kampa, K., von Grünhagen, W., Basset, P.-M. and Gimonet, B.: HOST, a General Helicopter Simulation Tool for Germany and France. AHS 56th Annual Forum and Technology Display, Virginia Beach, VA, May 2–4, 2000.

[53] van der Wall, B.G.: An Analytical Model of Unsteady Profile Aerodynamics and Its Application to a Rotor Simulation Program. 15th European Rotorcraft Forum, Amsterdam, Netherlands, Sept. 12–15, 1989.

[54] van der Wall, B.G.: Analytic Formulation of Unsteady Profile Aerodynamics and Its Application to Simulation of Rotors. ESA TT-1244, 1992 (Translation of the Research Report DLR-FB 90–28, 1990).

[55] Mangler, K.W., and Squire, H.B.: The Induced Velocity Field of a Rotor. ARC R&M 2642, 1950.

[56] Leiss, U.: A Consistent Mathematical Model to Simulate Steady and Unsteady Rotor-Blade Aerodynamics. 10th European Rotorcraft Forum, The Hague, Netherlands, Aug. 28–31, 1984.